M 2026

U.PORTO
FEUP FACULDADE DE ENGENHARIA
UNIVERSIDADE DO PORTO

Characterisation of plug welds in dissimilar joints of carbon steel and austenitic stainless steel with different thicknesses.

Gonçalo Miranda Ribeiro
MASTER'S DEGREE DISSERTATION IN MATERIAL ENGINEERING SUBMITTED TO THE FACULTY OF ENGINEERING OF THE UNIVERSITY OF PORTO

Supervisor
Professora Laura MM Ribeiro

Co-supervisor
Professor Abílio Jesús

U.PORTO
FEUP FACULDADE DE ENGENHARIA
UNIVERSIDADE DO PORTO

CANDIDATO	Gonçalo Miranda Ribeiro	*Código* 202006913
TÍTULO	Characterisation of plug welds in dissimilar joints of carbon steel and austenitic stainless steel with different thicknesses.	
DATA	20-07-2026	
LOCAL	Faculdade de Engenharia da Universidade do Porto – Sala F106 – 10:00	

JÚRI	*Presidente*	*Prof.º Rúben Santos*	DEMEC/FEUP
	Arguente	*Dr.ª Rita Dantas*	DEMEC/FEUP
	Orientador	*Prof.ª Laura Ribeiro*	DEMEC/FEUP

“All the great things are simple, and many can be expressed in single words: freedom, justice, honour, duty, mercy, hope.”

Winston Churchill

ABSTRACT

The integration of dissimilar materials is a key enabler for lightweight and structurally efficient railway vehicles. Within the Train Solutions Portugal project, a critical challenge is the reliable joining of stainless steel car bodies to low-carbon structural steel end beams through the underframe bolster region, which is responsible for load transfer between the car body and bogies, including bump-stop/draw-gear interactions.

This study presents the microstructural and mechanical characterisation of plug fusion weldments in S355J2 structural steel and AISI 301LN austenitic stainless steel joints, representative of the previously described structural configuration. Specimens were welded with two different filler materials, AWS A5.9 ER308LSi and AWS A5.22 E309LMoT0-1/4, using controlled process parameters and fabrication procedures that reflect industrial practice. A single plug-weld joint geometry with three thickness combinations was investigated using macrostructural and microstructural analyses, Vickers microhardness mapping, salt-spray corrosion tests, monotonic tensile testing, and constant-amplitude fatigue testing to examine heterogeneities, defects, and potential crack initiation sites associated with plug welding.

Fatigue tests under constant-amplitude loading were performed to establish fatigue life behaviour and to assess failure mechanisms. Results indicate that the two materials didn't show a significant discrepancy in the macro and micro analyses and in the microhardness mapping; however, in the corrosion tests, the AWS A5.22 E309LMoT0-1/4 exhibited a higher corrosion resistance. In fatigue life testing, only specimens welded with AWS A5.22 E309LMoT0-1/4 were evaluated. The novelty of this work lies in the integrated experimental characterisation of weld geometry, mechanical mismatch and fatigue behaviour in dissimilar plug fusion joints, a configuration that remains largely unexplored in the literature.

The results obtained underscore the importance of weld design and process optimisation in improving joint performance, thereby contributing to the development of robust multi-material joining strategies applicable to railway structures.

Keywords: Fatigue performance; Plug fusion welding; Dissimilar steel joints; AISI 301LN / S355J2; Railway structures; Crack initiation

RESUMO

A integração de materiais dissimilares constitui um fator determinante para o desenvolvimento de veículos ferroviários estruturalmente eficientes e de peso reduzido. No âmbito do projeto *Train Solutions Portugal*, um dos desafios críticos reside na ligação viável entre o aço inoxidável e o aço estrutural de baixo teor de carbono, através da região do estrado (bolster), responsável pela transferência de carga entre a caixa e os bogies, incluindo as interações com os batentes (bump-stops) e o sistema de engate (draw-gear). Este estudo apresenta a caracterização microestrutural e mecânica de juntas soldadas por fusão em tampão (plug weld) entre aço estrutural S355J2 e aço inoxidável austenítico AISI 301LN, representativas da configuração estrutural descrita anteriormente. Os provetes foram soldados com dois metais de adição distintos, AWS A5.9 ER308LSi e AWS A5.22 E309LMoT0-1/4, recorrendo a parâmetros de processo controlados e a procedimentos de fabrico representativos da prática industrial. Foi analisada uma única geometria de junta soldada em tampão, com três combinações de espessura, por meio de análises macro e microestruturais, mapeamento de microdureza Vickers, ensaios de corrosão em câmara de nevoeiro salino, ensaios de tração monotónica e ensaios de fadiga a amplitude constante, com vista a examinar heterogeneidades, defeitos e potenciais locais de iniciação de fenda associados à soldadura em tampão. Os ensaios de fadiga sob carregamento de amplitude constante foram realizados com o objetivo de estabelecer o comportamento à vida à fadiga e avaliar os mecanismos de rotura.

Os resultados indicam que os dois materiais não apresentaram discrepâncias significativas nas análises macro e microestruturais, nem no mapeamento de microdureza; contudo, nos ensaios de corrosão, o metal de adição AWS A5.22 E309LMoT0-1/4 evidenciou uma resistência à corrosão superior. Nos ensaios de fadiga, apenas os provetes soldados com AWS A5.22 E309LMoT0-1/4 foram avaliados. A originalidade deste trabalho reside na caracterização experimental integrada da geometria da soldadura, da incompatibilidade química dos materiais, da variação de espessura e do comportamento à fadiga em juntas soldadas por fusão em tampão de materiais dissimilares, uma configuração ainda pouco explorada na literatura.

Os resultados obtidos sublinham a importância do projeto da soldadura e da otimização do processo para melhorar o desempenho da junta, contribuindo, assim, para o desenvolvimento de estratégias robustas de ligação multimaterial aplicáveis a estruturas ferroviárias.

Palavras-Chave: Desempenho à fadiga; Soldadura por tampão; Juntas de aço dissimilares; AISI 301LN / S355J2; Estruturas ferroviárias; Iniciação de fenda.

ACKNOWLEDGEMENTS

I want to express my deepest gratitude to everyone who supported me and whom I encountered throughout my academic journey, which culminated in this project.
First, I am profoundly grateful to my supervisor, Prof. Laura Ribeiro, for her constant support and for always being available whenever I needed guidance. I would also like to thank Prof. Abílio de Jesus for all the support provided throughout this dissertation. My thanks also go to my internship supervisor, Bernardo Begonha, for his availability and for making me feel so welcome during my time there, as well as to everyone at SERMEC for their warm hospitality. A special thanks to the welders, João and Rui, who generously gave their time to produce the specimens and patiently answered all my questions, and to João Silva for his help throughout the mechanical tests and for consistently clearing my doubts.
I am also thankful to several people from the Department of Mechanical Engineering who crossed my path and, with their willingness to help, made my days brighter: José Ramiro Soares, Maria João Moreira, Maria Cândida Silva, José Carlos Fonseca, Joana Angélica Loureiro, and Manuel Fernando Vieira. A special thank you to Dr. Bruno Oliveira for all his invaluable help in carrying out these tests.
To the great friends this academic journey has given me Bruno Cunha, Dinis Carneiro, Gonçalo Cruz, and everyone in the "Praia" group thank you for helping me through these six years. A special mention goes to João Pires, my partner in all the battles we conquered over these six years; thank you for being my support and, above all, my true friend.
I cannot forget my long-time friends, Tiago Soares and Tiago Ribeiro, for their constant support and encouragement over the years. To my friends in "Dinamismos Insanos," thank you for always lifting my spirits and being a pillar of support, ensuring I never gave up during the hardest moments. Also, thanks to my friends in "Triple 1" for all the late-night gatherings that helped me relax and kept my motivation high.
Finally, to my parents, thank you for all the love, support, and encouragement throughout all these years I love you so much. To my sister, who gets on my nerves, but I know she is always rooting for me. To my grandparents and my aunt, who might not fully understand all the work I have done, thank you for your unconditional support and for all the warm meals that comforted my heart. To my godparents who always encouraged me throughout the years, a special thanks to my godfather for all the moments spent at Estádio do Dragão.

INSTITUCIONAL ACKNOWLEDGEMENTS

I want to thank the Centro de Apoio Tecnológico à Indústria Metalomecânica (CATIM) for conducting the Corrosion tests in artificial atmospheres – Salt spray tests, especially to Eng. Ana Azevedo and Carlos Brabosa. I would also like to express my gratitude to SERMEC GROUP for allowing me to do an internship, particularly to Mário Duarte. This work is a result of Agenda "PRODUCING RAILWAY ROLLING STOCK IN PORTUGAL", nr. C645644454-00000065, investment project nr. 55, financed by the Recovery and Resilience Plan (PRR) and by European Union - NextGeneration EU.



TABLE OF CONTENTS

ABSTRACT i

RESUMO ii

ACKNOWLEDGEMENTS iii

INSTITUCIONAL ACKNOWLEDGEMENTS iv

TABLE OF CONTENTS v

LIST OF FIGURES viii

LIST OF TABLES xi

LIST OF ABBREVIATIONS xii

1.Introduction 1

1.1 Motivation 1

1.2 Objectives 2

1.3 Dissertation's Structure 2

2.Literature Review 3

2.1 Base Materials and Weldability 3

2.1.1 Steel AISI 301LN (EN 10088-2:2005) 3

2.1.2 Welding of austenitic stainless steel 4

2.1.3 Steel S355J2 (EN 10025-2:2004) 5

2.1.4 Welding of carbon steel 6

2.2 Welding 7

2.2.1 Gas Metal Arc welding 8

2.2.2 **Shielding Gases** 10

2.2.3 **Plug welds** 10

2.3 Challenges of joining material 11

2.3.1 Welding dissimilar materials 11
2.2.2 Microstructural prediction 12
2.2.3 Welding Defects 13
2.2.4 Corrosion behaviour of dissimilar welding materials..... 14

2.3 Fatigue in welded structures for railway vehicles..... 15

3.MATERIALS AND METHODS..... 17

3.1 Materials 17
3.1.1 Base Materials 17
3.1.2 Filler Materials 18

3.2 Methods 18
3.2.1 Test Specimens..... 18
3.2.2 Welding Procedure..... 19
3.3.3 Mechanical and Microstructure Characterisation of the welded joints 21
3.3.4 Corrosion Tests 23
3.3.5 Mechanical Test of Welded Specimens..... 24

4.Results and Discussion 26

4.1 Base Materials 26

4.2 Preliminary results 28
4.2.1 Macrographic examination of the plug wels..... 28
4.2.2 Tensile shear test 29
4.2.3 Process improvement..... 31

4.3 Characterisation of final specimens 32
4.3.1 Microstructural characterization..... 32
4.3.2 Microhardness Profiling 39
4.3.3 Corrosions tests analysis 44

4.4 Mechanical tests of the welded joints 45
4.4.1 Tensile shear test of the welded joints..... 45
4.4.2 Fatigue test of the welded joints..... 48

5.CONCLUSIONS AND FUTURE WORK 52

6.References 54

APPENDIX 59

A Tensile Shear Results of Preliminary Results 59

LIST OF FIGURES

FIGURE 1:(A) VERTICAL SECTION OF THE FE-CR-NI PHASE DIAGRAM AT A CONSTANT 70 WT-% FE. (B) SCHEMATIC REPRESENTATION OF THE VARIOUS TYPES OF PRIMARY PHASE SOLIDIFICATIONS (A, AF, FA, AND F) AS A FUNCTION OF COMPOSITION (CREQ/NIEQ RATIO) [22]. 5

FIGURE 2: MICROSTRUCTURES OF AN AUSTENITIC STAINLESS STEEL. (A) AF MODE; (B) FA MODE [22]. 5

FIGURE 3: CCT DIAGRAM OF S355 STEEL [33]. 6

FIGURE 4: SUB-REGIONS OF THE HAZ IN THE FE-C DIAGRAM [30]. 7

FIGURE 5:TYPES OF WELDING PROCESSES [44]. 8

FIGURE 6: SIMPLE DIAGRAM OF THE GAS METAL ARC WELDING PROCESS [52]. 9

FIGURE 7:VOLT-AMPERE CURVE FOR A CONSTANT VOLTAGE POWER SOURCE [52]. 10

FIGURE 8: DISSIMILAR METAL PLUG WELDING CONFIGURATION WITH THE IDENTIFICATION OF THE DIFFERENT MATERIALS INVOLVED (OWN SOURCE). 11

FIGURE 9: SCHAEFFLER DIAGRAM [68]. 12

FIGURE 10: EXPERIMENTAL COMPONENTS AND JOINT ASSEMBLY FOR THE DISSIMILAR PLUG WELD STUDY. (A) STAINLESS STEEL AISI 301LN PLATES SHOWING THE VARIATION IN PRE-DRILLED PLUG HOLE DIAMETERS. (B) CARBON STEEL S355J2 PLATES DISPLAYING THE GROUND SURFACE PREPARATION ON THE LEFT SECTION. (C) FINAL WELDING SETUP: DISSIMILAR LAP JOINT ASSEMBLY SECURED BY CLAMPS BEFORE THE WELDING PROCEDURE. 20

FIGURE 11:SCHEMATIC OF THE TEST SPECIMEN DIMENSIONS FOR PLUG JOINTS, IN ACCORDANCE WITH THE SPECIFICATIONS OF THE AWS D1.1 STANDARD [55]. 21

FIGURE 12: SCHEMATIC REPRESENTATION OF THE TENSILE SHEAR TEST SPECIMEN ACCORDING TO EN ISO 14273:2016. (A) TOP VIEW DETAILING THE GEOMETRICAL PARAMETERS OF THE LAP JOINT. (B) CROSS-SECTIONAL VIEW OF THE TESTING SETUP, ILLUSTRATING THE USE OF SPACER PLATES[100]..... 22

FIGURE 13:ROWS OF INDENTATION IN WELDED JOINTS. 23

FIGURE 14: INITIAL STATE OF THE SPECIMENS BEFORE SALT SPRAY TESTING. THE SPECIMENS ARE ORGANISED BY MATERIAL COMBINATION (ALTERNATING BETWEEN FM). 23

FIGURE 15: SPECIMENS FOR STATIC AND FATIGUE TESTING; A) SAMPLE 8 - TS_01_309; B) SAMPLE 10 - TS_02_309; C) SAMPLE 12 - TS_03_309. 24

FIGURE 16: GEOMETRY AND DIMENSIONS OF THE SPECIMENS PRODUCED FOR FATIGUE TESTS. 24

FIGURE 17: INSTRON 8802 SERVO-HYDRAULIC TESTING MACHINE. 25

FIGURE 18: IMAGES FROM OPTICAL MICROSCOPY OF THE AISI 301LN SHEET WITH DIFFERENT THICKNESS AND TEMPER CONDITIONS: (A) C850, 1.5 MM; (B) C850, 4 MM; AND (C) C1000, 5 MM..... 26

FIGURE 19:IMAGE FROM OPTICAL MICROSCOPY OF THE S355 J2 SHEET WITH 8MM OF THICKNESS. 27

FIGURE 20: STEREO MICROSCOPE IMAGES OF THE CROSS-SECTION OF THE WELD JOINTS: A) SAMPLE 1; B) SAMPLE 2; C) SAMPLE 3; D) SAMPLE 4; E) SAMPLE 5; F) SAMPLE 6. 28

FIGURE 21:SURFACE MACROGRAPHS OF THE FRACTURED PLUG WELD SPECIMENS SEPARATING THE AISI 301LN AND S355J2 INTERFACES. THE MATRIX COMPARES SAMPLES 1 TO 6 ACROSS THREE PLUG DIAMETERS (3 MM, 15 MM, AND 18 MM) WELDED WITH AWS A5.9 ER308LSI (LEFT) AND AWS A5.22 E309LMOT. 30

FIGURE 22: COMPARATION OF THE 18 MM PLUG WELDS DEPOSITED WITH E309LMO FILLER METAL: (A) GEOMETRY WITHOUT COUNTERSINK; (B) GEOMETRY WITH COUNTERSINK. 31

FIGURE 23: MACROSTRUCTURE OF WELDED JOINT BETWEEN 1.5 MM AISI 301LN AND 8 MM S355J2 WITH THE FILLER METAL AWS A5.9 ER308LSI. POSITION 1- FM, POSITION 2- TRIPLE INTERFACE BETWEEN THE 2 BM AND THE FM, POSITION 3- INTERFACE BETWEEN THE FM AND THE AISI 301LN AND POSITION 4- INTERFACE BETWEEN THE FM AND S355J2. 32

FIGURE 24:MICROSTRUCTURE OF THE TS_01_308 PLUG WELD: A) ER308LSI FILLER METAL (POSITION 1); B) INTERFACE BETWEEN THE FILLER METAL AND AISI 301LN (POSITION 2); C) INTERFACE BETWEEN THE FILLER METAL, AISI 301LN AND S355J2 (POSITION 3); D) INTERFACE BETWEEN THE FILLER METAL AND S355J2 (POSITION 4)..... 33

FIGURE 25: MACROSTRUCTURE OF WELDED JOINT BETWEEN 1.5 MM AISI 301LN AND 8 MM S355J2 WITH THE FILLER METAL AWS A5.22 E309LMOT0-1/4. POSITION 1 – INTERFACE BETWEEN THE AISI 301LN WITH THE FM; POSITION 2 – INTERFACE BETWEEN THE S355J2 WITH FM; POSITION 3 – FM ; POSITION 4 - S355J2. 34

FIGURE 26: MICROSTRUCTURE OF THE TS_01_309 PLUG WELD: A) INTERFACE BETWEEN THE FILLER METAL AND AISI 301LN; B) INTERFACE BETWEEN THE FILLER METAL AND S355J2 POSITION 2); C) ER309LMO (POSITION 3); S355J2 (POSITION 4). 34

FIGURE 27:MACROSTRUCTURE OF WELDED JOINT BETWEEN 4 MM AISI 301LN AND 8 MM S355J2 WITH THE FILLER METAL AWS A5.9 ER308LSI.POSITION 1 – INTERFACE BETWEEN THE AISI 301LN WITH THE FM; POSITION 2 – INTERFACE BETWEEN THE S355J2 WITH FM; POSITION 3 – FM. 35

FIGURE 28:MICROSTRUCTURE OF THE TS_02_308 PLUG WELD: A) INTERFACE BETWEEN THE FILLER METAL AND AISI 301LN; B) INTERFACE BETWEEN THE FILLER METAL AND S355J2 POSITION 2); C) ER308LSI (POSITION 3). ... 35

FIGURE 29: MACROSTRUCTURE OF WELDED JOINT BETWEEN 4 MM AISI 301LN AND 8 MM S355J2 WITH THE FILLER METAL AWS A5.22 E309LMOT0-1/4.POSITION 1 – INTERFACE BETWEEN THE AISI 301LN AND THE FM; POSITION 2 – FM; POSITION 3 – INTERFACE BETWEEN THE S355J2 AND FM..... 36

FIGURE 30:MICROSTRUCTURE OF THE TS_02_309 PLUG WELD: A) INTERFACE BETWEEN THE FILLER METAL AND AISI 301LN (POSITION 1); B) POSITION 1; C) ER309LMO (POSITION 2). D) INTERFACE BETWEEN THE FILLER METAL AND S355J2 (POSITION 3). 36

FIGURE 31:MACROSTRUCTURE OF WELDED JOINT BETWEEN 5 MM AISI 301LN AND 8 MM S355J2 WITH THE FILLER METAL AWS A5.9 ER308LSI. POSITION 1 – INTERFACE BETWEEN THE AISI 301LN AND THE FM; POSITION 2 – FM; POSITION 3 – INTERFACE BETWEEN THE S355J2 AND THE FM..... 37

FIGURE 32:MICROSTRUCTURE OF THE TS_03_308 PLUG WELD: A) INTERFACE BETWEEN THE FILLER METAL AND AISI 301LN (POSITION 1); B) ER308LSI (POSITION 2); C) INTERFACE BETWEEN THE FILLER METAL AND S355J2 POSITION 3). 37

FIGURE 33:MACROSTRUCTURE OF WELDED JOINT BETWEEN 5 MM AISI 301LN AND 8 MM S355J2 WITH THE FILLER METAL AWS A5.22 E309LMOT0-1/4.POSITION 1 – INTERFACE BETWEEN THE AISI 301LN AND THE FM; POSITION 2 – INTERFACE BETWEEN THE S355J2 AND THE FM; POSITION 3 – FM..... 38

FIGURE 34:MICROSTRUCTURE OF TS_03_309 PLUG WELD: A) INTERFACE BETWEEN THE FILLER METAL AND AISI 301LN (POSITION 1); B) INTERFACE BETWEEN THE FILLER METAL AND S355J2 (POSITION 2); C) ER309LMO (POSITION 3). 38

FIGURE 35: MICROHARDNESS PROFILE OF THE WELDED JOINT BETWEEN 1.5 MM AISI 301LN AND 8 MM S355J2 WITH THE FILLER METAL AWS A5.9 ER308LSI. 40

FIGURE 36: MACROSTRUCTURE OF WELDED JOINT BETWEEN 1.5 MM AISI 301LN AND 8 MM S355J2 WITH THE FILLER METAL AWS A5.9 ER308LSI..... 40

FIGURE 37: MICROHARDNESS PROFILE OF THE WELDED JOINT BETWEEN 1.5 MM AISI 301LN AND 8 MM S355J2 WITH THE FILLER METAL AWS A5.22 E309LMOT0-1/4..... 40

FIGURE 38:MACROSTRUCTURE OF WELDED JOINT BETWEEN 1.5 MM AISI 301LN AND 8 MM S355J2 WITH THE FILLER METAL AWS A5.22 E309LMOT0-1/4. 41

Figure 39: Microhardness profile of the welded joint between 4 mm AISI 301LN and 8 mm S355J2 with the filler metal AWS A5.9 ER308LSi. 41

Figure 40:Macrostructure of welded joint between 4 mm AISI 301LN and 8 mm S355J2 with the filler metal AWS A5.9 ER308LSi. 42

Figure 41: Microhardness profile of the welded joint between 4 mm AISI 301LN and 8 mm S355J2 with the filler metal AWS A5.22 E309LMoT0-1/4. 42

Figure 42:Macrostructure of welded joint between 4 mm AISI 301LN and 8 mm S355J2 with the filler metal AWS A5.22 E309LMoT0-1/4. 42

Figure 43: Microhardness profile of the welded joint between 5 mm AISI 301LN and 8 mm S355J2 with the filler metal AWS A5.9 ER308LSi. 43

Figure 44:Macrostructure of welded joint between 5 mm AISI 301LN and 8 mm S355J2 with the filler metal AWS A5.9 ER308LSi. 43

Figure 45: Microhardness profile of the welded joint between 5 mm AISI 301LN and 8 mm S355J2 with the filler metal AWS A5.22 E309LMoT0-1/4. 43

Figure 46:Macrostructure of welded joint between 5 mm AISI 301LN and 8 mm S355J2 with the filler metal AWS A5.22 E309LMoT0-1/4. 44

Figure 47: Macrographs of the welded joints (Samples 7 to 12) showing the surface evolution during the neutral salt spray test at 0 h, 48 h, and 96 h of exposure, comparing filler metals AWS A5.9 ER308LSi and AWS A5.22 E309LMoT0-1/4. 45

Figure 48: Experimental failure mode of the specimen subjected to tensile testing, showing interfacial fracture. 46

Figure 49: Experimental shear force-displacement graph – Geometry 1.5 mm AISI 301LN and 8 mm S355J2. 46

Figure 50:Experimental shear force-displacement graph – Geometry 4 mm AISI 301LN and 8 mm S355J2. 47

Figure *51*:Experimental shear force-displacement graph – Geometry 5 mm AISI 301LN and 8 mm S355J2. 47

Figure 52: Lack of fusion defect observed in specimen TS_01_02. 48

Figure 53: Fatigue Performance of TS_01_309, TS_02_309 and TS_03_309(Load range (N)). 48

Figure 54:: Fatigue Performance of TS_01_309, TS_02_309 and TS_03_309(Shear stress range (MPa)). 49

Figure 55: Fatigue test specimens of condition TS_02_309, a) partial pull-out failure mode in S355J2, b) interfacial fracture mode and c) partial pull-out failure mode in AISI 301LN. 50

Figure 56: Fatigue test specimens of condition TS_03_309 partial pull-out failure mode in S355J2. ... 51

LIST OF TABLES

TABLE 1: CHEMICAL COMPOSITION OF AISI 301 LN (WT.%) [21]. 3
TABLE 2: CHEMICAL COMPOSITION S355J2 (WT%) [32]..... 6
TABLE 3: EQUATIONS TO CALCULATE TEST PARAMETERS..... 16
TABLE 4: CHEMICAL COMPOSITION OF BASE MATERIALS USED [91–94]. 17
TABLE 5: MECHANICAL PROPERTIES OF BASE MATERIALS USED [91–94]. 18
TABLE 6: CHEMICAL COMPOSITION OF THE FILLER MATERIALS USED [96,97]. 18
TABLE 7:MECHANICAL PROPERTIES OF FILLER METALS USED [96,97]. 18
TABLE 8: EXPERIMENTAL MATRIX, NOMENCLATURE AND DIMENSIONS OF THE SPECIMENS..... 19
TABLE 9: FINAL MATRIX, NOMENCLATURE AND DIMENSIONS OF THE SPECIMENS. 19
TABLE 10: FIRST STAGE MAG WELDING OPERATIONAL PARAMETERS. 20
TABLE 11: FINAL STAGE MAG WELDING OPERATIONAL PARAMETERS. 21
TABLE 12: DIMENSIONS OF TENSILE TEST SPECIMENS, ACCORDING TO EN ISO 14273:2016 [100]. 21
TABLE 13: TESTING CONDITIONS..... 23
TABLE 14: HARDNESS RESULTS OF BASE MATERIALS 27
TABLE 15: STATISTICAL SUMMARY OF THE TENSILE SHEAR TEST FOR SAMPLES 1 TO 6, DISPLAYING THE MINIMUM, MAXIMUM, AND AVERAGE FAILURE LOAD (N), AND THE RELATIVE STANDARD DEVIATION (RSD)..... 29
TABLE 16: STATISTICAL ANALYSIS OF THE FATIGUE RESULTS..... 49

LIST OF ABBREVIATIONS

A. Austenitic
AF. Austenitic-Ferritic
BM. Base Material
CE. Carbon Equivalent
CHAZ. Coarse Grained Heat Affected Zone
Cr_{eq}. Chromium equivalent
CV. Constant-Voltage
DCEN. Direct Current Electrode Negative
DCEP. Direct Current Electrode Positive
DIM. Deformation Induced Martensite
F. Ferritic
FA. Ferritic-Austenitic
FCC. Face-Centred Cubic
FGHAZ. Fine Grained Heat Affected Zone
FM. Filler Metal
FZ. Fusion Zone
GMAW. Gas Metal Arc Welding
HAZ. Heat-Affected Zone
HCF. High Cycle Fatigue
ICHAZ. Inter-Critical Heat Affected Zone
LCF. Low Cycle Fatigue
MAG. Metal Active Gas
MIG. Metal Inert Gas
Nieq. Nickel equivalent
PWHT. Post Weld Heat Treatment
RSD. Relative Standard Deviation
TRIP. Transformation Induced Plasticity
WFS. Wire Feed Speed

1. Introduction

This dissertation was carried out as part of the Master´s Degree in Materials Engineering at the Faculty of Engineering of the University of Porto (FEUP). This chapter introduces the project's motivation and objectives.

1.1 Motivation

The transport sector is under global pressure to lower its ecological footprint. Consequently, rail transport has re-emerged as a strategic pillar for sustainable mobility. In the European Union (EU), rail accounted for just 0.3% of transport-related greenhouse gas emissions in 2022, despite carrying 8.1% of passengers and 16.6% of freight [1].

Therefore, rail transport is central to achieving the mobility goals outlined in the European Green Deal and the Sustainable and Smart Mobility Strategy. The objective is clear: achieving climate neutrality by 2050 requires a significant modal shift from road to rail [2].

In Portugal, this trajectory is reflected in the National Railway Plan (Plano Ferroviário Nacional), which seeks to modernise, scale the national network and build a fully Portuguese train [3].

Historically, between the early 1960s and the mid-1970s, the company SOREFAME manufactured hundreds of railway units. This autonomous production not only modernised the Portuguese fleet but also established high technical standards. However, following the cessation of SOREFAME'S activity after 1974, Portugal became reliant on foreign manufacturers [4]. To reverse this dependence and diversify the national productive structure, the project "Producing Railway Rolling Stock in Portugal" was launched under the Recovery and Resilience Plan (PRR). This ambitious initiative aims to enable the national industry to acquire essential knowledge and strengthen production capacity by developing a new train [3].

Within this framework, the present thesis was developed in collaboration with the SERMEC GROUP as part of the master's Program in Materials Engineering.

The SERMEC GROUP is the main leader of this project involving another 13 entities. The SERMEC was founded in 1985 by its current president, Mário Duarte, and comprises four companies: SERMEC II, SERMEC Windpower, Weartech, and Ibermill. While its primary activity involves the production, repair, and commercialisation of components for sectors ranging from steelworks to refineries, SERMEC II plays a pivotal role in the current railway project [5]. Its responsibilities include project management, the design and development of the carriage body, and the secondary structure for subsystem interfaces, such as the train floor. Additionally, SERMEC II oversees the transformation of raw materials through machining, laser cutting, and welding, as well as the final assembly of the vehicle [6].

It is in this specific context of structural fabrication that this thesis is positioned. This study focuses on the testing and analysis of welded joints intended for application in the train floor structure under construction by SERMEC II.

1.2 Objectives

This dissertation aims to evaluate the metallurgical characteristics and mechanical properties of dissimilar welded joints produced by Gas Metal Arc Welding (GMAW), and to correlate these results with the manufacturing process parameters, in order to guarantee the quality of welded structures, specifically for application in the train floor structure.

To achieve this main goal, the following specific objectives were defined:

- To evaluate the condition of raw materials through chemical analysis, metallographic examination, and mechanical characterisation;
- To characterise the fusion zone (FZ), heat affected zone (HAZ) and base metal of the joints, using metallographic preparation and optical microscopy;
- To compare the mechanical properties of each joint to identify significant differences;
- To select the most suitable filler metal (FM) for the application.

1.3 Dissertation's Structure

In addition to this introductory chapter, which establishes the research scope and objectives of the work, the dissertation is organised into four additional chapters. Chapter 2 provides a comprehensive literature review regarding structural steel S355J2 and stainless steel AISI 301LN, examining their metallurgical welding behaviour, process related defects, corrosion susceptibility, and mechanical properties. Chapter 3 outlines the methodology employed in this study to achieve the previously defined objectives. Chapter 4 presents the results of all activities, aiming to address the research questions that guide this dissertation. Lastly, Chapter 5 summarises the main findings and final considerations of this investigation.

2. Literature Review

This chapter provides an overview of the steels AISI 301LN and S355J2, focusing on their properties and weldability. It also addresses the GMAW process, highlighting the key parameters of the process. The chapter then transitions to the challenges associated with dissimilar joints. Finalises with fatigue in railway vehicles.

2.1 Base Materials and Weldability

2.1.1 Steel AISI 301LN (EN 10088-2:2005)

The steel AISI 301 LN (EN 10088-2:2005), also known as X2CrNiN18-7, is classified as an austenitic stainless steel, containing a minimum of 11% chromium, which forms a passive Cr_2O_3 film, that gives a good corrosion resistance [7–10]. The austenitic stainless steels are non-magnetic and have a face-centred cubic (FCC) structure, which confers exceptional mechanical properties, weldability, and castability, fundamental to their use in various areas [11–13].

AISI 301 LN stands out as a "metastable austenitic steel" due to its low austenite-stabilising elements content, which enables it to exhibit the Transformation Induced Plasticity (TRIP) effect during plastic deformation, resulting in a superior balance between high work-hardening rates and ductility [14]. These mechanical properties are governed by its low stacking fault energy and the stability of the austenitic phase, which, under mechanical or thermal deformation, can transform into deformation-induced martensite (DIM), significantly raising the yield strength [14,15].

In addition to good mechanical properties, austenitic stainless steels are known for their corrosion resistance; in this case, the low carbon content minimises the risk of chromium carbide precipitation at grain boundaries, thereby preventing sensitisation and intergranular corrosion [16,17]. Furthermore, the presence of nitrogen improves resistance to localised corrosion such as pitting, making this steel suitable for operation in aggressive environments [17,18]. The presence of nitrogen in its composition also reinforces the austenitic matrix through solid-solution strengthening and compensates for the lower nickel content, ensuring austenite stability [19]. New studies have shown that nitrogen improves the fatigue resistance of austenitic stainless steels. This is achieved through more planar slip and homogeneous deformation, driven by dislocation interactions and a reduction in stacking fault energy. Consequently, this planar slip mitigates strain localisation, hinders the formation of persistent slip bands, and increases slip reversibility, all of which effectively delay crack initiation [20]. Nickel and manganese are also fundamental to stabilise austenite and prevent hot cracking, and carbon is kept at low levels to ensure intergranular integrity [13–15]. The influence of alloying elements is decisive for the mechanical properties and corrosion resistance. The chemical composition of this steel is shown in Table 1, and its C1000 and C850 grades refer to the tensile strength levels [10,21].

Table 1: Chemical composition of AISI 301 LN (wt.%) [21].

	C (%)	Si (%)	Mn (%)	P (%)	S (%)	Cr (%)	Ni (%)	N (%)
AISI 301 LN	0.03	1.00	2.00	0.045	0.015	16.50-18.50	6.0-8,0	0.10-0.20

These steel grades are characterised by a high coefficient of thermal expansion and low thermal conductivity. During heating processes, such as welding, the material expands while heat dissipation is restricted. This results in a steep thermal gradient, rendering the component highly susceptible to structural distortion [12].

2.1.2 Welding of austenitic stainless steel

Most austenitic stainless steels are weldable and produce highly ductile joints, with the notable exception of AISI 303. In austenitic stainless steel welds, there are four distinct modes of solidification, and they depend on the ratio between chromium equivalent (Cr_{eq}) and nickel equivalent (Ni_{eq}). The austenitic mode (A) results in a fully austenitic microstructure because the primary phase forming immediately after the liquid state is exclusively austenite. Whilst the austenitic-ferritic (AF) mode shares this same primary phase but allows a small portion of ferrite to form during the subsequent cooling [22]. Conversely, as the ratio of the Cr_{eq} to the Ni_{eq} increases, the solidification shifts towards the ferritic-austenitic (FA) mode, where the primary phase is ferrite and austenite only forms in the final stages of solidification. Ultimately, to the fully ferritic (F) mode where ferrite remains the dominant primary phase [22]. The more advantageous mode is the ferritic-austenitic, where the low-melting-point liquid phase does not wet the interphase boundaries as easily as it would in mono phases, thereby providing a higher resistance to solidification cracking [23]. In the case of the AISI 301 LN, which predominantly solidifies via the FA mode, the material exhibits high sensitivity to the local welding conditions. A high cooling rate can force a transition to the AF mode [24]. However, whilst these distinct modes of macro solidification exist and can be strategically targeted, it is important to note that a single weld can still exhibit various distinct ferrite morphologies, due to local variations in the chemical composition across the molten pool [22].

Building upon these previously established solidification modes, the microstructural evolution of the weld metal heavily dictates its ultimate mechanical integrity. When austenite acts as the primary phase, the deposited metal may be fully austenitic under mode A, or it may solidify under mode AF, which typically contains a small volumetric fraction of eutectic ferrite distributed along the solidification grain boundaries [12]. Conversely, when ferrite is the primary phase under mode FA, a solid-state transformation occurs during cooling via an invariant peritectic or eutectic reaction, forming austenite along the grain boundaries whilst leaving a residual ferrite content [12]. The morphology of this δ ferrite is linked to the solidification pathways; whilst mode AF produces eutectic ferrite, mode FA predominantly generates a vermicular morphology, which is the most observed structure in austenitic stainless steel welds [12,24,25]. Furthermore, if the weld is subjected to rapid cooling, the primary ferrite can manifest as acicular ferrite, characterised by needle-like structures containing both vermicular and acicular formations [18,25].

The presence and morphological distribution of this δ ferrite are of paramount importance because fully austenitic filler metals exhibit a dangerously high tendency for hot cracking [26]. Ensuring the retention of an adequate amount of ferrite within the microstructure effectively prevents this catastrophic defect [26–28]. This protective mechanism occurs primarily because detrimental impurities like phosphorus and sulphur possess a significantly higher solubility in ferrite than in austenite; the ferrite safely dissolves these elements, thereby preventing their harmful segregation into low-melting-point compounds [29,30].

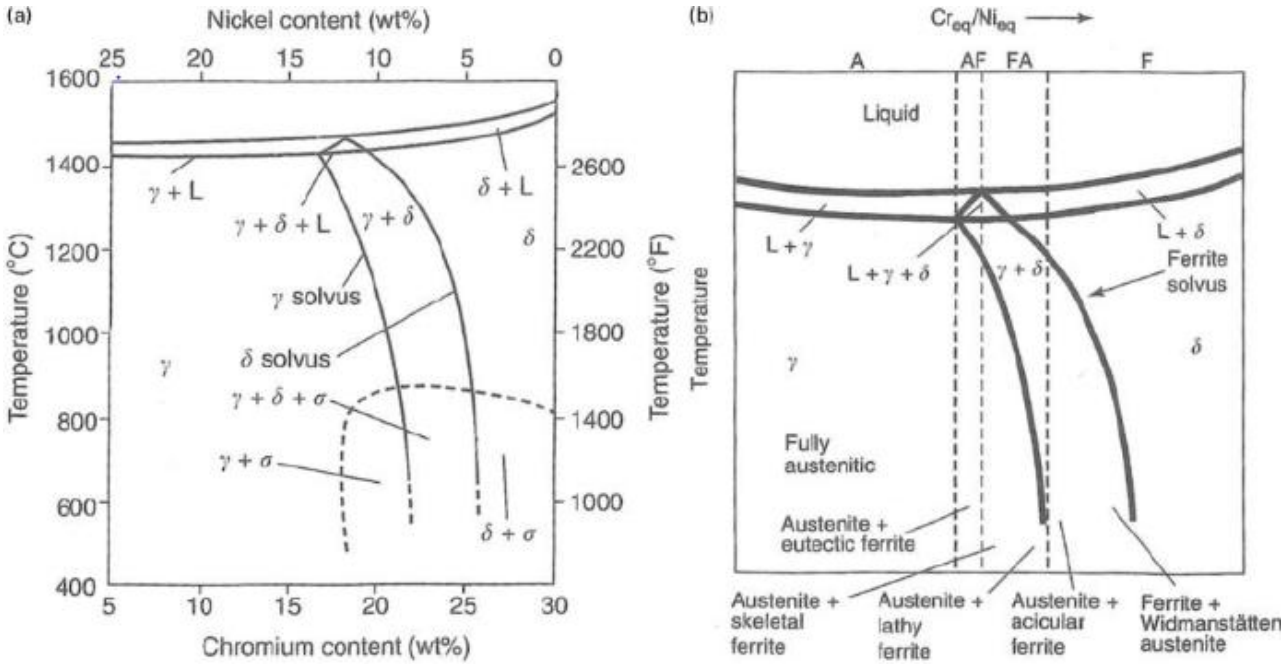


Figure 1:(a) Vertical section of the Fe-Cr-Ni phase diagram at a constant 70 wt-% Fe. (b) Schematic representation of the various types of primary phase solidifications (A, AF, FA, and F) as a function of composition (Creq/Nieq ratio) [22].

Figure 2 illustrates two distinct microstructures of an austenitic stainless steel, highlighting the characteristic morphology of the δ ferrite formed under different solidification modes.

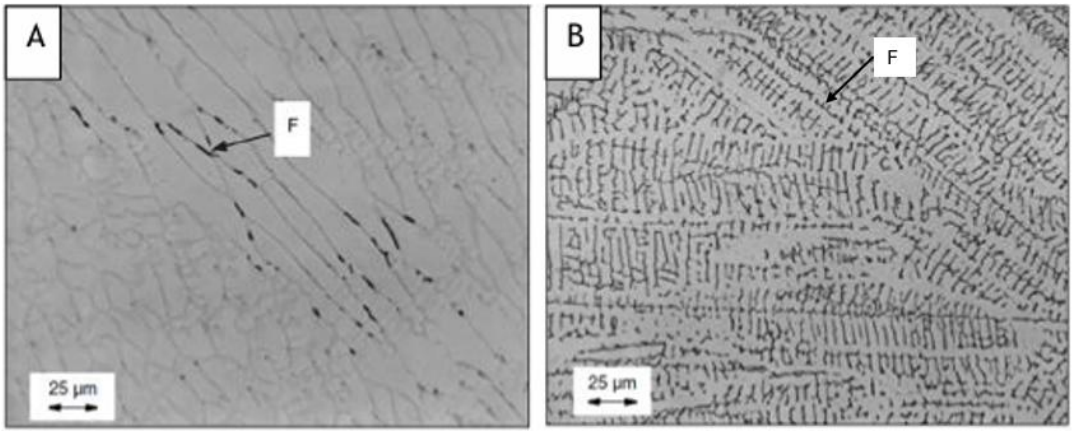


Figure 2: Microstructures of an austenitic stainless steel. (A) AF mode; (B) FA mode [22].

2.1.3 Steel S355J2 (EN 10025-2:2004)

The structural steel S355J2 (EN 10025-2:2004) is classified as a high-yield non-alloy carbon-manganese (C-Mn) steel. It is widely used in sectors such as civil construction, pipeline manufacturing and the transport sector [7,31]. S355J2 steel presents a minimum yield strength of 355 MPa for sections with a thickness below 16mm, in the annealing state and a minimum impact toughness of 27 J at -20ºC [32]. The chemical composition of this structural steel is presented in Table 2.

Table 2: Chemical composition S355J2 (wt%) [32].

	C (%)	Si (%)	Mn (%)	P (%)	S (%)	Cu (%)
S355 J2	0.20	0.55	1.60	0.025	0.025	0.55

The microstructure depends heavily on the cooling rate to which the material is subjected, potentially leading to different constituent phases, as illustrated in Figure 3 [33].

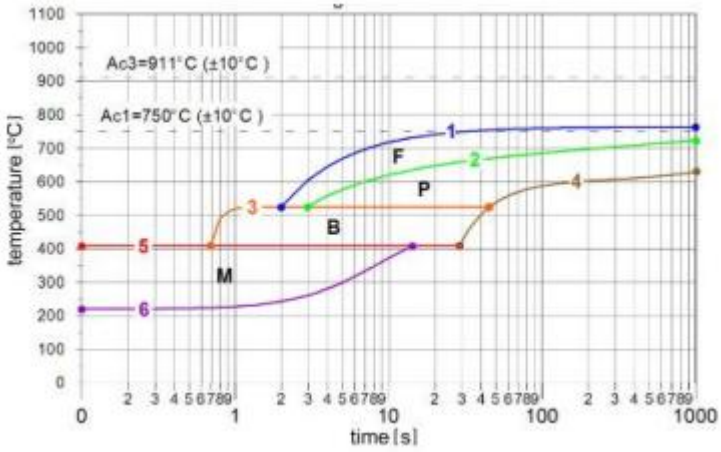


Figure 3: CCT diagram of S355 steel [33].

Even though its chemical composition, this steel is usually classified as an unalloyed steel. The presence of copper contributes to the improvement of mechanical properties through precipitation hardening within the ferritic matrix [34]. However, the introduction of alloying elements to optimise corrosion resistance or to enhance mechanical strength ultimately affects the steel's weldability [35]. In the context of C-Mn steels, such as S355J2, this assessment is performed using the Carbon Equivalent (CE) index, which weighs the combined influence of carbon and the other alloying elements, as expressed in Equation 1[36].

$$\mathrm{CE} = C + \frac{Mn}{6} + \frac{Cr+Mo+V}{5} + \frac{Cu+Ni}{15} \qquad \text{(Eq. 1)}$$

For the steel S355J2, this parameter is between 0,45 and 0,49, varying according to the plate's thickness [32]. Whenever the carbon equivalent index reaches or exceeds 0,50%, the adoption of special welding procedures is required [35]. Such as preheating the base metal may be justified, this practice slows down the cooling rate of the joint after welding, considerably mitigating the risk of forming brittle microstructures susceptible to cracking. Another approach is the use of post-weld heat treatments for stress relief, aiming to dissipate the residual stresses induced by the thermal cycle [37].

2.1.4 Welding of carbon steel

Every arc welding process is likely to generate a severe temperature gradient spanning from the melting point to ambient temperatures [38]. Due to these thermal changes, in the case of carbon steel, a specific HAZ is created, which can be divided into distinct subzones exhibiting fundamentally different microstructures and properties. The first of these subzones is the Coarse Grained Heat-Affected Zone (CGHAZ), where peak temperatures rise above the Ac3 critical point, resulting in the formation of coarse austenite grains [39]. Adjacent to this is the Fine Grained Heat-Affected Zone (FGHAZ), where temperatures reach up to the Ac3 point, leading to the development of smaller

austenite grains [39]. Further outward, the material enters the Inter-Critical Heat-Affected Zone (ICHAZ), which experiences temperatures between the Ac3 and Ac1 points; this causes partial austenite transformation during heating, creating a region that usually has the lowest hardness within the joint [39]. The outermost region is the over-tempered zone, where peak temperatures remain strictly lower than the Ac1 point; because the heat is insufficient to trigger a full phase transformation, the existing microstructure merely undergoes a tempering effect accompanied by the coarsening of precipitation [39].

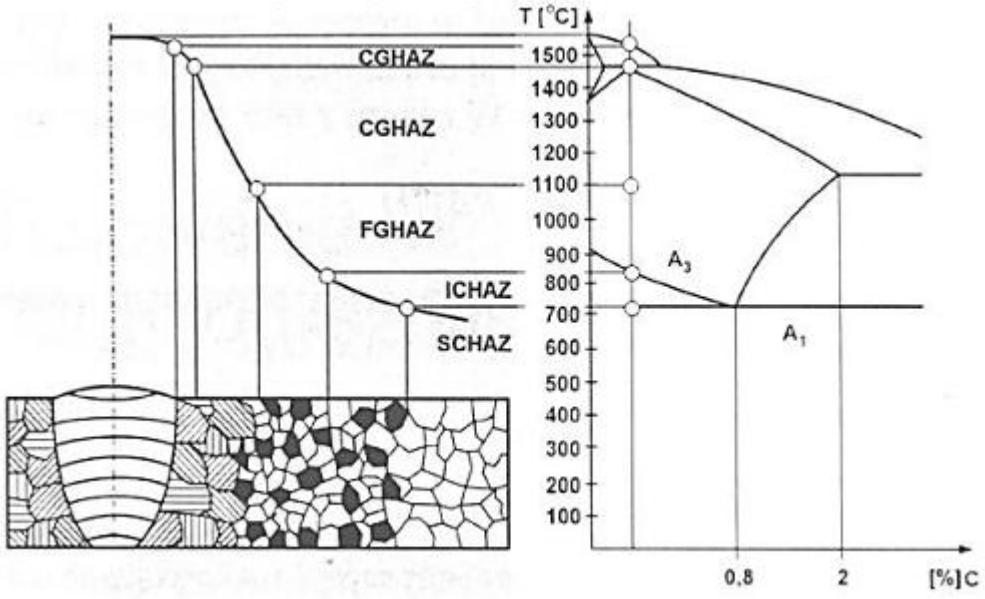


Figure 4: Sub-regions of the HAZ in the Fe-C diagram [30].

In the case of low-carbon steel, the thermal cycles bring another problem by the formation of diffusion less hard structures, such as bainite and martensite, in the weld metal and the HAZ, resulting in significant volume changes and internal instability [40]. The addition of alloy elements is crucial in this process, such as carbon, silicon, and manganese, as reduces the martensite start temperature. Although these stresses cannot be eliminated, optimising the welding sequence is identified as the simplest and most productive method [40].

2.2 Welding

A wide range of metal joining techniques is available, including adhesive bonding, brazing, mechanical joining, and welding, with welding being the most used technique [41]. According to ISO 25901, welding is a process whereby two or more components are permanently joined to establish continuity in the properties across the workpiece material(s), by the application of heat, pressure, or a combination of both, with or without the utilisation of a filler material [42]. The welding process may also rely on shielding gases, welding powders, or pastes, among other aids, with the necessary external energy sources, electrical, chemical, or optical inputs [41]. Welding processes are typically divided into two major categories: pressure welding and fusion welding. Pressure welding does not use filler materials; instead, the joint is formed through the application of pressure, sometimes combined with heat, while keeping the temperature below the melting point of the base metals. In contrast, fusion welding requires melting the base materials; a filler material may be added to the molten pool to enhance the process, adding extra mass and strength to the weld [43].

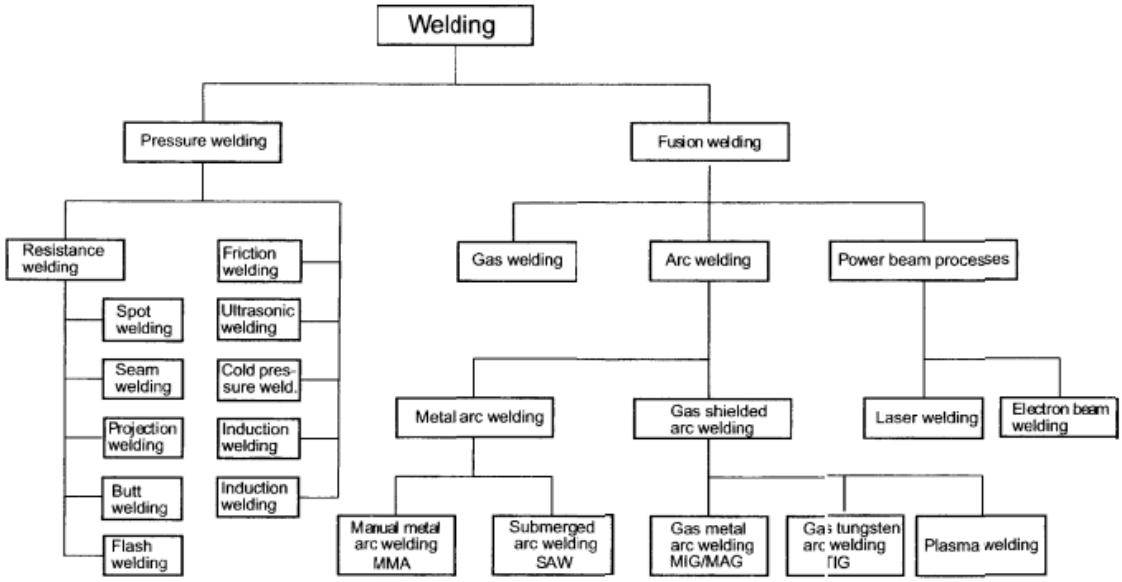


Figure 5:Types of welding processes [44].

This dissertation focuses exclusively on gas metal arc welding, which was the welding method employed.

2.2.1 Gas Metal Arc welding

GMAW is recognised as the leading welding process in most industrialised countries and is widely used for joining dissimilar materials, including carbon steel and stainless steel [25,45,46]. This technique encompasses two methods: Metal Inert Gas (MIG), which employs an inert shielding gas, and Metal Active Gas (MAG), which uses an active shielding gas. MIG welding is particularly suitable for non- ferrous metals such as aluminium and copper [47]. Conversely, MAG welding is the preferred choice for ferrous metals and is extensively applied in pipe welding, shipbuilding, bridges, and pressure vessels [48,49]. Additionally, MAG is often selected because $C0_2$ is significantly less expensive than argon, the shielding gas typically used in MIG welding [47]. The significant advantages of the GMAW technique include the ability to weld steel, aluminium, and copper; the capacity to handle a wide range of thicknesses (>30mm); and its suitability for all welding positions [46–50].

Since GMAW is a fusion welding technique, the base materials (BM) melt locally, forming the Fusion Zone (FZ). This region solidifies with a cast microstructure whose properties depend on the thermal cycle and chemical composition. Near the FZ lies the HAZ, where the material does not melt but undergoes significant microstructural transformation due to exposure to elevated temperatures [51].

The MIG/MAG welding process is based on an electric arc formed between the workpiece and a continuously fed consumable electrode. The electrode wire is normally connected to the positive terminal of the power source, while the workpiece is connected to the negative terminal [46]. This configuration, known as Direct Current Electrode Positive (DCEP), provides a stable arc, low spatter, and good penetration. When the poles invert, Direct Current Electrode Negative (DCEN), the arc becomes unstable and produces larger droplets; this polarity is rarely used [52]. The shielding gas protects both the arc and the weld pool as it flows through the welding gun [46]. As the wire is fed, this technique is automatically considered semi-automatic and requires less operator skill [50].

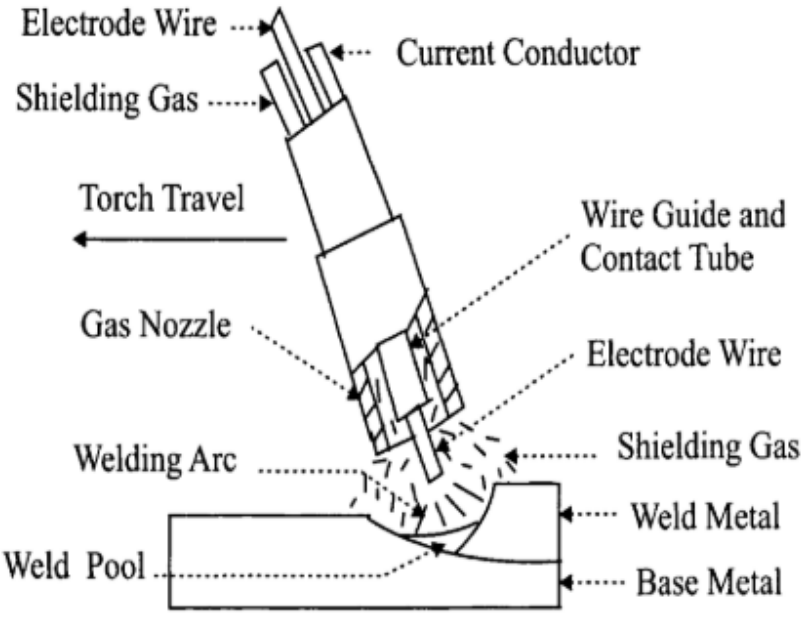


Figure 6: Simple diagram of the gas metal arc welding process [52].

This process has three main transfer modes: globular, spray and short-circuit transfer. In the globular transfer mode, the FM forms large droplets, bigger than the wire diameter, making it suitable only for flat and horizontal positions [52,53]. This mode uses an intermediate current level, lower than spray mode, but higher than that in short-circuit transfer [52]. The spray transfer mode utilises higher current levels, producing small droplets that result in a highly stable, spatter-free arc [53]. Finally, the short-circuit transfer mode employs the lowest current values, generating minimal heat input, producing small droplets and fine spatter, making it ideal for thin sections [46,52,53].

As with other welding processes, it is essential to define the operating parameters: voltage, current and wire-feed speed. Voltage controls the arc length; increasing the voltage widens the arc cone, resulting in a wider weld bead. The current is associated with the wire-feed speed (WFS), higher WFS means an increase in the energy input and current density, resulting in faster electrode melting and deeper weld penetration. Travel speed is also a parameter that plays a critical role, but this one is controlled manually by the welder and functions independently of the power source settings. However, a higher travel speed reduces the linear heat input, producing narrower weld beads with less penetration [52].

These welding processes utilise a specialised power source that provides a Constant-Voltage (CV) output. When paired with a constant-speed wire feeder, this configuration promotes a self-regulating arc. A graphic of this power source characteristic is shown in Figure 3. The self-regulation mechanism ensures that if the arc length changes momentarily during operation, the current adjusts automatically.

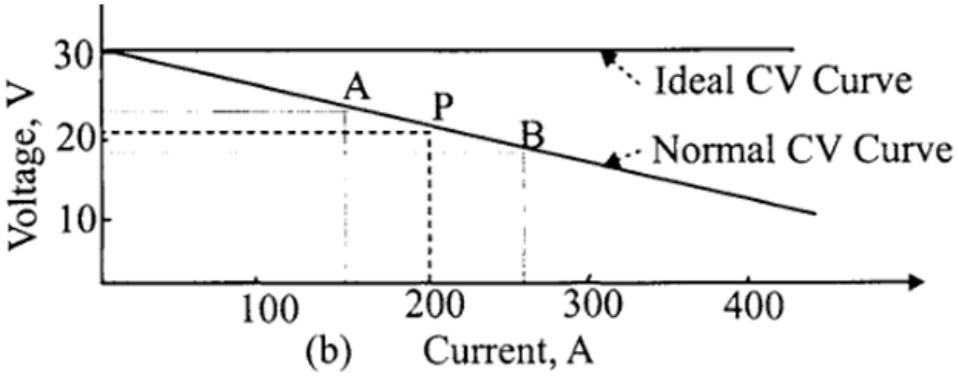


Figure 7:Volt-Ampere Curve for a constant voltage power source [52].

2.2.2 Shielding Gases

Although a wide variety of shielding gases can be used in GMAW, argon, carbon dioxide, helium, and oxygen are the most common choices for welding carbon and stainless steels. These gases are selected based on their specific properties. Argon is utilised because it provides an excellent arc stability and good penetration, producing a characteristic finger-shaped penetration profile due to the high current density of the arc. Carbon dioxide is widely used for welding carbon steels; however, it tends to generate more spatter and produce weld surfaces with less regularity. Helium offers higher thermal conductivity, increasing heat input while maintaining an inert atmosphere [54].

Another option is that gas mixtures are frequently employed to optimise weld quality. Argon-oxygen blends increase the droplet transfer rate and create a more fluid weld pool, resulting in wider weld beads. Argon-carbon dioxide mixtures are common in welding carbon and low-alloy steels, and higher carbon dioxide content generally increases penetration. The combination of these gases can be used in short-circuit, globular, and spray transfer modes for both structural steel and austenitic stainless steel. In the case of argon-carbon dioxide-hydrogen mixtures are used for austenitic stainless steel, but due to the presence of hydrogen, they must not be used for carbon steels [54].

2.2.3 Plug welds

Plug welding is a type of joint typically used to join one board to another in a lap joint configuration, where one of the boards features prefabricated through-holes. This method has gained widespread applications owing to its high strength, excellent sealing performance, and superior surface quality [40]. This joining method involves depositing filler metal into the pre-drilled holes, generating a continuous structural bond that fuses the inner walls of the upper plate with the surface of the bottom plate. In the railway industry, the body structure of passenger carriages is frequently manufactured by welding materials of various compositions and thicknesses. In these scenarios, plug welding is used in areas where traditional spot welding is difficult to apply, such as the structural components [40].

To ensure the structural integrity of the joint, the geometric configuration of the plug weld must adhere to strict guidelines. In accordance with the AWS D1.1 code, there are specific limitations regarding the dimensions of the prefabricated holes. The minimum diameter of the plug weld hole must be no less than the thickness of the part in which it is made. Additionally, the maximum diameter of the hole shall not exceed the minimum diameter plus 3 mm or 2.25 times the thickness of the part, whichever is greater [55].

Current research on plug welding joints has primarily focused on their fundamental mechanical properties, through tensile and shear tests to obtain the failure load and tensile strength, the yield strength and tensile strength of the plug welded joint. The failure modes of the specimens included pull-out fracture, thickness fracture, and ductile fracture. However, the change of welding parameters, thickness and different hole diameters makes the comparability impossible.

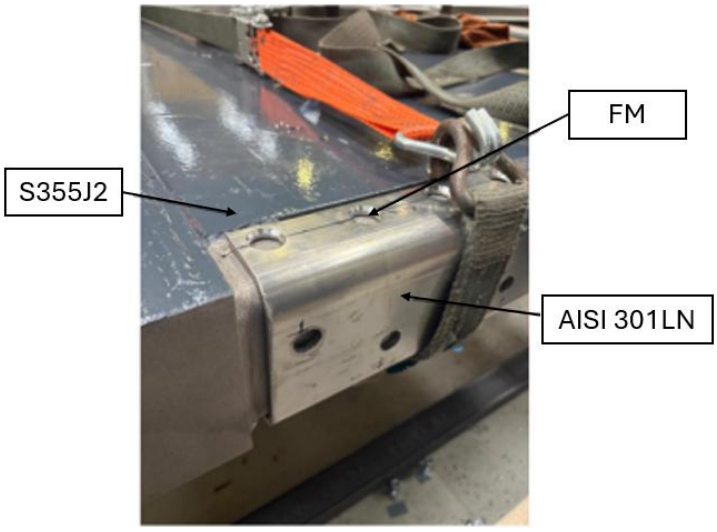


Figure 8: Dissimilar metal plug welding configuration with the identification of the different materials involved (own source).

2.3 Challenges of joining material

2.3.1 Welding dissimilar materials

The primary objective of joining different materials, such as welding an austenitic stainless steel onto a carbon steel, is to strategically combine specific properties like corrosion resistance with structural strength and cost efficiency [26,56,57]. However, achieving a high quality structural connection is fundamentally complicated by differing physical properties; a significant thermomechanical challenge arises, for example, stainless steel possesses a 50% higher coefficient of thermal expansion and a 40% lower coefficient of thermal conductivity compared to carbon steel [27].

The intense thermal gradients required to fuse these dissimilar materials also create profound microstructural challenges, where peak temperatures reach between 750 ºC and 900ºC, leaving the HAZ structure in a partially austenitic domain. The specific austenite formed in this intermediate region possesses a highly elevated carbon concentration, changing its transformation behaviour during the subsequent cooling phase [58,59]. If the cooling rate is not strictly controlled, this highly hardenable, carbon enriched austenite will rapidly decompose into non-equilibrium, brittle phases such as martensite and bainite, creating localised fragile zones that undermine the mechanical integrity of the dissimilar joint [58–60].

Another critical phenomenon is dilution, because the liquid weld bead is formed by the fusion of the base metal combined with the filler metal; the composition and properties of the deposited layer are strongly influenced by how much they mix [61,62]. High dilution is a major challenge because it undesirably reduces essential alloying elements whilst simultaneously increasing the carbon content in the weld pool, drastically increasing the joint's susceptibility to hot cracking and compromising its corrosion resistance [56,57,63].

To mitigate all these phenomena, a post weld heat treatment (PWHT) at temperatures

between 550ºC and 675ºC is often required, but this thermal cycle introduces a new challenge by inducing intergranular corrosion in the stainless steel due to the precipitation of the chromium rich phases [12,38]. To help resolve these metallurgical challenges, dissimilar welding relies on the precise selection of filler metals with high alloy contents, such as ER308, ER309, ER312, ER316, or ER347 [38,63]. These specific chemical compositions are crucial because they actively inhibit the formation of brittle martensite whilst promoting the formation of ferrite within the weld pool, safely incorporating problematic impurities such as sulphur and phosphorus to successfully prevent hot cracking in the highly stressed fusion zone [39,51,64].

Such as the other arc welding, plug welding involves rapid heating and cooling thermal cycles that generate inevitable residual stress, which are defined as internal forces that remain in a component after the welding process [40]. During the welding process, a filler metal is deposited along the joint in liquid form. As this material attempts to expand, the surrounding cold base material restrains it, creating initial compressive forces [65–67]. Subsequently, during the cooling phase, the metal in the fusion zone attempts to contract but is once again restricted by the rigid base material, generating severe residual tensile stresses [65–67].

2.2.2 Microstructural prediction

Predicting the microstructure of the weld metal relies on established constitution diagrams, such as the Schaeffler, DeLong, and WRD-1992 diagrams, which utilise the fundamental concepts of chromium and nickel equivalents. Within these predictive models, elements such as molybdenum, silicon, and niobium act similarly to chromium in stabilising ferrite, and are consequently incorporated into the Cr_{eq} equation. Conversely, elements such as carbon, nitrogen, copper, and manganese act like nickel in stabilising austenite and are therefore included in the Ni_{eq} equation [29].

The Schaeffler diagram serves as an indispensable guide for relating these elemental variations to the predicted microstructure of the weld metal [28,68]. This specific diagram comprises structural fields and lines indicating the ferrite content; the Ni_{eq} on the y-axis promotes the formation of an austenitic structure and is known as a gamma-genic element; the Cr_{eq} on the x-axis promotes a ferritic structure and is characterised as an alpha-genic element [52]. The Schaeffler diagram predicts the resulting microstructure based on the chemical composition of both the base materials and the filler material, allowing a more accurate choice of the filler material through comparison.

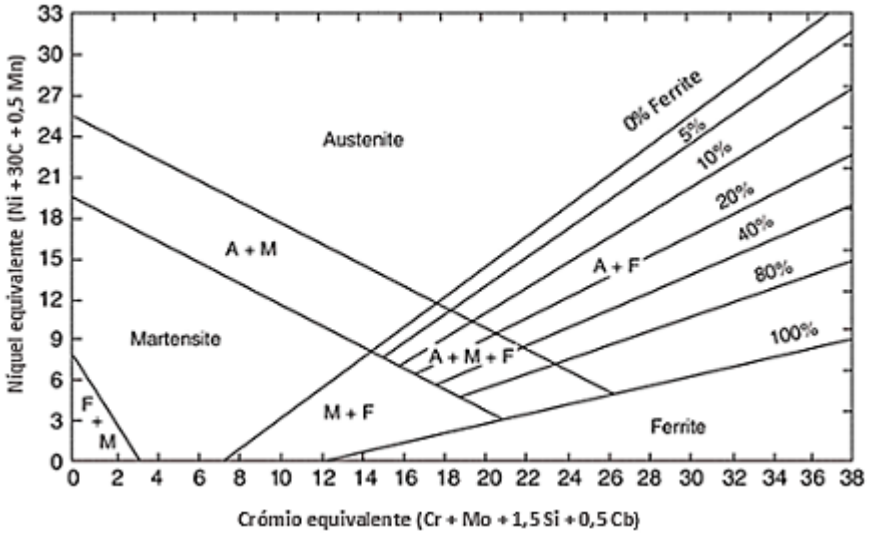


Figure 9: Schaeffler diagram [68].

Evolving from this foundational tool, the DeLong diagram represents a more targeted 3xx series stainless steel. Finally, the WRC-1992 diagram allows prediction of ferrite content [11].

Beyond theoretical predictions of microstructures using these diagrams, industrial applications frequently employ multi-pass welding procedures, which involve repeated thermal cycles with each successive pass [69]. While these overlapping thermal cycles introduce changes in microstructure, hardness, and mechanical properties of the weld, they offer distinct metallurgical advantages [69]. The heat applied during subsequent passes can effectively reduce accumulated residual stresses and lower the required energy input per pass, thereby strategically limiting excessive grain growth [70].

Stainless steel tends to introduce a distinct microstructural evolution, notably driving a transition in the ferrite phase from a cellular morphology to a columnar dendritic structure [69].

2.2.3 Welding Defects

In engineering, any physical interruption in the uniform structure of a weld is classified as a discontinuity, meaning that whilst all welds may contain flaws, these are not immediately considered defects. To properly evaluate structural integrity, a defect is defined as a discontinuity or cluster of discontinuities that exceeds the maximum acceptance limits and renders a structure incapable of meeting minimum specifications, ultimately leading to component rejection [71]. The quality of a welded joint is established by its service requirements, encompassing chemical composition, mechanical properties, and hardness [72].

Welding defects can be broadly categorised into two types, the first of which stems from inadequate welding parameters or operator skill. A common operational defect is an undercut, which manifests as depressions running parallel to the weld bead. This type of defect is typically caused by improper welding technique and by the application of excessively high electrical current and voltage [71,72]. Depending on its dimensions, this depression acts as a severe stress concentrator that drastically reduces the fatigue properties of the joint due to the sharp-notch effect it produces [71,72].

Another very common defect that can result from poor technique is porosity or slag inclusions. Porosity consists of the formation of spherical cavities resulting from the entrapment of gases during the solidification of the weld metal [71,72]. While sim is not a serious problem under normal loading conditions, porosity can serve as a crack initiation site if the joint must resist brittle fracture at lower temperatures. Similarly, slag inclusions occur when solid process particles become trapped within the joint instead of safely floating to the surface [72].

Some defects occur due to poor definition of welding parameters; specifically to lack of fusion and incomplete penetration, both of which are critical structural defects. The lack of fusion occurs when there is a failure of the connection between the base metal and the filler metal, or even between successive weld layers, and is associated with insufficient electrical current [71,72]. On the other hand, a lack of penetration is caused by insufficient heat input and improper joint design [72].

The other type is more related to the metallurgical bond between the materials. Cold cracking is a type of defect that can appear within hours to several days after welding is completed. This defect is dependent on three factors: the existence of phase fragilis (martensite), the presence of dissolved hydrogen, and the presence of internal tensions [73]. As the metal transforms, the solubility of hydrogen decreases, creating diatomic hydrogen molecules that create a massive internal pressure that tears the rigid material

apart [21,73,74]. Mitigating this risk requires control of the carbon equivalent and the application of low-hydrogen consumables, as well as proper pre-heating to remove moisture or post-heating below the martensite finish point to allow hydrogen diffusion [74,75].

Conversely, hot cracking, or solidification cracking, is frequently associated with austenitic stainless steels and occurs at elevated temperatures during or shortly after solidification [45,72]. This defect is driven by the segregation of low-melting-point eutectics, composed of impurities such as sulphur and phosphorus, which lack mechanical strength and are pushed towards the centre of the weld pool to withstand cooling stresses, causing the joint to tear apart from the inside [30,72]. This defect can be mitigated by employing slower welding speeds to shift the solidification front and ensure the sulphur content is strictly limited. And adding manganese to form stable compounds [21,30,76].

Stress-corrosion cracking occurs in austenitic stainless steel; this complex cracking mechanism propagates either intergranularly or transgranularly through the material, with transgranular cracking typically observed in chloride and caustic media. This type of cracking is initiated by high residual stress concentrations there [11]. Ultimately, the accumulation of these defects and internal stresses reduces the fatigue limit of the welded joint, lowering its fatigue strength below that of the base material and leading to premature structural collapse [40].

2.2.4 Corrosion behaviour of dissimilar welding materials

The corrosion behaviour of dissimilar joints between low-carbon steels and austenitic stainless steels is among the most complex themes in structural integrity, since the direct union of these two metallurgical systems introduces pronounced chemical and microstructural discontinuities that drastically alter local passivation mechanisms [77–80]. This vulnerability manifests immediately at the fusion line and joint interfaces, where the abrupt chemical transition between the ferritic–pearlitic matrix of the low-carbon steel, which lacks protective alloying elements, and the chromium and nickel rich matrix of the austenitic stainless steel establishes a marked macroscopic galvanic couple [77,78]. This chemical transition inevitably extends into the HAZ on the low-carbon steel side, where the thermal cycle of welding acts synergistically with filler-metal dilution, causing the chromium content to decrease progressively beyond the fusion line and giving rise to a sub-region whose chromium content falls below the critical passivation level [77,79]. In parallel with, yet metallurgically distinct from, the degradation observed on the carbon-steel side, the austenitic stainless steel HAZ undergoes its own intergranular failure mechanism, sensitisation [79].

Taken together, these mechanisms show how corrosion susceptibility varies across the joint. Filler-metal selection plays a central role in this variation; appropriately selected consumables confer greater chemical stability and a higher corrosion resistance on the weld metal [77–80]. The carbon-steel HAZ remains particularly vulnerable owing to its chemical composition [77,78]. The austenitic stainless steel HAZ is also weakened through sensitisation-induced intergranular corrosion [79]. The weld metal, by contrast, tends to be the most corrosion-resistant region of the joint [77–80].

2.3 Fatigue in welded structures for railway vehicles

Fatigue can be defined as the "localised damage process of a material produced by cyclic loading" [81–83], a critical phenomenon in structural elements such as railway carriages, which experience continuous dynamic loads from movement, vibration, and passenger weight [81,82,84]. In this structure, welded joints are highly susceptible to stress concentrations that can lead to fatigue crack initiation and propagation [41]. This vulnerability is exacerbated by welding defects, distortions, and the metallurgical complexity arising from the combination of dissimilar chemical compositions [71,83,85].

The fatigue process can be described in three distinct phases: crack initiation, crack propagation, and final fracture. Initiation typically occurs in a shear plane near a high-stress concentration, where cyclic plastic deformation produces slip-band cracking at the microstructural level; in the case of welded joints, this brief initiation phase is strongly influenced by residual stresses and the geometric discontinuities inherent to the weld toe or root [84,86]. This initial, microscopically driven growth is classified as stage I propagation and is governed by shear stresses acting on the crystallographic slip planes, which predominantly correspond to mode II loading [87]. As the crack extends beyond the first few grains, it transitions into stage II propagation, where growth becomes macroscopic and is governed predominantly by the tensile stress acting perpendicular to the crack plane, corresponding to mode I loading. This stage accounts for the largest portion of the crack growth life and produces the characteristic striations visible on the fracture surface, each representing the advance of the crack front during a single loading cycle [87]. A third loading mode, mode III, may also contribute in cases of multiaxial or non-proportional loading, although mode I is generally dominant in welded joints due to the orientation of the weld toe relative to the principal stress direction [88].

Ultimately, failure occurs when the remaining, uncracked cross-section becomes unable to sustain the applied load and fractures in a final, unstable event. Analysed fracture surfaces typically display three characteristic regions: radial marks or a smooth area indicating the initiation site, propagation lines reflecting the stage II growth direction, and a final fracture region whose morphology is ductile or brittle, depending on the material, the remaining load-bearing area, and the loading rate at final failure [89,90].

Fatigue can be classified into two regimes: low-cycle fatigue (LCF), limited to below 10^5 cycles, in which significant plastic deformation occurs and crack propagation plays a more significant role in the total life; and high-cycle fatigue (HCF), generally exceeding 10^5 cycles, in which stresses remain predominantly elastic and the crack initiation period accounts for the largest share of the total fatigue life [84].The cyclic loading is characterised by parameters presented in Table 3.

Table 3: Equations to calculate test parameters

Stress amplitude (Sa)	$\mathrm{Sa} = \frac{(Smax - Smin)}{2}$	[86]
Mean stress (Sm)	$\mathrm{Sm} = \frac{(Smax + Smin)}{2}$	[86]
Stress ratio (R)	$\mathrm{R} = \frac{Smin}{Smax}$	[86]

Fatigue resistance is quantified using the S-N curve expression, following the Basquin law, which relates the number of cycles to the tension, defined by the equation:

$$logN = logC - mlog\Delta S$$

where ΔS is the stress range, N is the number of cycles to failure, m is the inverse slope of the S-N curve, and C is a constant dependent on the joint detail and material [86].

However, existing studies on plug-welded structures confirm that residual stresses significantly lower the joint's fatigue limit compared to the base material [35]. These studies have primarily generated isolated load-life (ΔF-N) curves based on specific parameters, including varying plate thicknesses and weld nugget diameters. Relying on this process is inefficient for engineering applications [41].

3. MATERIALS AND METHODS

This chapter presents the materials and methodology used in this dissertation. The chemical composition and mechanical properties of the steels applied are presented, and the expected microstructure of the weld metal was predicted using the Schaeffler diagram. The details of the welding procedure are also displayed. To evaluate the adequacy of the filler metals and welding parameters, a series of destructive tests, including tensile and fatigue tests, as well as macroanalysis, microanalysis, microhardness and corrosion tests, were performed.

3.1 Materials

3.1.1 Base Materials

The experimental study investigated dissimilar welded joints between AISI 301LN austenitic stainless steel and S355J2 structural steel. The stainless steel was utilised in two distinct conditions, namely C1000 and C850. The fundamental difference between these classifications lies in their minimum tensile strength, which is achieved through varying degrees of cold rolling. This mechanical process induces strain hardening and promotes the partial transformation of the metastable austenite into deformation induced martensite, elevating the material's tensile strength [14,15]. The chemical compositions are presented in Table 4.

Table 4: Chemical composition of base materials used [91–94].

	C	Mn	P	S	Si	Cr	Ni	N
AISI 301LN C850 (t=1,5mm)	0.021	1.19	0.030	0.002	0.44	17.6	6.6	0.15
AISI 301LN C850 (t=4mm)	0.016	1.22	0.035	0.003	0.59	17.5	6.6	0.15
AISI 301LN C1000 (t=5mm)	0.021	1.62	0.034	0.001	0.52	17.4	6.6	0.12
S355 J2 (t=8mm)	0.145	1.14	0.015	0.007	0.02	-	-	0.003

The weldability of steels is strongly correlated with their carbon equivalent value. The S355J2 steel exhibits a CEV of 0.33, indicating good weldability. Conversely, a CEV exceeding 0.50 necessitates special precautions, such as pre-heating treatments, to ensure joint integrity [95]. The mechanical properties of the base material are detailed in Table 5.

Table 5: Mechanical properties of base materials used [91–94].

	Rp 0.2 (MPa)	Rm (MPa)	A (%)
AISI 301LN C850 (t=1.5mm)	**635**	**885**	**37**
AISI 301LN C850 (t=4mm)	**648**	**903**	**38**
AISI 301LN C1000 (t=5mm)	**792**	**1041**	**26**
S355 J2 (t=8mm)	**482**	**569**	**23**

3.1.2 Filler Materials

In this study, two different filler materials were utilised: AWS A5.9 ER308LSi (1mm) and AWS A5.22 E309LMoT0-1/4 (0.8mm). These materials exhibit a significant difference in their chemical compositions, as presented in Table 6.

Table 6: Chemical composition of the filler materials used [96,97].

	C	Mn	P	S	Si	Cr	Ni	Mo	Cu	Co	N
ER308LSi	0.024	1.93	0.028	0.002	0.90	19.78	9.24	0.10	0.17	0.04	0.09
E309LMoT0-1/4	0.025	1.73	0.014	0.001	0.53	23.18	13.79	2.20	0.11	-	0.01

Alongside chemical compatibility between the base and filler materials, the mechanical properties of the consumables are crucial for ensuring the structural integrity and load-bearing capacity of the welded joint. The mechanical properties of the filler material are detailed in Table 7.

Table 7:Mechanical properties of filler metals used [96,97].

	Rp 0.2 (MPa)	Rm (MPa)	A (%)
ER308LSi	371	549	44
E309LMoT0-1/4	491	689	32

3.2 Methods

3.2.1 Test Specimens

The experimental procedure was divided into two distinct phases of specimen manufacturing. An initial series of test specimens was fabricated to establish the preliminary welding parameters and validate the design. Subsequently, based on the preliminary assessment, the final parameters and specimen geometry were defined and

manufactured for final experimental testing.

The initial set consists of six specimens, whose dimensions (thickness and plug hole diameter) are detailed in Table 8. The nomenclature adopted for each specimen indicates the base materials, their respective thicknesses, the filler metal employed, and the joint diameter.

Table 8: Experimental matrix, nomenclature and dimensions of the specimens.

	Thickness of AISI 301LN (mm)	Thickness of S355J2 (mm)	Plug hole diameter (mm)
Sample 1 – 301(0.8)355(8)308(LSi)_Plug 3	0.8	8	3
Sample 2 – 301(0.8)355(8)309(LMo)_Plug 3	0.8	8	3
Sample 3 – 301(4)355(6)308(LSi)_Plug 15	4	6	15
Sample 4 – 301(4)355(6)309(LMo)_Plug 15	4	6	15
Sample 5 – 301(5)355(8)308(LSi)_Plug 18	5	8	18
Sample 6 – 301(5)355(8)309(LMo)_Plug 18	5	8	18

To conclude the experimental matrix, a final set consisting of six newly manufactured specimens was introduced. Based on preliminary observations, it was deemed necessary to implement certain modifications to the initial specimen design before final testing. The underlying physical and mechanical justifications for adopting this optimised configuration will be extensively evaluated in the subsequent chapter. All pertinent information regarding the revised dimensions, base materials, and specific nomenclature is presented in Table 9.

Table 9: Final matrix, nomenclature and dimensions of the specimens.

	Thickness of AISI 301LN (mm)	Thickness of S355J2 (mm)	Plug hole diameter (mm)
Sample 7 - TS_01_308	1.5	8	10
Sample 8 - TS_01_309	1.5	8	10
Sample 9 - TS_02_308	4	8	15
Sample 10 - TS_02_309	4	8	15
Sample 11- TS_03_308	5	8	18
Sample 12 - TS_03_309	5	8	18

3.2.2 Welding Procedure

The welding process was MAG welding with a joint of plug weld and steel subgroup 1.2/8.1, according to ISO/TR 15608 [98]. This process was semi-automatic, and the different joints are presented in Figure 10. The shielding gas was ISO 14175-M12, containing 2% carbon dioxide and 98% argon [99]. The gas flow rate was maintained at a

constant 12L/min throughout the welding process. The procedure was carried out in the vertical position using direct current electrode positive (DCEP) polarity and a short-circuit metal transfer mode.

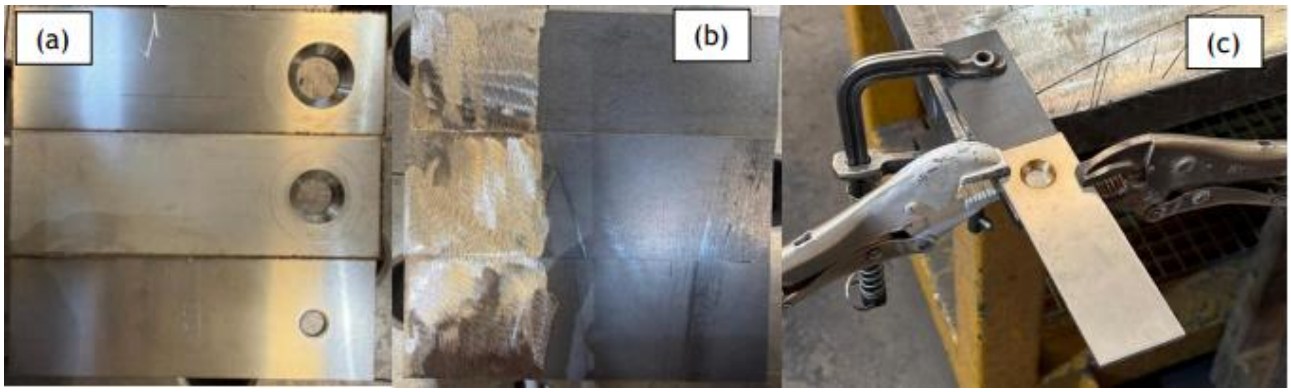


Figure 10: Experimental components and joint assembly for the dissimilar plug weld study. (a) Stainless steel AISI 301LN plates showing the variation in pre-drilled plug hole diameters. (b) Carbon steel S355J2 plates displaying the ground surface preparation on the left section. (c) Final welding setup: dissimilar lap joint assembly secured by clamps before the welding procedure.

As depicted in Figure 10(a), the AISI 301LN plates are presented in their final prepared state before the joining process. The preparation of these components involved several preliminary steps. Initially, the plug holes were machined into the sheet metal. In the cases of the greater thickness, the 4 mm and 5 mm plates were countersunk to improve torch access and facilitate the welding procedure. Ultimately, to eliminate any residual impurities or contaminants, the surfaces were thoroughly degreased with a solvent before welding. Conversely, the joining area of the S355J2 base plates is mechanically ground. This step ensures the removal of any existing surface impurities and superficial corrosion that may have developed. As previously stated, the welding procedure was performed in the vertical position. To firmly secure the two plates, several locking clamps were applied. This setup ensured strict parallelism between the components and prevented the plates from lifting or separating due to thermal distortion. The plug welds were fabricated in a single pass using a combined welding path. The operator first completed a continuous circular loop around the perimeter of the hole, followed immediately by a serpentine filling sequence to complete the deposition in the central core without interrupting the welding arc.

As previously stated, the experimental methodology comprised two distinct stages. The preliminary stage employed different base plate thicknesses than those used in the final configuration. Notably, the specimens in this initial phase did not feature countersunk holes. The operational welding parameters corresponding to this first phase are detailed in Table 10.

Table 10: First stage MAG welding operational parameters.

	Samples 1 and 2	Samples 3 and 4	Samples 5 and 6
Current (A)	150	172	193
Voltage (V)	20.5	22.9	23.4
Wire Speed (m/min)	7.8	9.0	9.7

The finalised welding parameters, established following the revision process to optimise the joint configuration, are presented in Table 11.

Table 11: Final stage MAG welding operational Parameters.

	Samples 7 and 8	Samples 9 and 10	Samples 11 and 12
Current (A)	80	180	190
Voltage (V)	17	22.8	22.8
Wire Speed (m/min)	6.0	9.0	9.0

3.3.3 Mechanical and Microstructure Characterisation of the welded joints

To conduct the macrostructural and microstructural analysis of the joint structure, the sectioning and final dimensions of the test specimens were established in accordance with the AWS D1.1 standard guidelines, as depicted in Figure 11.

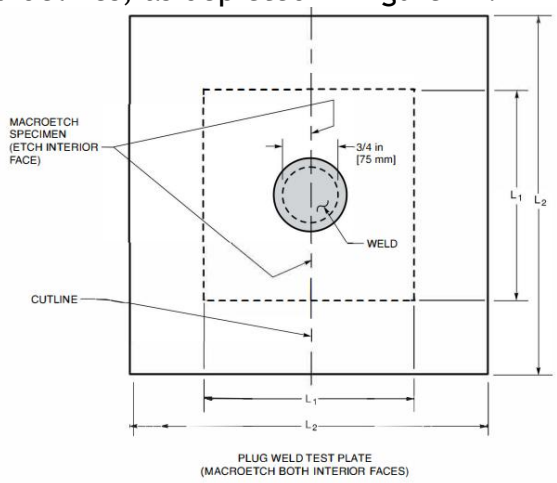


Figure 11:Schematic of the test specimen dimensions for plug joints, in accordance with the specifications of the AWS D1.1 standard [55].

3.3.3.1 Tensile shear tests

Tensile shear testing of the welded joints was performed in accordance with EN ISO 14273:2016 [100]. As in the welding procedure, tensile shear tests were conducted in different stages: initially, five specimens per condition were evaluated using the first set of welding parameters. Subsequently, for the final parameter configuration, three specimens per condition were tested, specifically utilising the AWS A5.22 E309LMoT0-1/4 (0.8 mm) filler. To guarantee strict alignment and maintain parallelism between the testing machine grips, spacer plates (shims) were employed. The precise geometric dimensions are detailed in Table 12 and illustrated in Figure 12.

Table 12: Dimensions of tensile test specimens, according to EN ISO 14273:2016 [100].

Thickness t mm	Overlap a mm	Specimen width b mm	Specimen length Ls mm	Free length between clamps Lf mm	Length of individual test pieces Lt mm
0,5 ≤ t ≤ 1,5	35	45	175	95	105
1,5 < t ≤ 3	45	60	230	105	138
3 < t ≤ 5	60	90	260	120	160

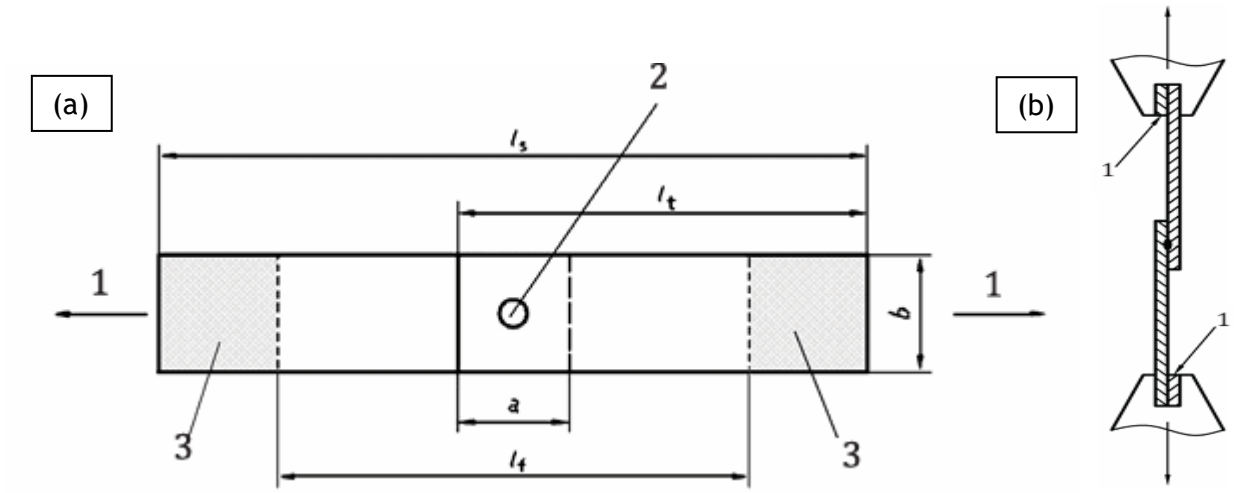


Figure 12: Schematic representation of the tensile shear test specimen according to EN ISO 14273:2016. (a) Top view detailing the geometrical parameters of the lap joint. (b) Cross-sectional view of the testing setup, illustrating the use of spacer plates [100].

The first set of the tensile shear test were performed using a SHIMADZU Autograph AG-Plus, with a maximum load capacity of 250kN and a grip speed of 10mm/min. Except for the final set of tensile shear test, which were performed using an INSTRON 8802, with a maximum load capacity of 250 kN, this machine was also used for the fatigue tests.

3.3.3.2 Macrostructure and Microstructure Analysis

An electric saw cut as shown in Figure 11, and an abrasive disc was used for removing transverse-section specimens for macro and micro analysis. Following ISO 17639[101], an etched macro examination was conducted to evaluate defects and joint structure, and micro etching was used to analyse the microstructure.

The metallographic preparation of the specimens started with mechanical grinding using SiC abrasive papers (180, 320, 400, 600, and 1000 mesh) at a rotational speed of 300 rpm. This was followed by a final polishing stage employing cloth pads and diamond suspensions (6 µm and 1 µm) at 150 rpm. To reveal the microstructure of the stainless steel, an electrolytic etching process using a 10% oxalic acid solution (10 g oxalic acid in 100 mL H2O) was adopted, applying a current density of 1 A/cm² at 6 V for 1 minute [102]. Conversely, the S355J2 carbon steel was etched using a 4% Nital solution (100 mL of 96% ethanol and 4 mL of 65% HNO3) for 10 seconds [102]. Due to the dissimilar nature of the welded joints, a selective etching approach was required: the S355J2 base metal was etched with Nital, while the remaining regions were subjected to the electrolytic oxalic acid procedure.

The microstructural characterisation was conducted using a Leica DM4000M optical microscope equipped with a DMC 2900 camera and Leica LAS X software. Additionally, macroscopic imaging of the entire specimen cross-section was acquired using a Leica DVM6 Digital Optical Microscope paired with the corresponding Leica LAS software.

3.3.3.3 Microhardness tests

For all welded joints, Vickers hardness tests were performed using a load of HV 0.1 according to ISO 9015-2. As seen in Figure 13, two rows were done, one aligned with the top weld bead, another below the fusion pool, using a regular interval along the row. The equipment used was the FALCON 400 micro/macro-Vickers Hardness Tester (INNOVATEST) with an applied load of 100gf for 10 seconds.

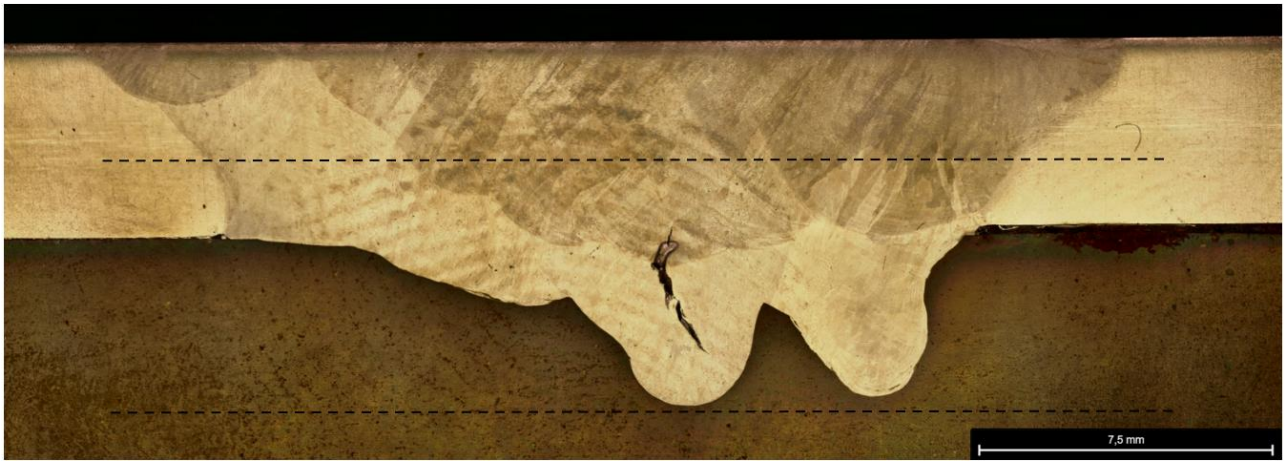


Figure 13:Rows of indentation in welded joints.

3.3.4 Corrosion Tests

The corrosion tests were conducted in a salt spray chamber according to the EN ISO 9227:2022+A1:2024 standard for a duration of 96 hours. The operational parameters were controlled and maintained as detailed in Table 13.

Table 13: Testing Conditions

NaCl Concentration	50+-5 g/L
Collected solution pH	6,5 to 6,7
Test solution pH	6,4 to 6,6
Concentration of the collected solution	1029 to 1032 g/dm3
Salt spray intensity	1,0 to 1,3 ml/h
Total volume collected during the test	442 ml in 4 collecting devices
Chamber temperature	35+-2 ºC
Air pressure	1,0 bar
Humidness temperature	35ºC
Corrosivity of the test chamber	73,2 g/m2

All specimens were exposed to identical salt-spray testing conditions, as shown in Figure 14. It should be noted that the dark marks observed on some specimens are the result of thermal oxidation induced by the welding process and were present on the specimens prior to the onset of testing.

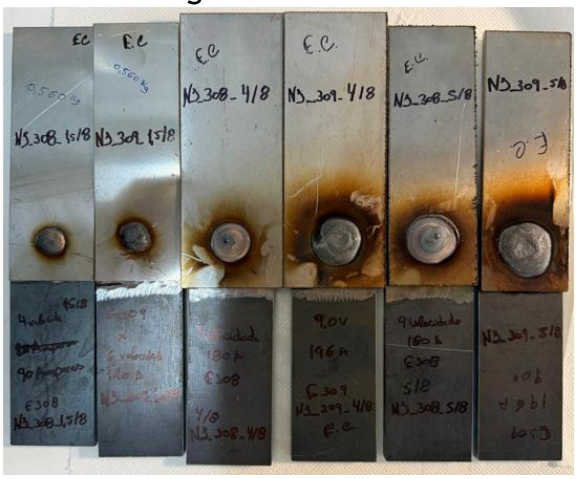


Figure 14: Initial state of the specimens before salt spray testing. The specimens are organised by material combination (alternating between FM).

3.3.5 Mechanical Test of Welded Specimens

3.3.5.1 Fatigue tests

Having characterised and selected the best additive material, it was imperative to evaluate how these combinations affect fatigue life. These fatigue tests will contribute to enrich the literature, which is very limited. Regarding the fatigue tests performed, twelve specimens were produced for each condition, as well as an additional three specimens to be used in the tensile shear tests.

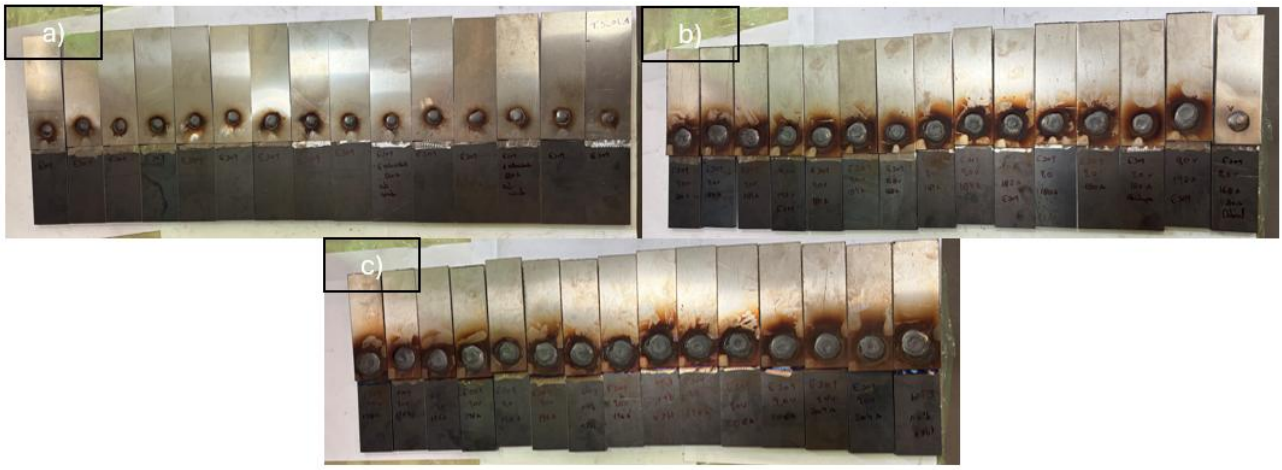


Figure 15: Specimens for static and fatigue testing; a) Sample 8 - TS_01_309; b) Sample 10 - TS_02_309; c) Sample 12 - TS_03_309.

The specimens were manufactured in accordance with the standard ISO 14324 [100], respecting the geometry and dimensions. The final dimensions and geometry of the specimens are shown in Figure 16.

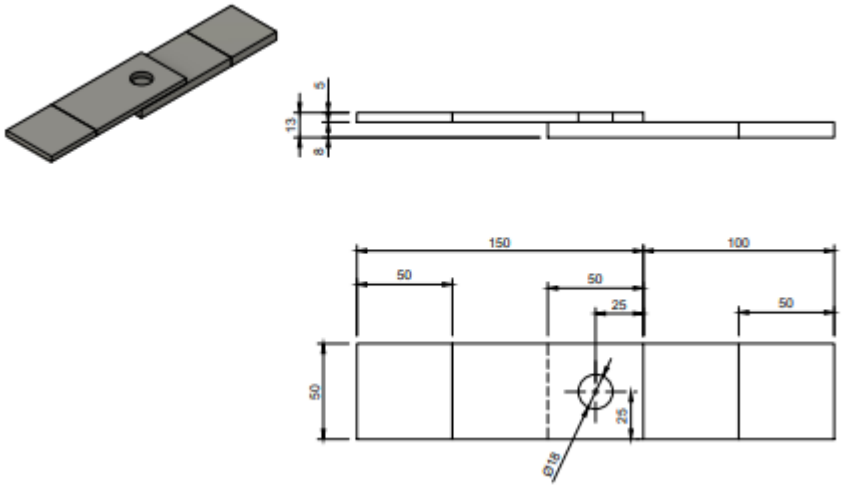


Figure 16: Geometry and Dimensions of the Specimens produced for Fatigue tests (mm).

Mechanical testing was carried out on an Instron 8802 servo-hydraulic testing machine that has a 250 kN load capacity. The fatigue tests were load-controlled at a stress ratio of R=0.05, using a sinusoidal loading waveform with a frequency of 15 Hz, in accordance with ISO 14324[100]. Several stress levels were defined to characterise the welded stacks over different numbers of cycles, aiming at the construction of a fatigue curve (S-N curve). For these fatigue tests, an infinite specimen life was defined in the

procedure as 5.00×10^6 cycles. Specimens that reached this number of cycles correspond to run-outs.

3.3.5.2 Tensile shear tests

As previously mentioned, the geometry and dimensions of the tensile shear specimens are equivalent to those of the fatigue tests. For each condition, three tests were conducted, following the ISO 4136 standard [103], and each resulted in a value of ultimate tensile shear force (kN), which translates into the ultimate load-bearing capacity of the welded joint, and the average of those values will be considered for each stack. The equipment used was also the same as the fatigue testing one, represented in Figure 17, and the defined displacement rate was 1mm/min.



Figure 17: Instron 8802 servo-hydraulic testing machine.

4.Results and Discussion

This chapter is structured into three main sections. Initially, the properties of the base materials are outlined, followed by the macro-analysis and tensile shear test results derived from the preliminary tests. The subsequent section examines the outcomes obtained using the finalised welding parameters, thereby facilitating the selection of the appropriate filler material. The chapter concludes with the evaluation of the fatigue life of the final plug-weld configurations.

4.1 Base Materials

This section presents the microstructure and hardness of the base materials, which will subsequently assist in identifying the boundaries of the HAZ. Figure 18 illustrates the microstructure of AISI 301LN with different thicknesses.

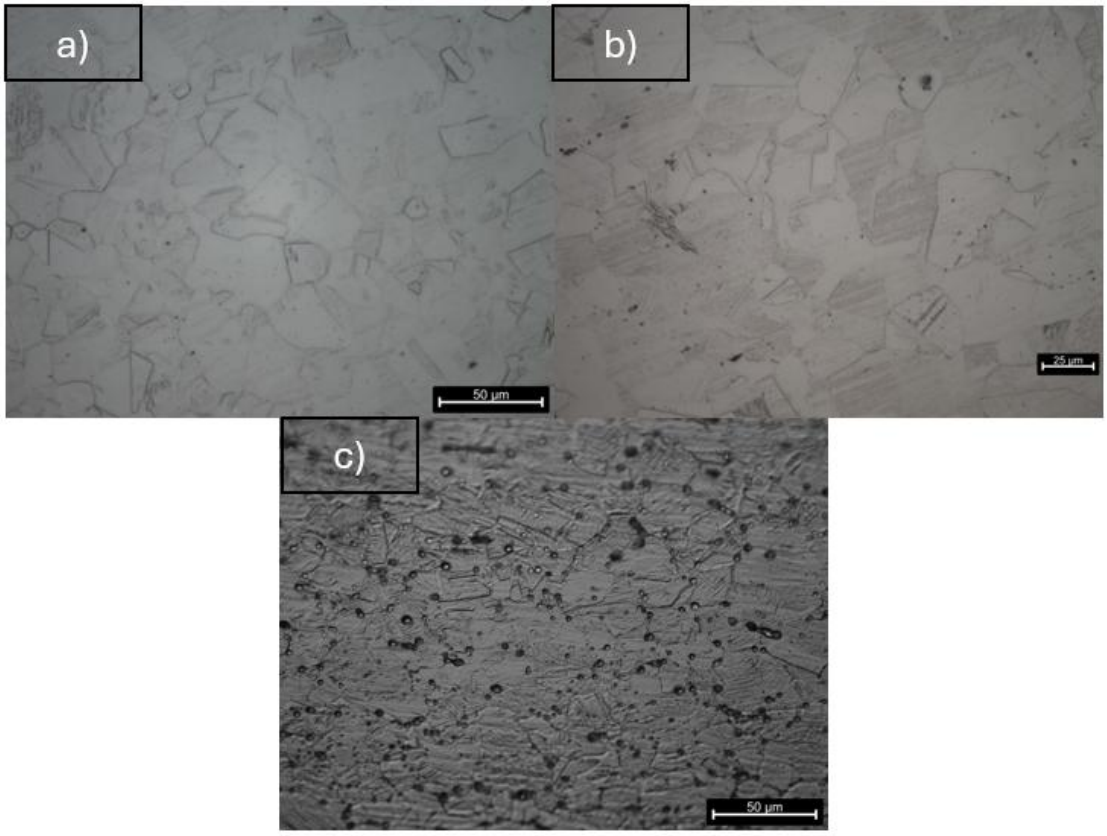


Figure 18: Images from optical microscopy of the AISI 301LN sheet with different thickness and temper conditions: (a) C850, 1.5 mm; (b) C850, 4 mm; and (c) C1000, 5 mm.

The AISI 301LN steel with thicknesses of 1.5 mm and 4 mm (Figure 18(a) and (b)) shows a microstructure characterised by well-defined polygonal grains and the presence of twins. In contrast, the C1000 condition with a 5 mm thickness (Figure 18(c)) exhibits a microstructure produced by cold rolling followed by recrystallisation, in which equiaxed grains formed during recrystallisation, although the previously deformed structure was not fully reverted. The previous work-hardening state introduces a high density of deformation bands and facilitates the transformation of metastable austenite into strain-induced martensite, as evidenced by the textured appearance of the grain structure.

The other material studied in this work, S355J2, is a structural steel with a simpler chemical composition. Figure 19 illustrates the microstructure.

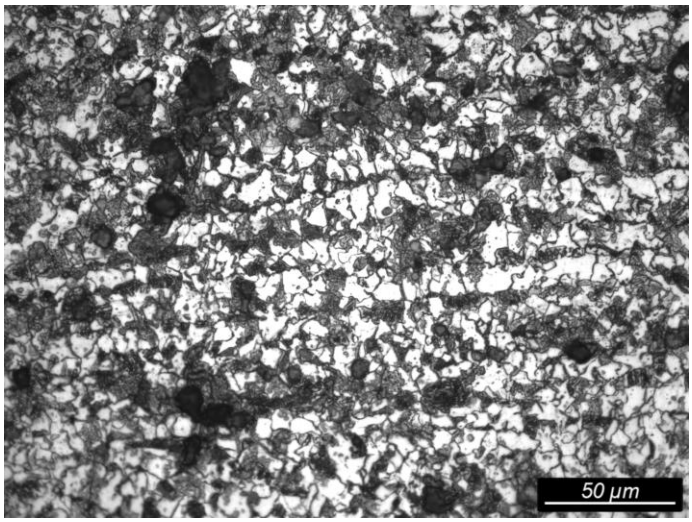


Figure 19:Image from optical microscopy of the S355 J2 sheet with 8mm of thickness.

We can see polygonal ferrite grains (this phase is characterised by high ductility) and colonies of perlite with high hardness and mechanical resistance. The hardness of the base materials is presented in Table 14.

Table 14: Hardness results of base materials

Indentation	S355J2	AISI 301 C850 1,5	AISI 301 C850 4	AISI 301 C1000 5
1	278	318	258	290
2	253	326	289	310
3	211	307	302	309
4	289	334	259	296
5	376	317	257	298
6	281	326	255	326
7	295	328	280	298
8	280	297	281	279
9	235	313	305	277
10	273	319	282	305
Average	277	319	277	299
Relative Standard Deviation (RSD)	16%	3%	7%	5%

The S355J2 exhibits an average hardness of 277 HV, with individual measurements varying widely, from a minimum of 211 HV to a maximum of 376 HV. This variation is justified by the banded ferrite-pearlite structure of the steel.

The hardness of all three conditions of AISI 301LN displays much lower RSD values, confirming a highly homogeneous microstructure. However, an anomaly is observed when comparing the two plates of the C850 temper grade. The thinner 1.5 mm plate exhibits a noticeably higher average hardness (319 HV) than the 4 mm plate (277 HV), despite sharing the same nominal designation. This behaviour may be associated with differences in the cold-rolling reduction ratio and the resulting degree of recrystallisation, with the thinner plate potentially retaining a greater fraction of work-hardened, unrecrystallised structure. However, in the absence of tensile test data for these specific thicknesses, this hypothesis could not be further validated and should be confirmed in future work.

A discrepancy is also observed when comparing the 1.5 mm plate (C850) with the

5 mm plate (C1000), which can again be attributed to the dynamics of the strain hardening and recrystallisation and the resulting hardness.

4.2 Preliminary results

4.2.1 Macrographic examination of the plug wels

Following the metallographic preparation, an evaluation of the cross-section of the plug welds, presented in Figure 20, was conducted to assess the structural integrity and the fusion zone characteristics.

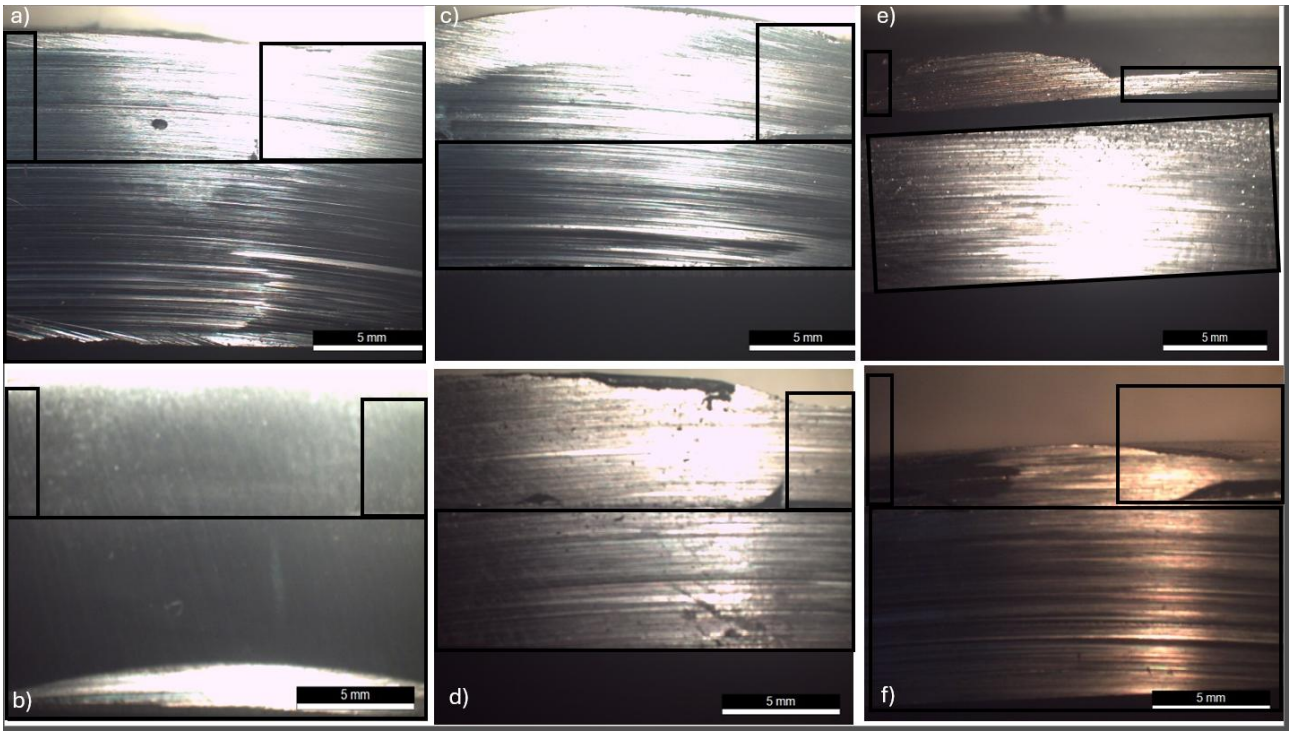


Figure 20: Stereo microscope images of the cross-section of the weld joints: a) Sample 1; b) Sample 2; c) Sample 3; d) Sample 4; e) Sample 5; f) Sample 6.

The analysis of the dissimilar joint cross-sections, presented in Figure 20, enables the identification of discontinuities in all samples. It is known that both geometric integrity and the quality of the metallurgical bond are strongly influenced by welding operating conditions. In the specimens corresponding to the largest plug diameter (18 mm), Figures 20-a and 20-b, a lack of fusion was observed at the lateral boundaries of the joint. Additionally, Figure 20-a exhibited a macro porosity within the central region of the fusion zone, which constitutes a critical operational defect.

With the hole diameter reduced to 15 mm, geometric asymmetries became apparent. In Figure 20-d, a clear lack of filling was identified on the left-hand quadrant of the weld bead, which is concurrently accompanied by a localized lack of fusion at the weld root corners. Nevertheless, despite these localised discontinuities, Figure 20-c exhibits a sound bond between the base materials.

Finally, the analysis of the joints with the smallest nominal diameter (3 mm), Figures 20-e and 20-f, revealed a pronounced gap between the overlapping plates. This gap is heavily influenced by the processing history and initial topology of the 0.8 mm thick AISI 301LN. This sheet was originally corrugated and subsequently subjected to a flattening process before welding. This mechanical flattening process is shown to be ineffective. Consequently, severe residual distortions remained in the thin-gauge plate,

inherently introducing geometric defects and preventing a flush, proper contact with the flat surface of the S355J2. Notably, during metallographic polishing, the AISI 301LN plate of Sample 5 detached from the S355J2 substrate, indicating poor interfacial bonding.

4.2.2 Tensile shear test

Following the macrostructural characterisation of the plug-welded joints, their mechanical performance was evaluated using lap-shear tensile tests to establish a direct correlation between the previously identified morphological and geometric discontinuities and the actual load-bearing capacity of the joints.

Table 15: Statistical summary of the tensile shear test for samples 1 to 6, displaying the minimum, maximum, and average failure load (N), and the Relative Standard Deviation (RSD).

FAILURE LOAD (N)	MINIMUM	MAXIMUM	AVERAGE	RSD
SAMPLE 1 – 301(0.8)355(8)308(LSI)_PLUG 3	5808	9007	7152	19%
SAMPLE 2 – 301(0.8)355(8)309(LMO)_PLUG 3	6332	10323	8531	19%
SAMPLE 3 - 301(4)355(6)308(LSI)_PLUG 15	50592	66456	58846	11%
SAMPLE 4 – 301(4)355(6)309(LMO)_PLUG 15	16977	28977	24322	19%
SAMPLE 5 – 301(5)355(8)308(LSI)_PLUG 18	72624	95130	93145	2%
SAMPLE 6 – 301(5)355(8)309(LMO)_PLUG 18	89528	96113	88525	10%

The experimental data compiled in Table 15 reveal substantial variation in mechanical performance among the tested configurations. Regarding the failure mechanism, all specimens failed via shear along the weld interface. Regarding relevance, sample 5 achieved the highest average failure load. Conversely, the lowest average failure load was recorded for the configurations with the 3mm plug.

When evaluating specimens of identical dimensions to compare the effects of different filler metals, distinct results emerge depending on the plug diameter. For the 3 mm plug configuration, high variation is observed in both conditions. Regarding the 15mm plug geometry, the results display a notable difference, while Sample 3 showed an average load of 58846 N, Sample 4 exhibited a high dispersion of 19%, along with a low average load of 24322 N.

Following the analysis of the quantitative mechanical data, a macrographic examination of the fracture surface was conducted for each tested sample to understand the structural behaviour of the joints and to provide crucial insights into the geometric consistency of the failure and the interaction between the overlapping sheets.

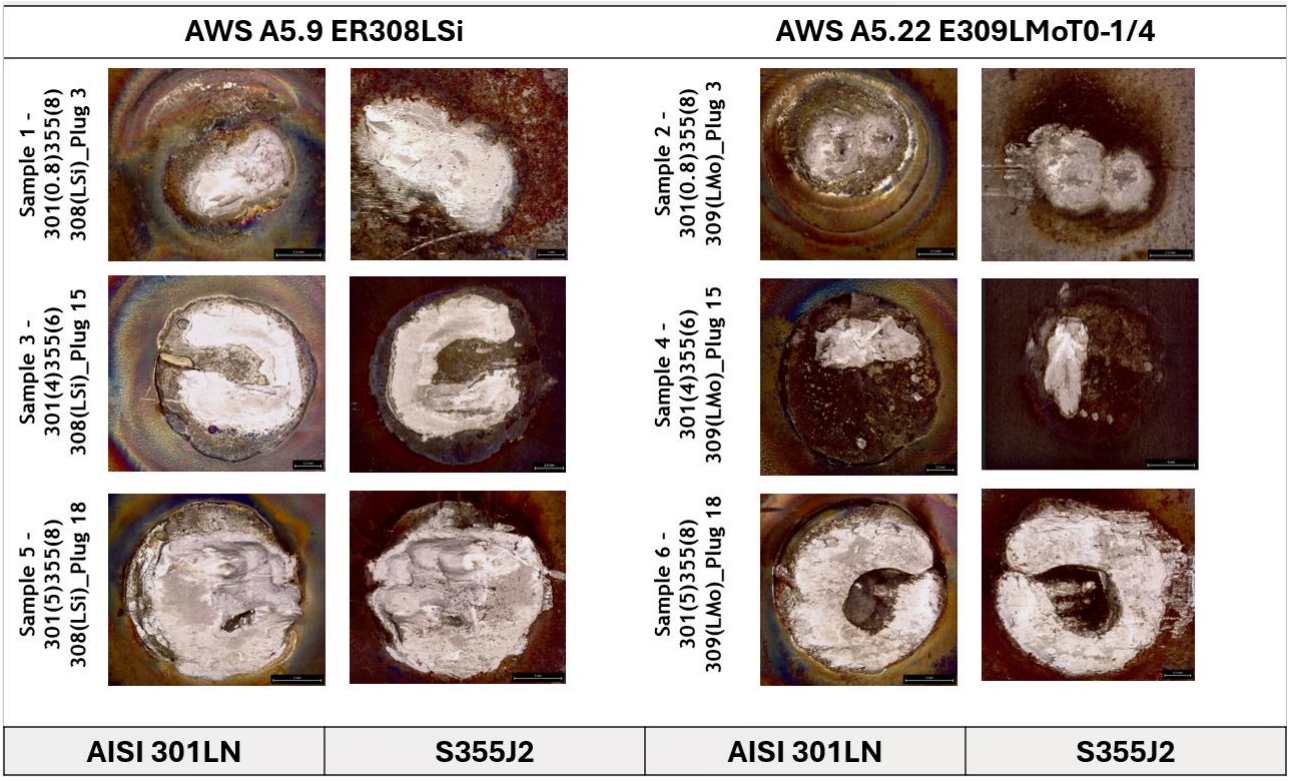


Figure 21:Surface macrographs of the fractured plug weld specimens separating the AISI 301LN and S355J2 interfaces. The matrix compares samples 1 to 6 across three plug diameters (3 mm, 15 mm, and 18 mm) welded with AWS A5.9 ER308LSi (left) and AWS A5.22 E309LMoT (right).

The features of the fractured surfaces justify the mechanical performance observed during the lap shear tests. In the case of the 3mm plug configurations, the low average shear load is governed by poor bonding between the filler material and the S355J2 steel substrate. The interface exhibited localised adhesion, which easily succumbed to shear stress forces. Furthermore, it is possible to observe a very wide HAZ surrounding these small joints; however, it's not possible to conclude about the bonding between the filler metal and the AISI 301LN.

Regarding the 15 mm plug configurations, there is clear evidence of fusion along the plug perimeter, whereas the centre of the plug exhibits no fusion bond. In the case of sample 3, the lack of fusion in the middle of the plug hole is highly apparent. A similar phenomenon occurred in sample 4. It can be concluded that the welding parameters were inadequate for achieving adequate fusion of S355J2, resulting in a low failure load. Conversely, sample 5 produced the best results during the initial phase. As observed in Figure 22, the fracture surface demonstrates that a metallurgical bond was established between the filler metal and the S355J2 substrate. In contrast, sample 6 exhibits the same recurring pattern, characterised by localised welding at the borders whilst leaving the centre entirely unbonded.

Crucially, this analysis highlighted that significant improvements were required before these configurations could be utilised in real-world applications. The recurrence of incomplete fusion and lack of penetration across multiple specimens demonstrates that the welding parameters and joint geometries were not fully optimised to ensure a reliable metallurgical bond, regardless of the filler metal selected. In the case of the 3 mm plugs, the utilisation of such a small diameter introduced severe technical constraints, restricting arc accessibility and leading to poor penetration into the lower base material.

The operational aspects of the welding process were considered, given that process repeatability and reproducibility are paramount. Achieving consistent, identical welds is essential for quality assurance; however, an elevated variation severely compromises the ability to guarantee structural and geometric conformity across production lots.

4.2.3 Process improvement

Welding literature indicates that gaps between faying surfaces reduce effective thermal contact and weaken heat conduction across the interface, thereby compromising local fusion efficiency and stability[104]. Therefore, the 0.8 mm thick AISI 301LN sheet was rejected and replaced with flat 1.5 mm thick sheet to ensure the required gap-free contact with the structural steel sheet substrate. Furthermore, it was concluded that the small 3 mm diameter restricted welder accessibility. By increasing the sheet thickness, compliance with normative standards was maintained whilst allowing the plug diameter to be expanded to 10 mm. This geometric modification improved arc accessibility, ensuring easier torch manipulation and enhancing process repeatability. This aligns with relevant AWS requirements regarding minimum dimensions, which are designed to ensure operational accessibility, weldability, and strict compliance with applicable code provisions.[55] Concurrently, the welding parameters were increased to provide sufficient heat input to melt the S355J2 substrate under the arc, thereby ensuring a sound metallurgical bond and stable fusion development at the joint interface.

Regarding the 15 mm plug configuration, the primary modification involved standardising the process by utilising the 8 mm thick S355J2 carbon steel plate as the base substrate to ensure uniform thermal dissipation, alongside subsequent optimisation of the welding parameters.

Finally, for the 18 mm plug geometry, parameter adjustments were also implemented. Additionally, for both the 15 mm and 18 mm configurations, the feasibility of introducing a countersink (chamfer) was evaluated. This geometric modification aimed to increase the torch angle of attack, thereby improving operator accessibility and effectively mitigating boundary fusion defects previously identified (Figure 22). Metallurgically, the introduction of such a chamfer enlarges the access angle to the joint, promotes deeper arc penetration, and facilitates the fusion of both the side walls and the root. [55,105,106]



Figure 22: Comparation of the 18 mm plug welds deposited with E309LMo filler metal: (a) geometry without countersink; (b) geometry with countersink.

The macrographs presented in Figure 22 indicate that lack of fusion at the corners persisted in the original geometry (Figure 22a), whereas Figure 22b shows complete corner fusion and a markedly improved metallurgical bond with the AISI 301LN sheet. This is consistent with the beneficial effect of the countersink in enhancing torch accessibility, increasing arc penetration, and promoting more complete fusion of the side walls and root. Overall, the chamfered configuration appears to produce more favourable joint integrity, which is in agreement with the consulted literature[105–107].

4.3 Characterisation of final specimens

This characterisation encompasses macroscopic and microstructural assessments to evaluate soundness and phase transformations, microhardness profiling to map mechanical gradients, and corrosion testing to ensure performance in environments. The findings detailed in the following subsections made it possible to determine the best-performing filler metal and to compare the plug geometries tested.

4.3.1 Microstructural characterization

Figure 23 presents the macrostructure of the welded joint between 1.5 mm-thick AISI 301LN stainless steel and 8 mm-thick S355J2 carbon steel, with ER308LSi filler metal.

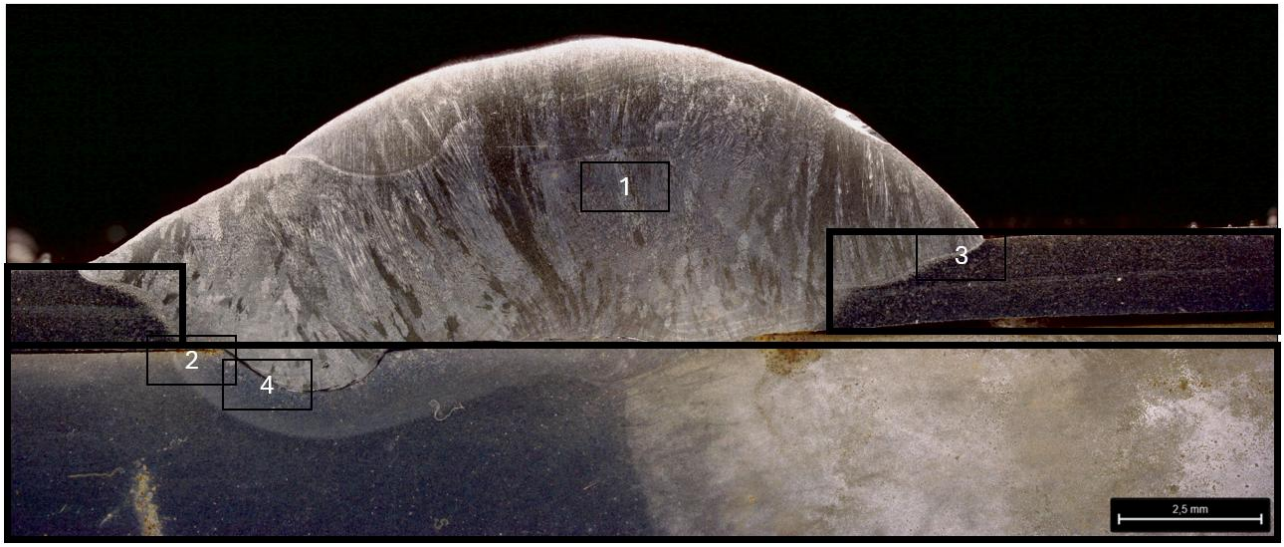


Figure 23: Macrostructure of welded joint between 1.5 mm AISI 301LN and 8 mm S355J2 with the filler metal AWS A5.9 ER308LSi. Position 1- FM, Position 2- Triple Interface between the 2 BM and the FM, Position 3- Interface between the FM and the AISI 301LN and Position 4- Interface between the FM and S355J2.

The cross-section of the plug weld shows four distinct zones that were identified by microstructural analysis; the corresponding results are presented in Figure 24.

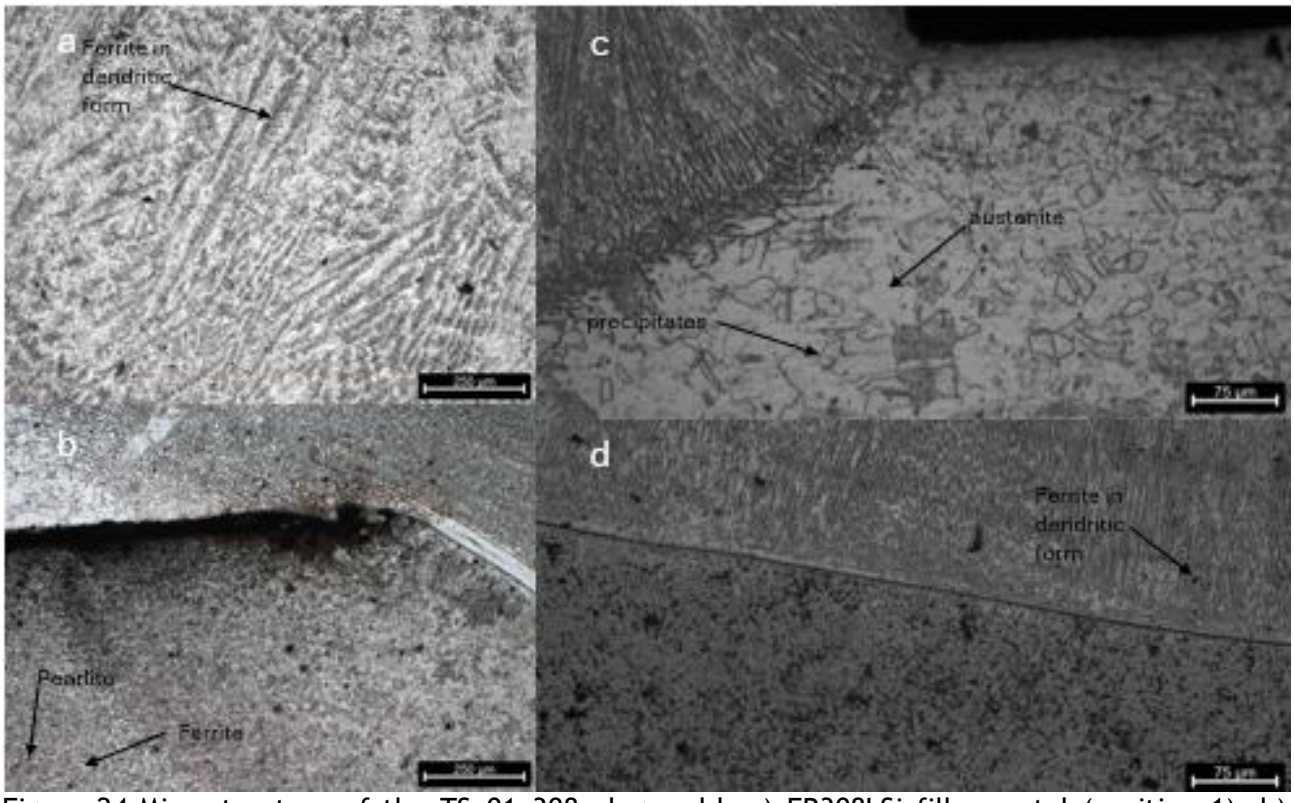


Figure 24:Microstructure of the TS_01_308 plug weld: a) ER308LSi filler metal (position 1); b) interface between the filler metal and AISI 301LN (position 2); c) interface between the filler metal, AISI 301LN and S355J2 (position 3); d) interface between the filler metal and S355J2 (position 4).

In position 1, the ER308LSi filler metal shows delta ferrite with a fine dendritic morphology embedded in an austenitic matrix. Position 2 illustrates the metallurgical transition between the filler metal and the adjoining base materials. A more gradual transition is observed at the AISI 301LN interface, whereas a sharper boundary remains visible between the filler metal and the S355J2 steel, associated with the more abrupt change in chemical composition between the two materials. Within the HAZ of the AISI 301LN, the austenitic matrix shows evidence of precipitates, while the region corresponding to the S355J2 base material retains a ferritic-pearlitic matrix.

Figure 25 shows the macrostructure of the dissimilar welded joint with the same material combination as the previous specimen but fabricated using E309LMoT0-1/4 filler metal. The cross-section identifies four distinct zones. A clear misalignment between the two base metals is evident, caused by the welding process.

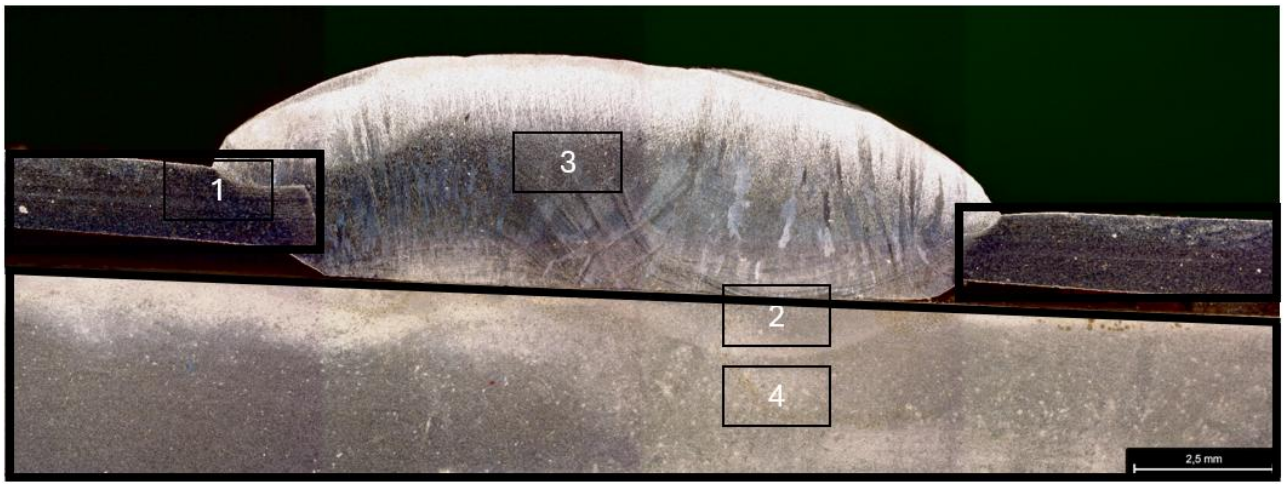


Figure 25: Macrostructure of welded joint between 1.5 mm AISI 301LN and 8 mm S355J2 with the filler metal AWS A5.22 E309LMoT0-1/4. Position 1 – Interface between the AISI 301LN and the FM; Position 2 – Interface between the S355J2 and the FM; Position 3 – FM; Position 4 - S355J2.

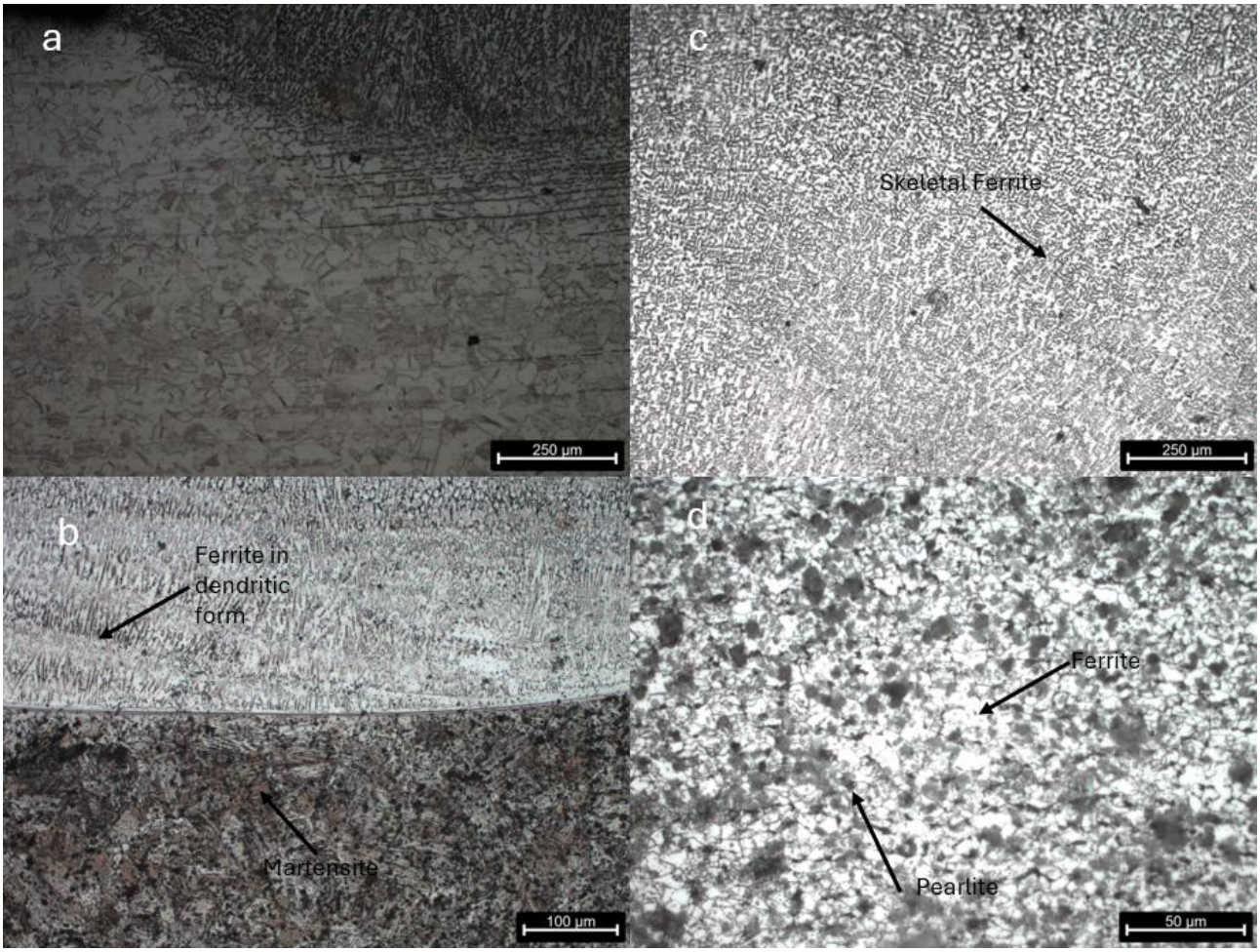


Figure 26: Microstructure of the TS_01_309 plug weld: a) Interface between the filler metal and AISI 301LN; b) Interface between the filler metal and S355J2 position 2); c) ER309LMo (position 3); S355J2 (position 4).

Figure 26 provides a detailed microstructural analysis across four distinct zones of the welded joint. Position 1 reveals a region characterised by equiaxial grains of austenite, and the formation of a skeletal morphology into the BM region demonstrates an excellent metallurgical bonding. Position 2 shows the boundary between the filler metal that

exhibits both dendritic and skeletal ferrite, whereas the adjacent HAZ of S355J2 shows localised martensite along with numerous precipitates. Furthermore, position 3 displays a highly homogeneous microstructure composed of delta ferrite. Lastly, position 4 shows the unaffected S355J2 base material, characterized by a typical ferritic matrix with pearlitic colonies, highlighting a significant increase in grain size when compared with the refined grain structure observed near the interface in position 2.

Figure 27 presents the macrostructure of the dissimilar welded joint between 4 mm-thick AISI 301LN stainless steel and 8 mm-thick S355J2 carbon steel, fabricated with ER308LSi filler metal.

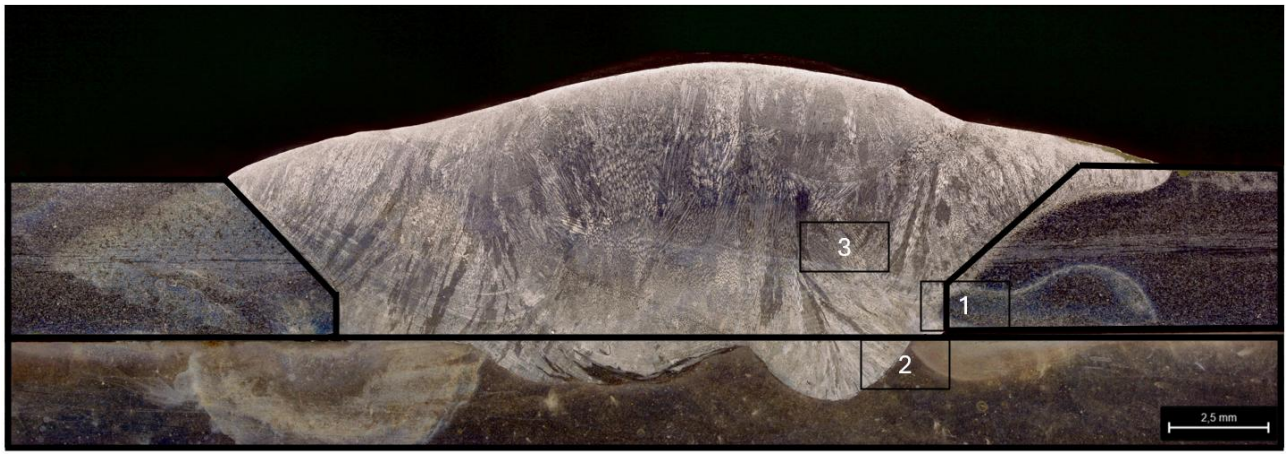


Figure 27:Macrostructure of welded joint between 4 mm AISI 301LN and 8 mm S355J2 with the filler metal AWS A5.9 ER308LSi.Position 1 – Interface between the AISI 301LN and the FM; Position 2 – Interface between the S355J2 and the FM; Position 3 – FM.

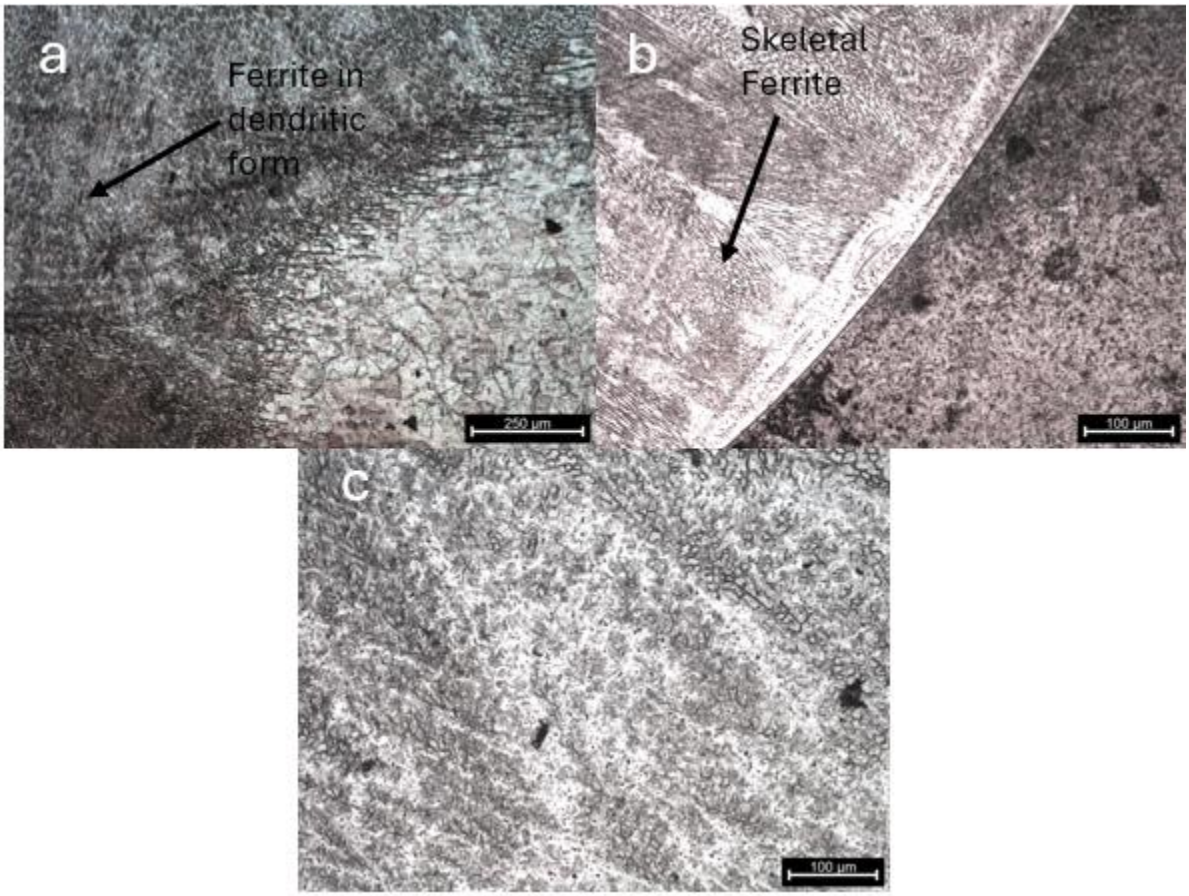


Figure 28:Microstructure of the TS_02_308 plug weld: a) Interface between the filler metal and AISI 301LN; b) Interface between the filler metal and S355J2 position 2); c) ER308LSi (position 3).

The microstructural features observed are broadly similar to those described for the TS_01_308, with no major differences identified between the two joint configurations.

Figure 30 shows the macrostructure of the dissimilar welded joint with the same material combination as the previous specimen but fabricated using E309LMoT0-1/4 filler metal.



Figure 29: Macrostructure of welded joint between 4 mm AISI 301LN and 8 mm S355J2 with the filler metal AWS A5.22 E309LMoT0-1/4.Position 1 – Interface between the AISI 301LN and the FM; Position 2 – FM; Position 3 – Interface between the S355J2 and the FM.

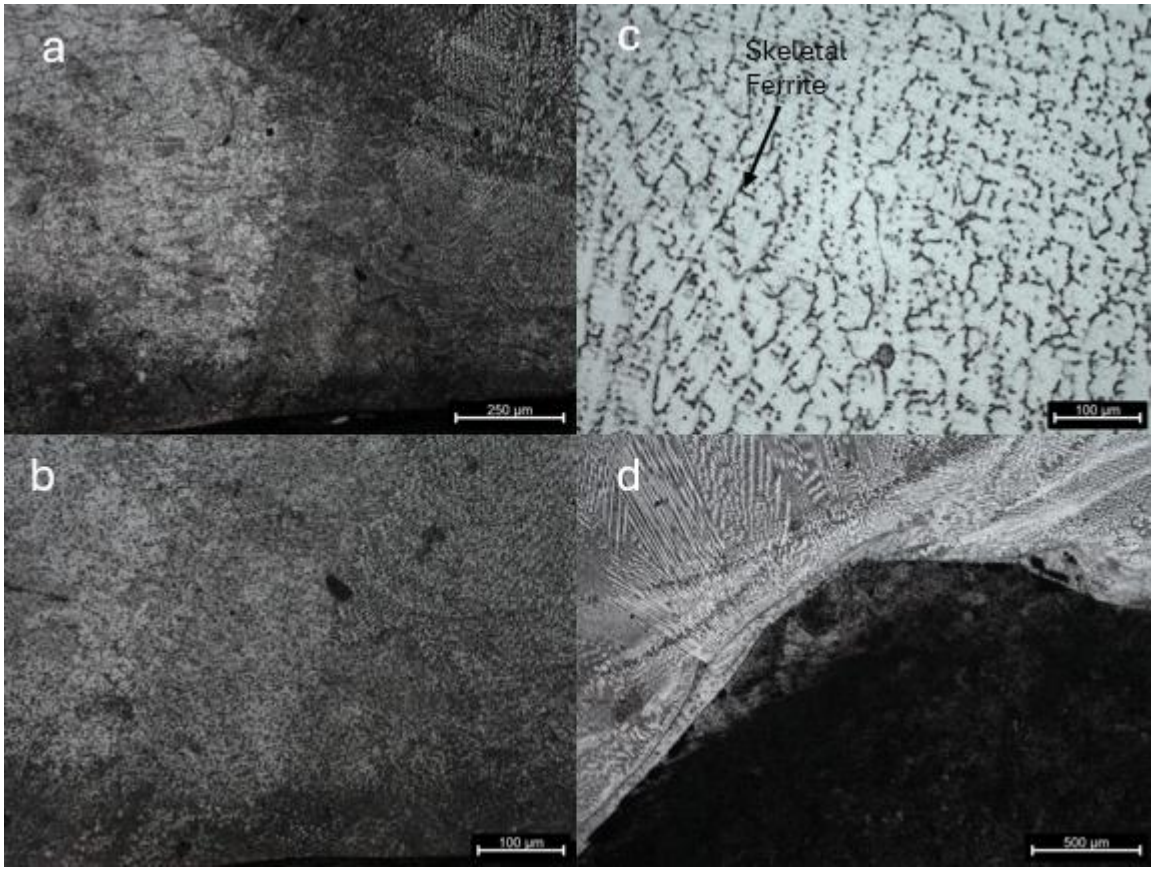


Figure 30:Microstructure of the TS_02_309 plug weld: a) Interface between the filler metal and AISI 301LN (position 1); b) position 1; c) ER309LMo (position 2). d) Interface between the filler metal and S355J2 (position 3).

In position 1, three distinct regions can be identified: the region on the far left, corresponding to the BM, and two separate regions corresponding to the FM. These two FM regions represent the initial and final welding passes, respectively. Due to the intense

thermal cycling and high heat input experienced during the process, a high density of precipitates is observed at this interface, which may be related to the higher alloy element content in the chemical composition of AWS A5.22 E309LMoT0-1/4. In position 2, in the core of the FM, the microstructure consists of a characteristic austenitic matrix embedded with skeletal ferrite. When compared to TS_02_308, it is not clear how the delta ferrite is presented. Furthermore, at position 3, a distinct interface is observable between FM and S355J2, and the FM reveals a dense distribution of both dendritic and skeletal ferrite exhibiting varying crystallographic orientations.

Figure 31 presents the macrostructure of the dissimilar welded joint between 5 mm-thick AISI 301LN stainless steel and 8 mm-thick S355J2 carbon steel, fabricated with ER308LSi filler metal.



Figure 31:Macrostructure of welded joint between 5 mm AISI 301LN and 8 mm S355J2 with the filler metal AWS A5.9 ER308LSi. Position 1 – Interface between the AISI 301LN and the FM; Position 2 – FM; Position 3 – Interface between the S355J2 and the FM.

As observable from Figure 32, this specific configuration was also bevelled; the primary differences relative to the preceding combination lie in the plug hole diameter, the welding parameters, and the AISI 301LN thickness.

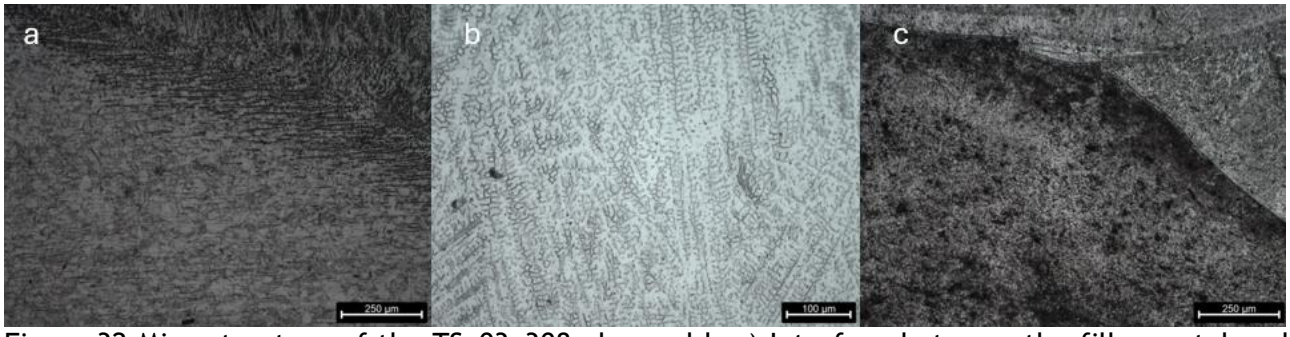


Figure 32:Microstructure of the TS_03_308 plug weld: a) Interface between the filler metal and AISI 301LN (position 1); b) ER308LSi (position 2); c) Interface between the filler metal and S355J2 position 3).

In position 1, the interface between the FM and the AISI 301 LN exhibits a microstructural mixing showing a skeletal ferrite on top of the austenite matrix; furthermore, there is a notable modification in the austenite grain morphology within the HAZ, which can be associated with a recrystallisation phenomenon induced by the thermal cycle of the welding process. In position 2, the FM shows a homogeneous microstructure.

This region is characterised by an austenitic matrix containing skeletal ferrite, which was not observed in the other combinations welded with ER308LSi Lastly, position 3 illustrates the interface between the FM and the S355J2, where the fusion line is clearly defined. A significant presence of precipitates is observed adjacent to this boundary; this carbide formation can be driven by carbon diffusion from the BM towards the weld metal due to the chemical gradient and the thermal cycle, ultimately promoting interfacial precipitation.

Figure 33 shows the macrostructure of the dissimilar welded joint with the same material combination as the previous specimen but fabricated using E309LMoT0-1/4 filler metal.



Figure 33:Macrostructure of welded joint between 5 mm AISI 301LN and 8 mm S355J2 with the filler metal AWS A5.22 E309LMoT0-1/4.Position 1 – Interface between the AISI 301LN and the FM; Position 2 – Interface between the S355J2 and the FM; Position 3 – FM.

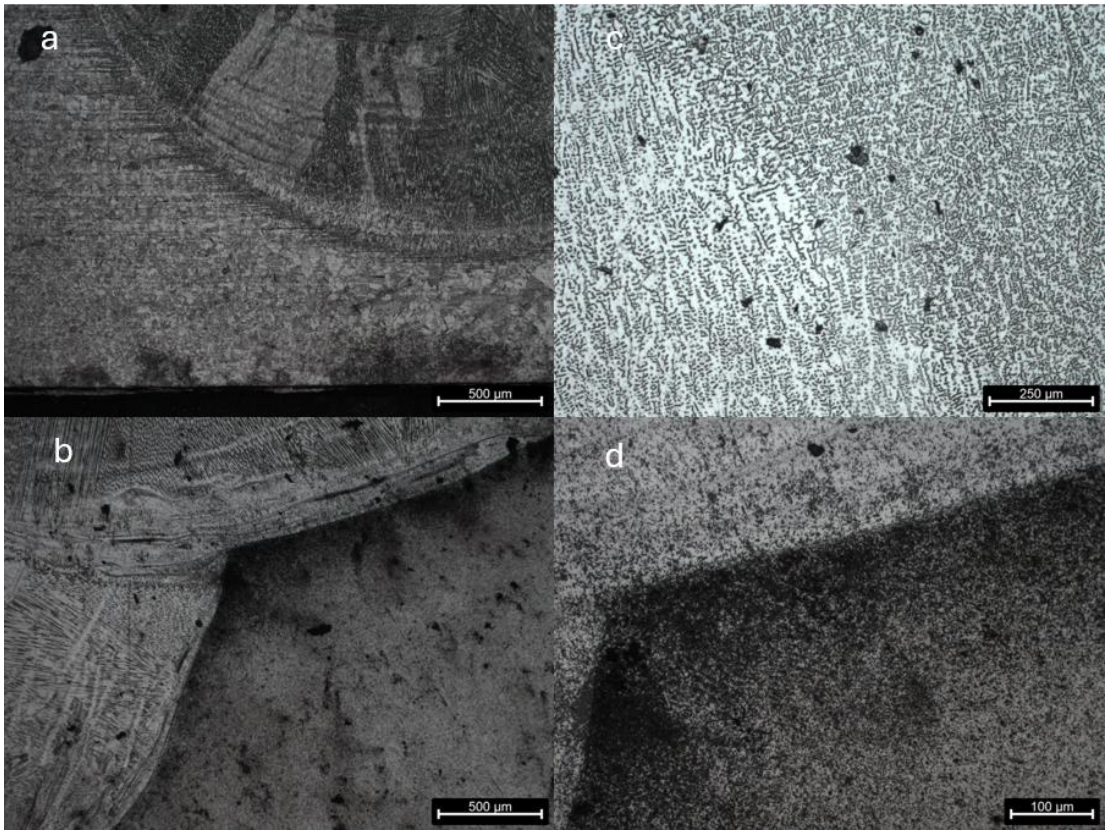


Figure 34:Microstructure of TS_03_309 plug weld: a) Interface between the filler metal and AISI 301LN (position 1); b) Interface between the filler metal and S355J2 (position 2); c) ER309LMo (position 3).

In position 1, the junction between the AISI 301 LN and the FM is observed, with the elongation of the skeletal ferrite from the FM to the matrix of austenite of the BM, as was observed in the other combinations. Furthermore, in the HAZ of the BM a significant coarsening of the austenite grains is noticeable immediately adjacent to the interface. This grain growth is attributed to the severe thermal cycle of the welding process, which exceeded the recrystallisation temperature in the near-boundary region, driving rapid grain growth at the boundary. In position 3, the FM exhibits a homogeneous microstructure comprising a matrix of austenite and skeletal ferrite, accompanied by precipitates or inclusions. Lastly, position 2 addresses the dissimilar interface between the FM and the S355J2 structural steel. While a distinct macroscopic boundary separates the two alloys, higher magnification reveals a dense, extensive distribution of carbide precipitates concentrated along this interfacial zone, induced by localised carbon migration.

In every combination, it was possible to identify the interfaces between the three different materials. At the interface between the AISI 301LN and the FM, bonding between the two materials can be observed, which may be related to their similar chemical composition. In contrast, in the case of S355J2 and the FM, a clear interface separates both materials. Both FMs show a microstructure of austenitic matrix with the presence of delta ferrite. For ER308LSi, the ferrite morphology could not be clearly identified in combinations 1 and 2, however, in the final combination, it was clearly displayed as skeletal ferrite. E309LMoT0-1/4, on the other hand, consistently shows an austenitic matrix with skeletal ferrite across every combination.

4.3.2 Microhardness Profiling

Analysis of the hardness profiles across the studied specimens indicates that they are influenced by both sheet thickness, welding parameters, and FM, which govern the thermal distribution developed during the welding cycle. Consequently, three microstructurally distinct regions are identified after welding: the two BM, the HAZ, and the FM. Because each zone experienced a unique thermal history in terms of intensity and duration, local variations in hardness are naturally expected. The distribution of microhardness values along the analysed profiles confirms this trend, demonstrating that the welding process results in a mechanically heterogeneous joint.

The hardness profiles across the weld joint interface are shown in Figure 35 to Figure 40. On the AISI 301LN side, the hardness ranges from 300 HV to 340 HV, decreasing toward the weld metal zone. This reduction is likely due to austenite recrystallisation, which decreases the martensite fraction and consequently lowers the hardness. Both FM present a hardness ranging from 180 HV to 210 HV. On the S355J2 side, the hardness is more homogeneous, ranging from 160 HV to 190 HV.

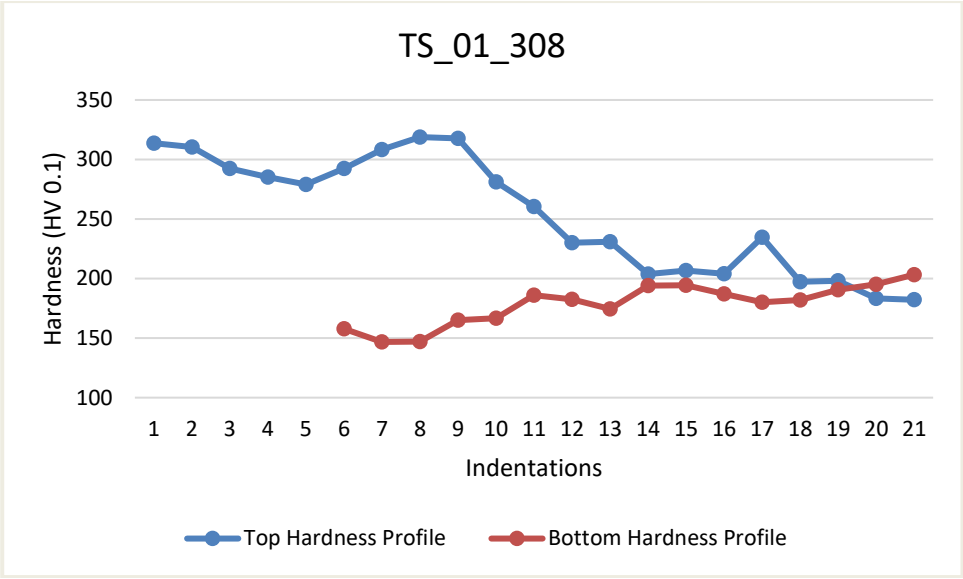


Figure 35: Microhardness profile of the welded joint between 1.5 mm AISI 301LN and 8 mm S355J2 with the filler metal AWS A5.9 ER308LSi.

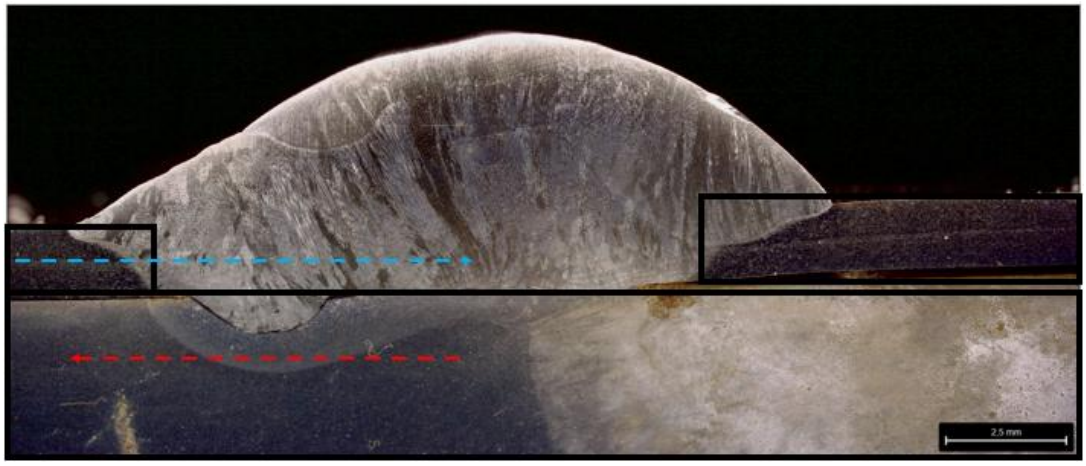


Figure 36: Macrostructure of welded joint between 1.5 mm AISI 301LN and 8 mm S355J2 with the filler metal AWS A5.9 ER308LSi.

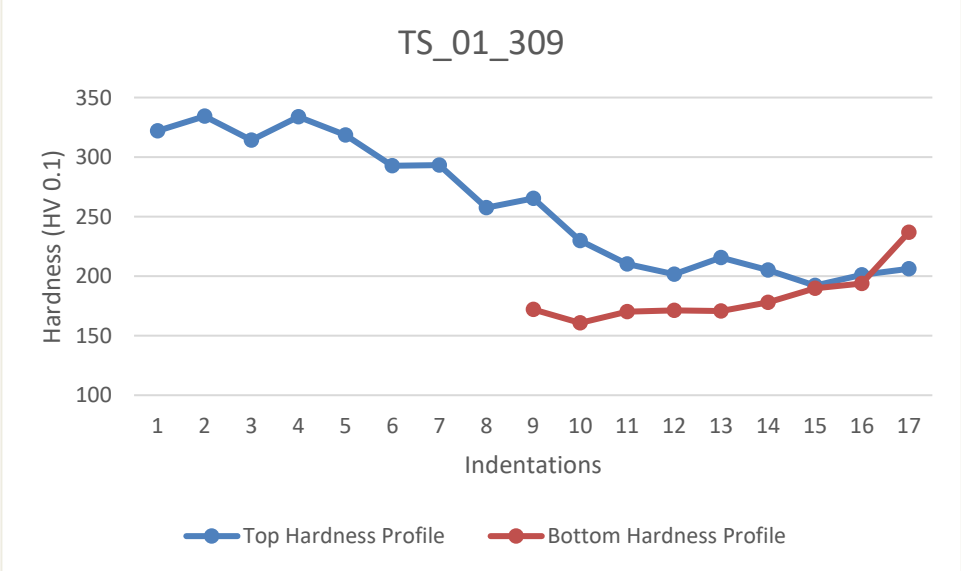


Figure 37: Microhardness profile of the welded joint between 1.5 mm AISI 301LN and 8 mm S355J2 with the filler metal AWS A5.22 E309LMoT0-1/4.

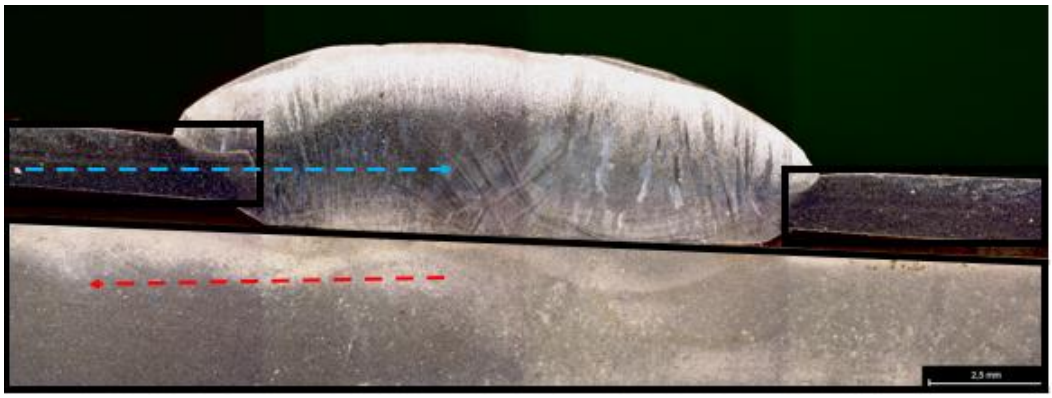


Figure 38:Macrostructure of welded joint between 1.5 mm AISI 301LN and 8 mm S355J2 with the filler metal AWS A5.22 E309LMoT0-1/4.

Figures 35 and 37 illustrate the hardness profiles across the joint between 1.5 mm AISI 301LN and 8 mm S355J2 using two different FMs. In the top hardness profile, the region spanning indentations 1-7 corresponds to the AISI 301LN BM. From indentation 12 onwards, the profile transitions into the FZ, where the hardness values stabilise at their lowest recorded levels.

The bottom hardness profile was measured entirely within the S355J2 steel. Fewer indentations were performed in this region once the hardness values stabilised, confirming that the profile had reached the unaffected BM zone. Moving further away from the FZ towards the BM, a clear, progressive decrease in hardness is observed before the values eventually stabilise.

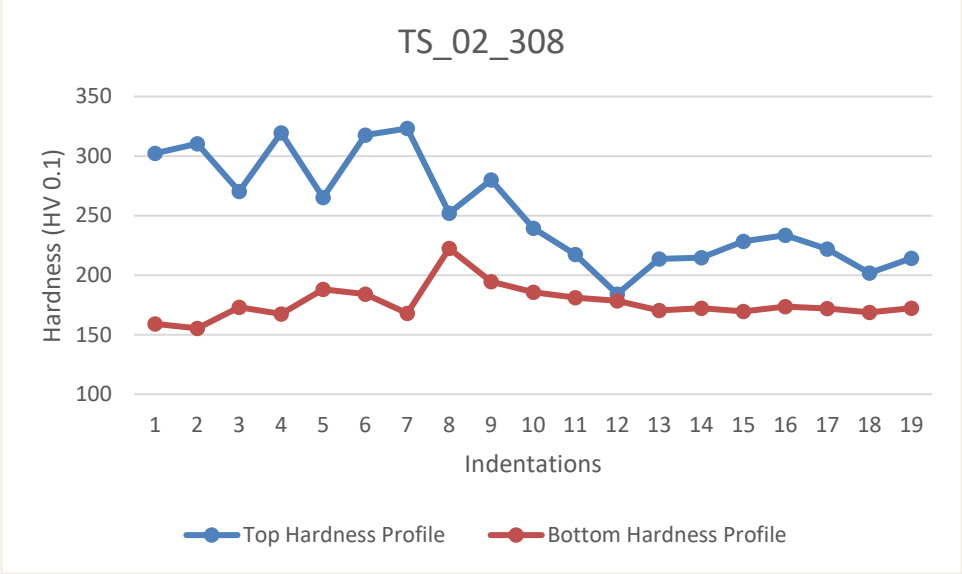


Figure 39: Microhardness profile of the welded joint between 4 mm AISI 301LN and 8 mm S355J2 with the filler metal AWS A5.9 ER308LSi.

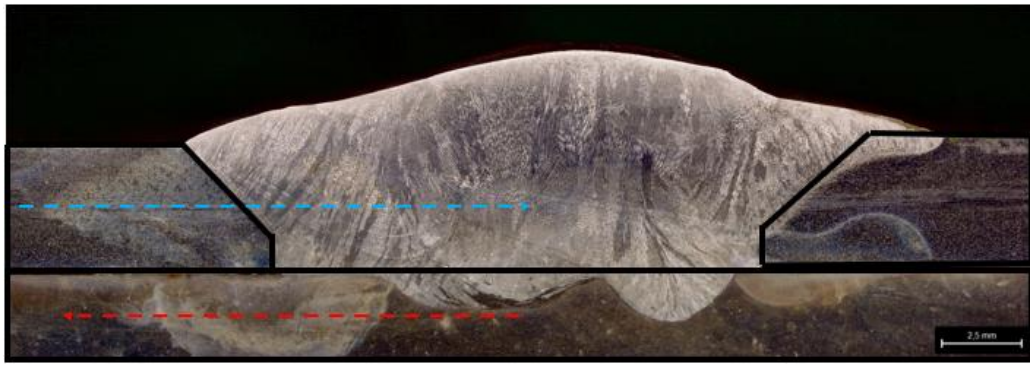


Figure 40:Macrostructure of welded joint between 4 mm AISI 301LN and 8 mm S355J2 with the filler metal AWS A5.9 ER308LSi.

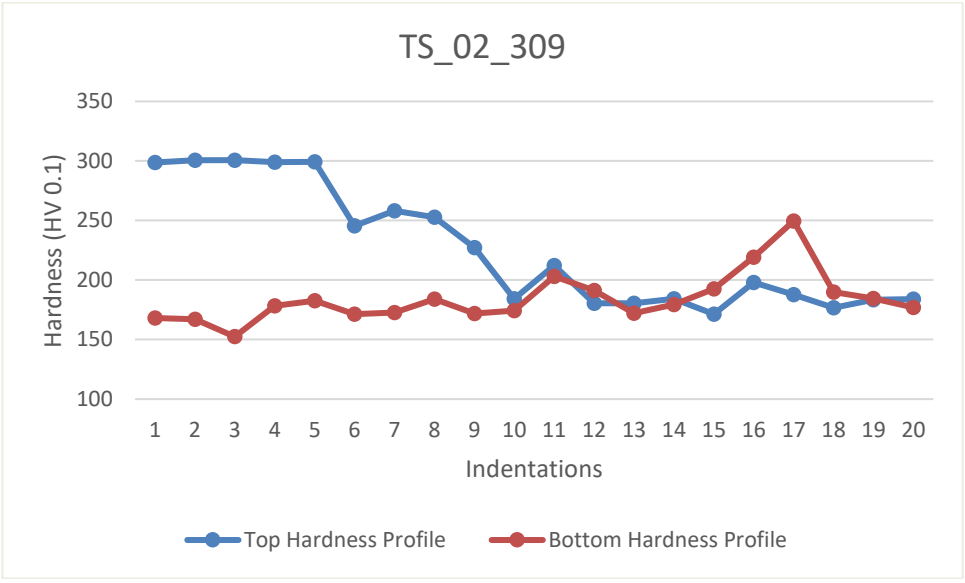


Figure 41: Microhardness profile of the welded joint between 4 mm AISI 301LN and 8 mm S355J2 with the filler metal AWS A5.22 E309LMoT0-1/4.

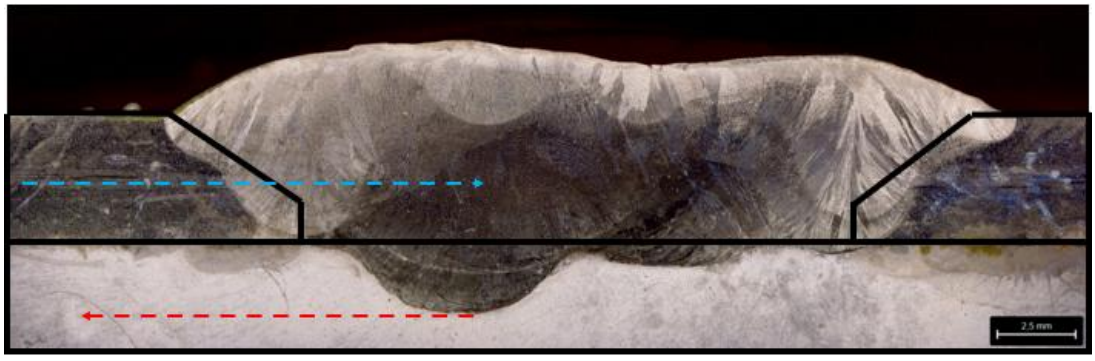


Figure 42:Macrostructure of welded joint between 4 mm AISI 301LN and 8 mm S355J2 with the filler metal AWS A5.22 E309LMoT0-1/4.

Figures 39 and 41 present a different joint combination; however, the overall profile tendency remains identical. A baseline hardness of approximately 300 HV is recorded within the AISI 301LN base metal, followed by a distinct decrease upon entering the HAZ, and a subsequent drop within the FM. In the bottom hardness profile, a similar trend is observed. Beyond these regions, hardness decreases progressively with increasing distance from the FZ.

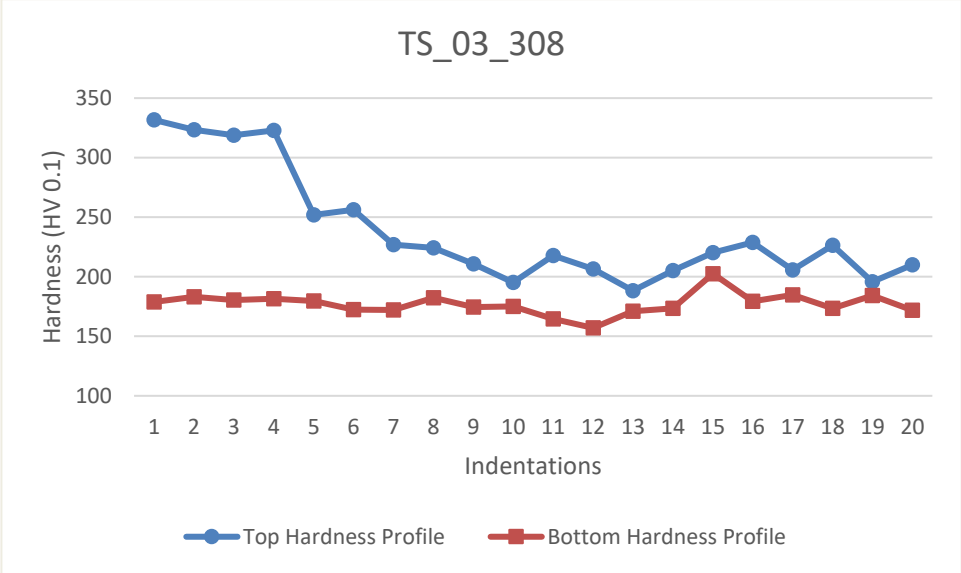


Figure 43: Microhardness profile of the welded joint between 5 mm AISI 301LN and 8 mm S355J2 with the filler metal AWS A5.9 ER308LSi.

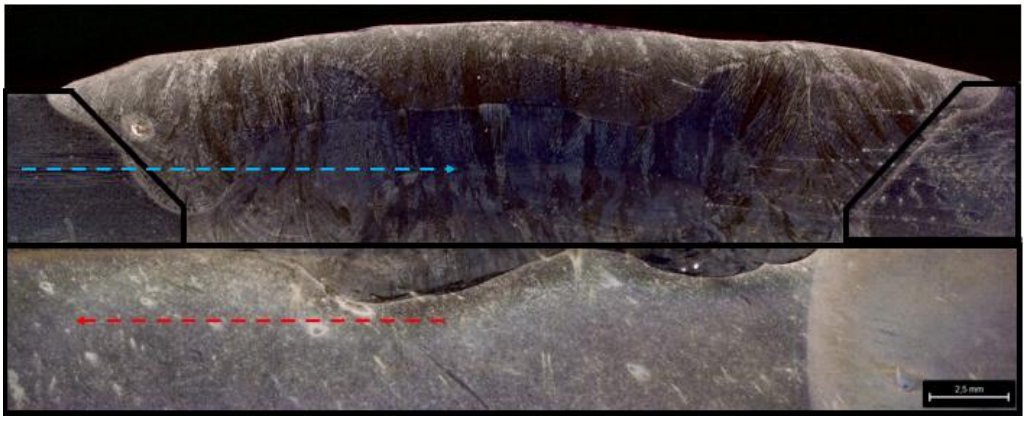


Figure 44:Macrostructure of welded joint between 5 mm AISI 301LN and 8 mm S355J2 with the filler metal AWS A5.9 ER308LSi.

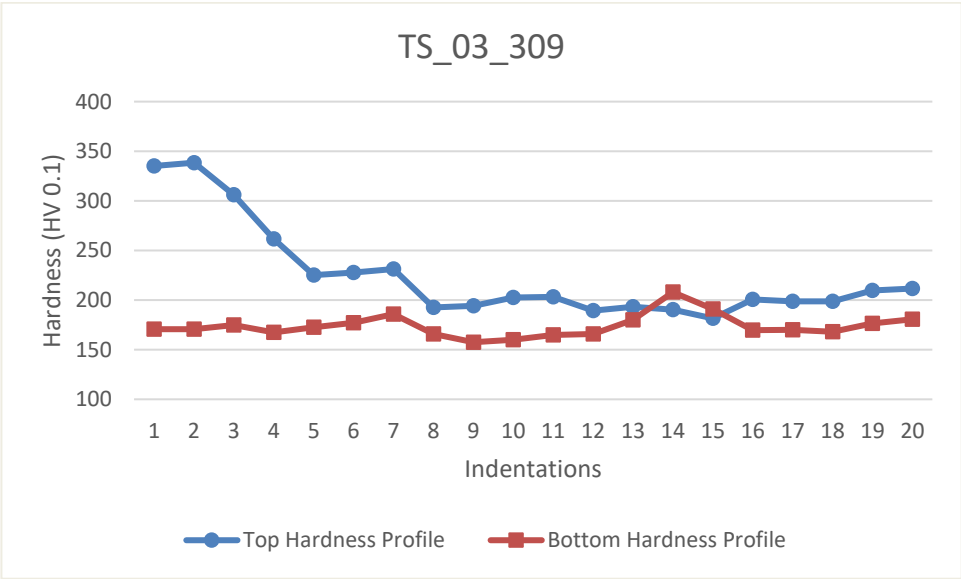


Figure 45: Microhardness profile of the welded joint between 5 mm AISI 301LN and 8 mm S355J2 with the filler metal AWS A5.22 E309LMoT0-1/4.

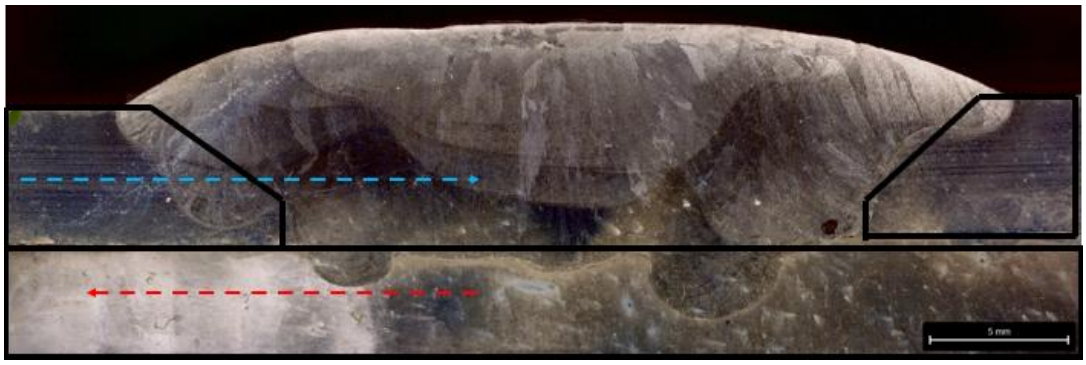


Figure 46:Macrostructure of welded joint between 5 mm AISI 301LN and 8 mm S355J2 with the filler metal AWS A5.22 E309LMoT0-1/4.

Figures 43 and 45 exhibit the same overall trend as previously observed. However, it is pertinent to note the significantly higher hardness within the AISI 301LN base material for this combination. This is attributed to the C1000 cold-rolled condition of this sheet, corroborated by the elevated BM hardness values obtained. A progressive decrease in hardness is observed as one transitions from the BM towards the FZ. Conversely, the bottom hardness profile reveals only a marginal variation between the HAZ and the BM. This behaviour differs markedly from the trends recorded in combination 2, where a more pronounced microstructural differentiation was observed.

Consistent with the microstructural analysis, five distinct regions are identified across the specimens: the AISI 301LN BM, the HAZ on the AISI 301LN side, the FZ, the HAZ on the S355J2 side, and the S355J2 BM. No significant hardness discrepancy is observed between the two FMs.

For combination 1, the S355J2 BM profile remains relatively unaffected, as corroborated by the macroscopic examinations. Given the geometric and parametric similarities, a comparable trend was anticipated for the other conditions. However, combination 3 deviates from this behaviour, displaying a bottom profile characterised by a linear hardness trend, thereby demonstrating a minimal impact of the welding process on the BM. Conversely, combination 2 exhibits a bottom profile characterised by wide hardness scattering. This phenomenon is a direct consequence of weld metal dilution with the S355J2 steel, resulting in localised elemental enrichment of the matrix.

4.3.3 Corrosions tests analysis

Following the neutral salt spray tests, during which one specimen was evaluated per condition, visual observations were conducted at 24-hour intervals, and representative photographs were captured. These macrographs of the initial, middle and final stages are presented in Figure 47.

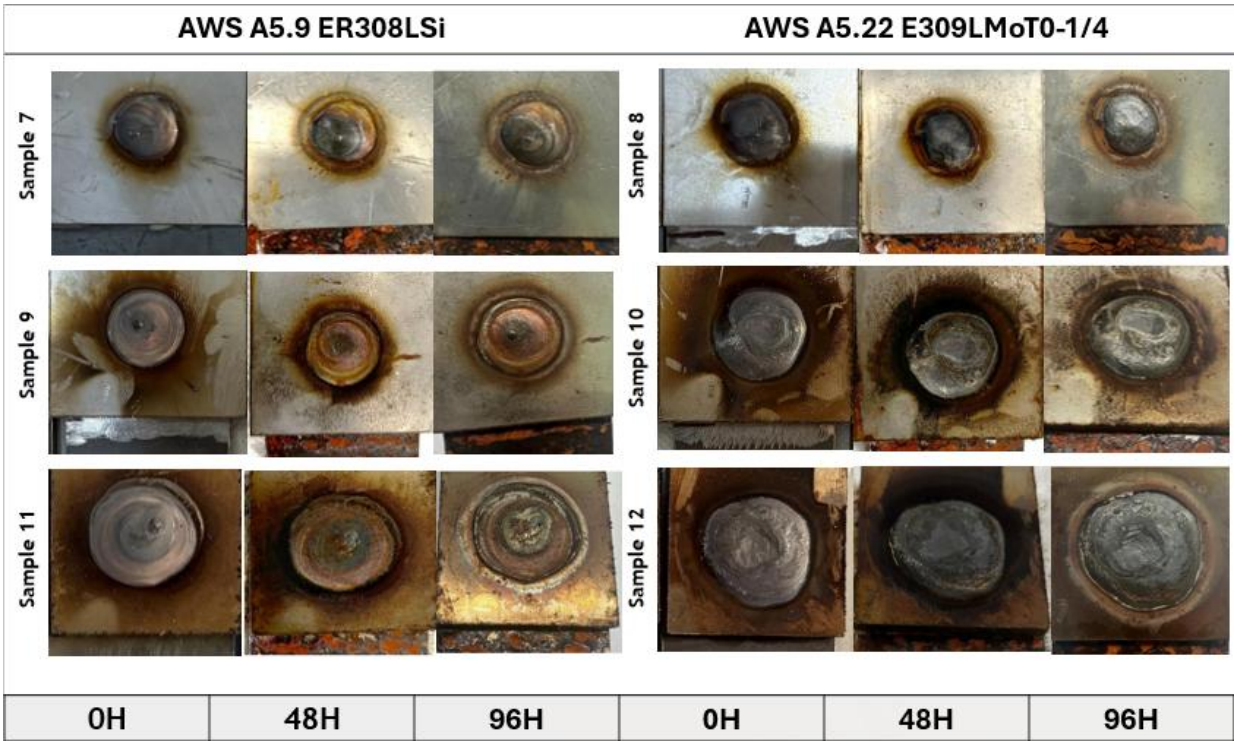


Figure 47: Images of the welded joints (Samples 7 to 12) showing the surface evolution during the neutral salt spray test at 0 h, 48 h, and 96 h of exposure, comparing filler metals AWS A5.9 ER308LSi and AWS A5.22 E309LMoT0-1/4.

All specimens exhibited corrosion after 96 hours of exposure. When comparing specimens welded with the same filler metal but differing in dimensions, specimens 7, 9 and 11 (ER308LSi) and specimens 8, 10 and 12 (E309LMoT0-1/4), no substantial differences in corrosion behaviour were observed within each group. This indicates that specimen dimensions do not constitute a significant variable in this test.

As anticipated in the literature review, the region first attacked by corrosion was the plug perimeter. This zone had been identified as susceptible to sensitisation of the austenitic stainless steel, and this was indeed observed, manifesting as reduced corrosion resistance in that region. In contrast, when specimens welded with different filler metals are compared, clear differences emerge, red corrosion was visible within the weld metal of joints welded with AWS A5.9 ER308LSi but was not observed to the same extent in joints welded with AWS A5.22 E309LMoT0-1/4. This lower corrosion resistance is attributable to the filler metal's chemical composition, as identical welding parameters were employed across all specimens. As previously discussed, AWS A5.9 ER308LSi presents lower Cr and Ni contents than AWS A5.22 E309LMoT0-1/4, which accounts for the latter's superior corrosion resistance. These findings are consistent with reports that corrosion of welded joints adversely affects their mechanical properties [88].

4.4 Mechanical tests of the welded joints

It should be noted that all specimens presented in this chapter were welded using AWS A5.22 E309LMoT0-1/4 filler metal, and the results discussed herein pertain exclusively to this filler metal.

4.4.1 Tensile shear test of the welded joints

Analysis of the tensile-tested specimens revealed that all specimens failed by interfacial fracture. This fracture mode indicates that the interface between the FM and the S355J2 base metal is the most mechanically fragile region of the joint, owing to a

localised stress concentration that results in premature failure, as illustrated in Figure 48.



Figure 48: Experimental failure mode of the specimen subjected to tensile testing, showing interfacial fracture.

Shear force–displacement curves were plotted for the three different geometries, as shown in Figures 49, 50, and 51.

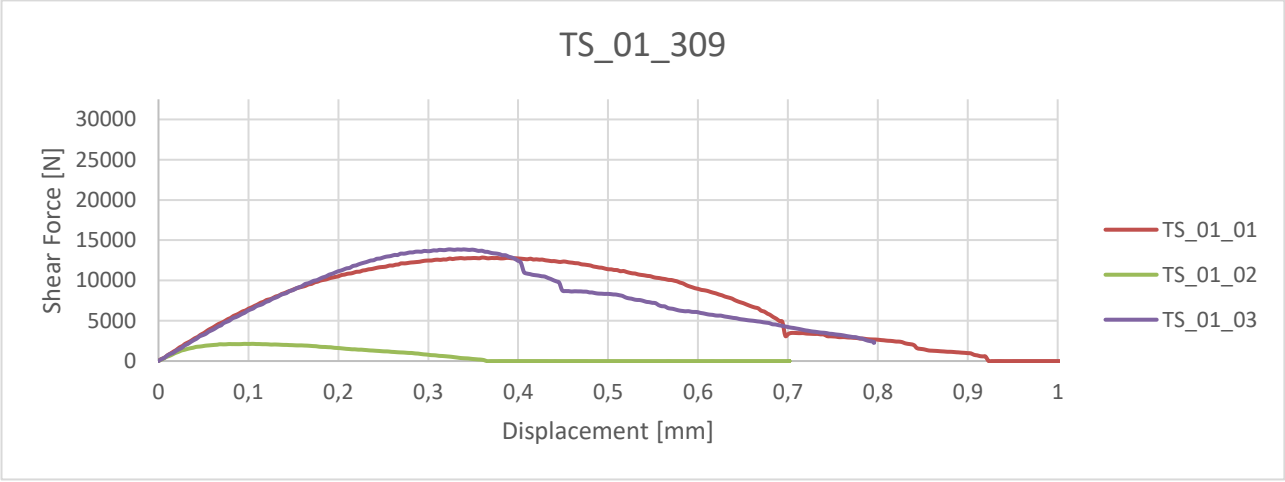


Figure 49: Experimental shear force-displacement graph – Geometry 1.5 mm AISI 301LN and 8 mm S355J2.

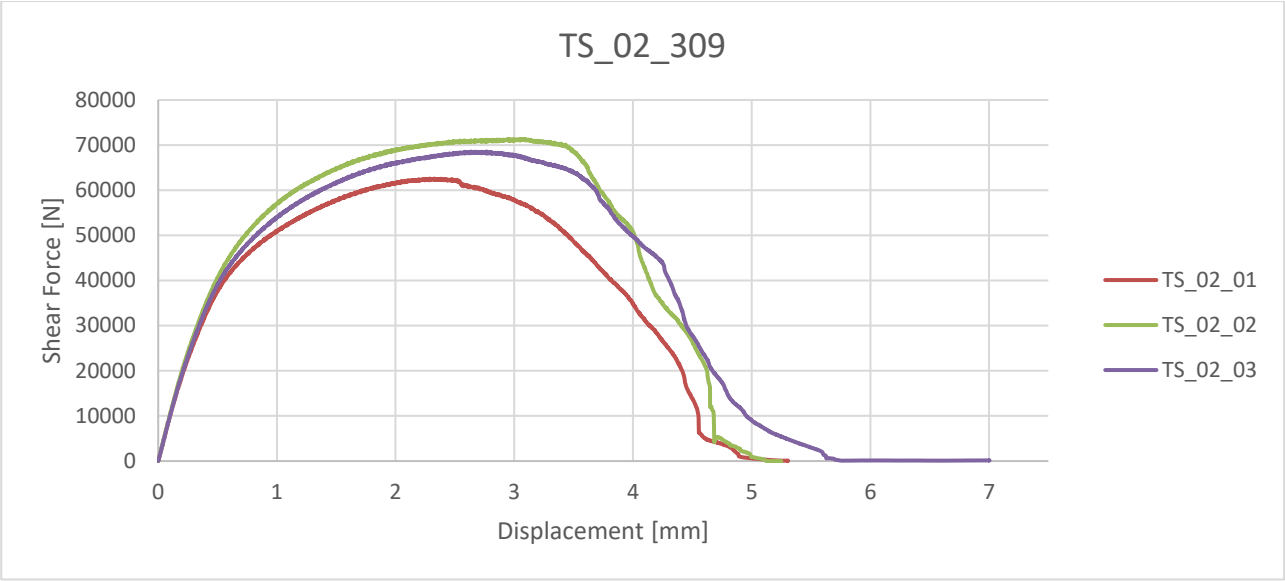


Figure 50:Experimental shear force-displacement graph – Geometry 4 mm AISI 301LN and 8 mm S355J2.

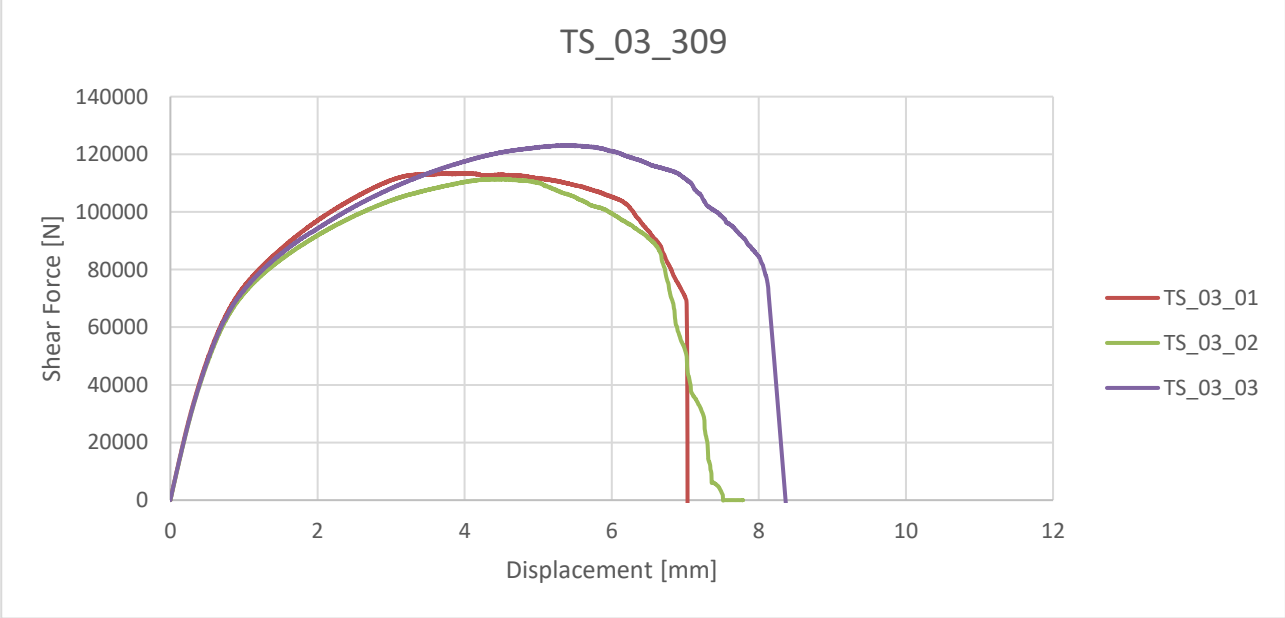


Figure 51:Experimental shear force-displacement graph – Geometry 5 mm AISI 301LN and 8 mm S355J2.

The shear force–displacement curves obtained for the three geometries (Figures 49, 50, and 51) reveal a clear increase in maximum shear force capacity with increasing joint geometry. Across geometries 2 and 3 (Figures 50 and 51), the three tested specimens exhibit consistent and overlapping behaviour, indicating good repeatability of the welding process and mechanical response. In contrast, in geometry 1, specimen TS_01_02 (Figure 49) exhibits a markedly lower shear force capacity. This result is attributed to a lack of fusion identified in this specimen, as illustrated in Figure 52, which compromised the effective bonding area and consequently reduced its load-bearing capacity.

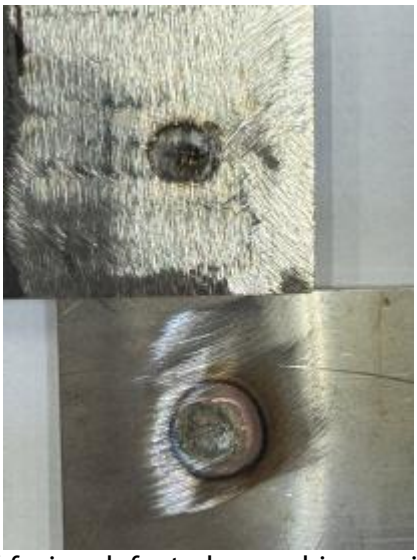


Figure 52: Lack of fusion defect observed in specimen TS_01_02.

4.4.2 Fatigue test of the welded joints

A total of twelve specimens were tested per condition during the fatigue tests. From these results, two graphs were derived, providing essential insight into the influence of different BM thicknesses and hole diameters on the fatigue resistance. Furthermore, these graphs enable a comparative assessment of the individual performance of the three plugs configurations under investigation, namely TS_01_309, TS_02_309, and TS_03_309.

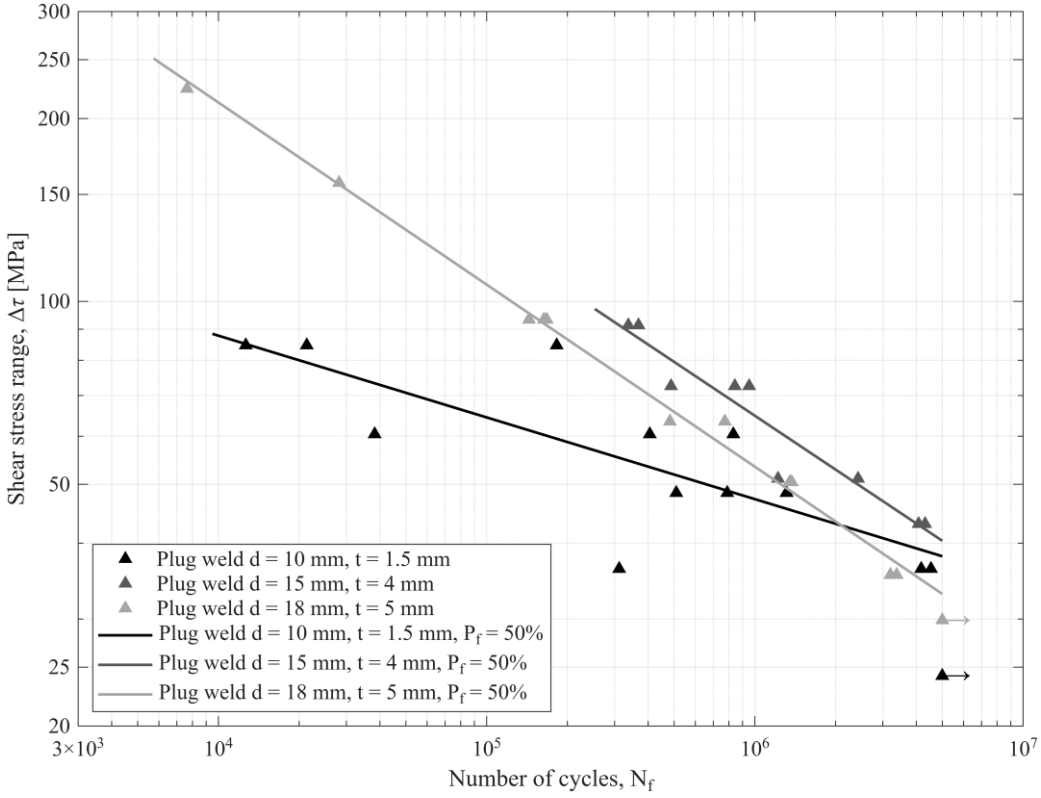


Figure 53: Fatigue Performance of TS_01_309, TS_02_309 and TS_03_309(Shear stress range (MPa)).

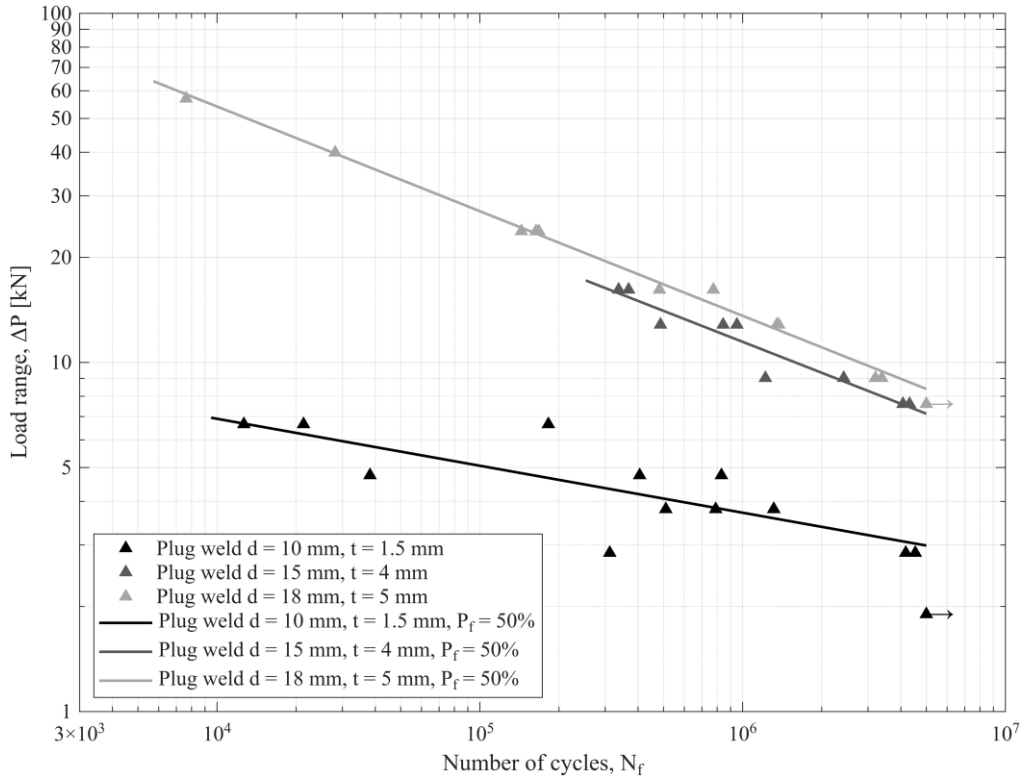


Figure 54: Fatigue Performance of TS_01_309, TS_02_309 and TS_03_309(Load range (N)).

The combined examination of the two graphs presented in Figures 53 and 54 reveals an inverse relationship between the applied stress level and the number of cycles to failure, corroborating the characteristic behaviour of welded joints subjected to fatigue loading. In Figure 53, the load range is plotted on the y-axis, representing the applied force in kN, whereas in Figure 54, the y-axis variable is the shear stress range, whereby the same loading condition is normalised as shear stress, in MPa. In terms of load range, the response is governed by the total force applied to the joint; in this case, factors such as the different thicknesses of the BM and the hole diameter strongly influence the relative positioning of the curves.

Upon transitioning to the shear-stress range, the applied force is normalised by the plug's effective resistance area, resulting in a slight convergence of the experimental points into a single probabilistic band. Consequently, the former reflects the joint's global response, whilst the latter approximates the local severity experienced by the plug weld. It is also important to note that the two run-out specimens (one belonging to TS_02_309 and one to TS_03_309) were excluded from the linear regression analysis and from other associated calculations, such as the slope and the coefficient of determination (R^2). Since these specimens did not reach failure within the defined experimental limit (5.00×10^6 cycles) .

Table 16: Statistical Analysis of the Fatigue Results.

CURVE	SPECIMENS TYPE	SLOPE	R^2	STANDARD DEVIATION
LOAD RANGE AND SHEAR STRESS RANGE	TS_01_309	-7,433	0,631	0,090
	TS_02_309	-3,395	0,917	0,040
	TS_03_309	-3,336	0,994	0,021

In both graphs, three distinct S-N curves can be identified, each corresponding to one of the combinations under study. Analysis of these lines reveals that two of them exhibit a similar slope. The third line, however, displays a markedly steeper slope, indicating a distinct joint response to cyclic loading. Given that all specimens were welded with the same filler metal, the observed difference can be attributed to plate thickness. Such a discrepancy may also provide insight into the mechanisms of crack initiation and propagation originating from the welded zone. Variations in thickness and hole diameter alter the local stress distribution and the mode of crack evolution, thereby accounting for the divergence observed between the regression lines[108,109].

Although the TS_03_309 configuration exhibits the highest load-bearing capacity at low cycle counts, its steeper slope indicates a more rapid degradation in fatigue strength with increasing number of cycles. In contrast, the TS_01_309 configuration, despite its lower initial capacity, retains its fatigue resistance more consistently. This behaviour suggests that the way the applied load is distributed between the plug and the BM leads to alterations in the crack initiation and propagation pattern. By contrast, the two curves with similar slopes differ in AISI 301LN thickness and plug diameter, but the differences are minimal, suggesting failure mechanisms that are closer to one another, although with differences in the absolute load values supported.

The statistical interpretation of the curves (Table 16) is corroborated by the R^2 values, which are central to validating the linear regression. Regarding both graphics, TS_02_309 exhibits an $R^2 = 0.917$, indicating reduced dispersion of points around the line. TS_03_309 shows an R^2 of 0.994, indicating almost perfect linear regression. In contrast, the TS_01_309 displays an $R^2 = 0.631$, indicating greater variability and a lower value.

There are differences when analysing the final form of the specimens put through testing. There are three different failure modes, as shown in Figure 55.

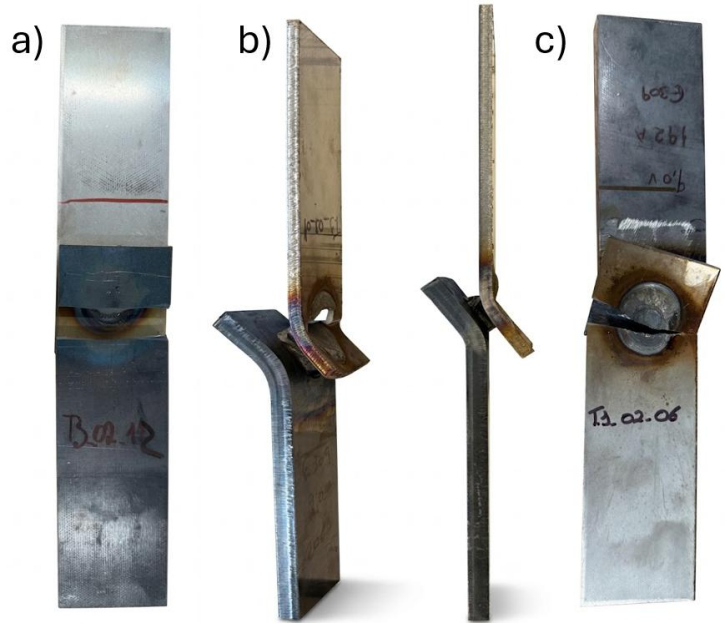


Figure 55: Fatigue test specimens of condition TS_02_309, a) partial pull-out failure mode in S355J2, b) interfacial fracture mode and c) partial pull-out failure mode in AISI 301LN.

As for the 12 specimens of condition TS_02_309, the 10 specimens tested in the lower load range, which exhibited a higher number of cycles to failure, also displayed a partial pull-out failure mode (Figure 55-a or Figure 55-c). The remaining 2 specimens, tested at the higher load range, exhibited an interfacial fracture mode (Figure 55-b). The interfacial fracture mode occurs when the crack propagates around the entire plug perimeter,

whereas in the partial pull-out failure mode, crack propagation initiates along approximately half of the plug perimeter and subsequently continues through the base material. The two specimens that exhibited a interfacial fracture mode were subjected to a higher applied load, which tends to promote a more rapid and global collapse of the joint. In the remaining specimens, the combination of a more moderate load and the resulting more progressive damage evolution likely led to a less extensive fracture, manifested as a partial pull-out failure mode.

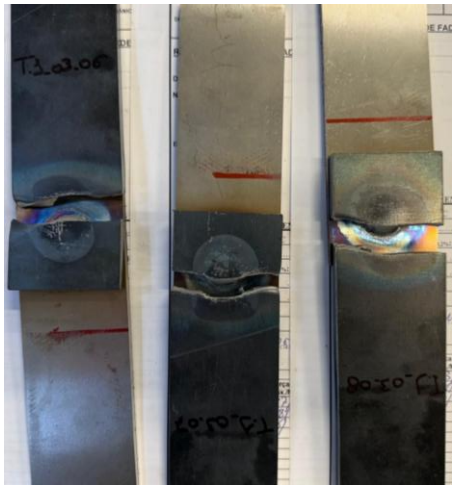


Figure 56: Fatigue test specimens of condition TS_03_309 partial pull-out failure mode in S355J2.

Similarly, of the 12 specimens in condition TS_03_309, the 10 tested in the lower load range exhibited a partial pull-out failure mode, however, in this condition, failure consistently occurred on the S355J2 side (Figure 56). The remaining 2 specimens, tested at the higher load range, exhibited an interfacial fracture mode, as observed for condition TS_02_309.

The failure modes and fatigue behaviour observed in the present study can be further contextualised by comparison with previous investigations on plug-welded joints involving dissimilar metals and varying plate thicknesses. Prior work on dissimilar plug-welded joints between carbon steel and austenitic stainless steel also reported the same two failure modes, partial pull-out and the interfacial fracture mode, with the transition between them governed by hole diameter rather than by the applied load level [110]. Below a critical hole diameter, failure occurred predominantly via shear due to insufficient weld penetration, whereas above this threshold, the joint consistently failed by partial pull-out [110]. Furthermore, research on plug-welded structures with similar-metal configurations has shown that the correlation between load range and fatigue life is strongly affected by variations in plug-weld diameter and plate thickness, resulting in significant scatter in load-life data and limiting its direct applicability to engineering design [40]. Overall, the observed failure modes are broadly consistent with those expected for plug-welded dissimilar joints; however, the present results also indicate that variations in plug diameter, in addition to plate thickness and applied load, exert a further influence on the resulting failure mode. This suggests that, given the considerable number of variables involved, such as plate thickness, plug diameter, filler metal composition, and load level, each joint configuration must be regarded as a distinct case, with its fatigue behaviour and failure mode governed by the specific combination of these parameters rather than by any single dominant factor.

5.CONCLUSIONS AND FUTURE WORK

This dissertation investigated the metallurgical and mechanical behaviour of dissimilar MAG-welded joints between structural steel S355J2 and austenitic stainless steel AISI 301LN, with the aim of identifying the most suitable filler metal, AWS A5.9 ER308LSi or AWS A5.22 E309LMoT0-1/4 and also different plug geometries, for application in the floor structure of a railway vehicle.

Based on the results obtained in the experimental tests, the following conclusions can be drawn:

- The microstructural observation and hardness confirmed that the AISI 301LN retained the expected austenitic matrix, with variations linked to the degree of cold working and sheet thickness.
- The preliminary results show the presence of discontinuities in the joints. Analysis of the transverse cross-sections revealed a lack of fusion at the borders of the plug weld. The tensile shear test further confirmed the lack of penetration at the centre of the plug, indicating that both the perimeter and the central region remained unwelded, with fusion limited to an intermediate annular zone.
- The preliminary results also indicated that the 0.8 mm AISI 301LN sheet generated gaps at the joint interface due to its lack of flatness. Separately, in the thicker AISI 301LN samples, a lack of fusion was observed at the corners of the plug weld, suggesting that countersinking could help mitigate this discontinuity. Furthermore, the lack of penetration observed points to the use of insufficiently high welding parameters.
- The macrostructure of the final samples reveals that the use of a 1.5 mm AISI 301LN sheet, instead of the 0.8 mm sheet, resolved the lack of flatness previously observed in the BM. There was a clear improvement with the countersink, eliminating the previous lack of fusion in the corners, as well as improving the bonding between the FM and the AISI 301LN. Additionally, increasing welding parameters resulted in a larger FZ in S355J2, representing a significant improvement, as the FZ in this material was previously almost negligible.
- The microstructural analysis of the final samples reveals that, at the FM, both filler metals present an austenitic matrix with dendritic ferrite, showing no significant difference between the two FMs. In the S355J2 HAZ, both martensite and precipitates were identified.
- The hardness profiles confirm a clear correlation with microstructural alterations in the different regions of the joint. However, the hardness of the different FMs did not differ significantly, although the pattern remained consistent across all samples. In the top hardness profile, the BM of AISI 301LN shows the highest hardness, which decreases as it approaches the FM, and reaching the lowest point at the FM. In the bottom hardness profile, the HAZ of S355J2 shows the highest hardness due to the formation of precipitates and the martensite phase, which then decreases until it stabilises in the BM of S355J2.
- The corrosion analyses aimed at understanding the differences between the two FMs. Regarding the comparison between filler metals, it was established that, for AWS A5.9 ER308LSi, the plug area was the first to be affected after 48 hours; in the case of AWS A5.22 E309LMoT0-1/4, the sample showed no corrosion at this stage. After 96 hours, corrosion was visible in every sample: AWS A5.9 ER308LSi showed corrosion both in the plug and in the plug perimeter, whereas AWS A5.22 E309LMoT0-1/4 only showed corrosion in the plug perimeter

- The tensile shear tests of the welded joints show better results when compared to the preliminary results, demonstrating that the process alterations were positive. TS_03_309 is the combination with the highest load-to-failure. On the other hand, TS_01_309 shows a lower load-to-failure combined with high variation, revealing a lack of penetration in the S355J2.
- The fatigue behaviour indicates that the different thicknesses and diameters of the plug have a significant influence on cyclic resistance. For railway structures, this is especially important because the joints are subjected to repeated loading over long service periods. Of the three configurations studied, the one that exhibited the best fatigue resistance was TS_03_309.

From a railway perspective, this study confirms that plug welding is a suitable joining process for AISI 301LN with S355J2, provided that the welding parameters are properly adjusted for each configuration. The most suitable FM is AWS A5.22 E309LMoT0-1/4, due to its higher corrosion resistance, since these joints will be exposed to varying environmental conditions, and their mechanical properties are influenced by corrosion. The most reliable joint is TS_03_309, which shows the highest load-to-failure and the best fatigue resistance. However, TS_01_309 did not show significant positive results, requiring a new approach to this configuration.

From a future work perspective and to maintain continuity with this study, two directions are worth exploring. Firstly, the TS_01_309 combination should be reconsidered with a view to improvement, as it still exhibits high variation and limited penetration; increasing the welding parameters and/or the plug diameter could be viable options to address this. Finally, mechanical testing should be carried out on specimens that have already undergone corrosion to understand how this condition affects their mechanical properties, thereby ensuring the longest possible service life for the trains and maximum safety for all future passengers of the Portuguese railway system.

6.References

[1] E. Commission, European Commission adopts 9th report on development of the rail market', (2025). https://transport.ec.europa.eu/news-events/news/european-commission-adopts-9threport-development-rail-market-2025-07-30_en.

[2] E.G. Deal, E. Commission, The European Green Deal, (n.d.). https://commission.europa.eu/strategy-and-policy/priorities-2019-2024/european-green-deal_en.

[3] N.R. Plan, P. Republic, Plano Ferroviário Nacional, Presidency of the Council of Ministers, Lisbon, 2022. https://arquivo.pt/wayback/20240516123302mp_/https://pfn.gov.pt/wp-content/uploads/2022/11/plano-ferroviario-nacional-20221117.pdf.

[4] A.P. Ferro, Pedido de Salvaguarda de Carruagens Sorefame, (2016). https://www.caminhosdeferro.pt/preservacao/wp.

[5] S.E.R.M.E.C. Group, O Grupo SERMEC The Road of Tomorrow', (2017). https://www.sermec2.pt/group.php#sermec.

[6] T.S. Portugal, Producing Railway Rolling Stock in Portugal: Mobilizing Agendas for Business Innovation', Accessed Nov 26 (2024). https://trainsolutions.pt/en/#entidades.

[7] J. Martin, Metal and alloys', Mater. Eng. 3a (2006) 71–132.

[8] R. Singh, Stainless steels and other CRAs', in Applied Welding Engineering Processes, Codes Stand. 3a (2020) 77–84.

[9] C.I.V.M.A.T.S., Austenitic STAINLESS STEEL 301 (UNS S30100 / W.Nr, (2025). https://www.civmats.com/grades/GRADES-301.HTML.

[10] European Committee for Standardization, Stainless steels - Part 2: Technical delivery conditions for sheet/plate and strip of corrosion resisting steels for general purposes, EN 10088–2: 2005 (2005).

[11] J.A. Brooks, J.C. Lippold, Selection of Wrought Austenitic Stainless Steels', in: Weld. Brazing Solder., United States of America: ASM International, 1993: pp. 1155–1189.

[12] R. Singh, Welding, corrosion-resistant alloys—Stainless steel', in Applied Welding Engineering Processes, Codes Stand. 3a (2020) 251–271.

[13] S. Saha, M. Mukherjee, T.K. Pal, Microstructure, Texture, and Mechanical Property Analysis of Gas Metal Arc Welded AISI 304 Austenitic Stainless Steel, J. Mater. Eng. Perform. 24 (2015) 1125–1139.

[14] A. Järvenpää, Processing and Properties of Reversion-Treated Austenitic Stainless Steels, Metals 10 (2020) 281.

[15] M. Tikhonova, R. Kaibyshev, A. Belyakov, Microstructure and Mechanical Properties of Austenitic Stainless Steels after Dynamic and Post-Dynamic Recrystallisation Treatment, Adv. Eng. Mater. 20 (2018).

[16] J.C. Lippold, D.J. Kotecki, Welding Metallurgy and Weldability of Stainless Steels, John Wiley & Sons, Hoboken, NJ, 2005.

[17] K.H. Lo, C.H. Shek, J.K.L. Lai, Recent Developments in Stainless Steels, Mater. Sci. Eng. R Rep. 65 (2009) 39–104.

[18] A.J. Sedriks, Corrosion of Stainless Steels, 2.a, John Wiley & Sons, New York, 1996.

[19] A. Järvenpää, M. Jaskari, A. Kisko, P. Karjalainen, Cyclic Behavior of Reversion-Treated Structures after Different Cold Rolling Reductions in an AISI 301LN Stainless Steel, Key Eng. Mater. 786 (2020) 52–59.

[20] J.W. Simmons, Overview: High-Nitrogen Alloying of Stainless Steels, Mater. Sci. Eng. A 207 (1996) 159–169.

[21] S.E. Hughes, Fracture Modes and Welding Defects', in A Quick Guide to Welding and Weld Inspection, in: Woodhead Publ. Ser. Weld. Join. Technol., Woodhead Publishing Limited, Cambridge UK, 2009: pp. 88–107.

[22] J.A. Siefert, S.A. David, Weldability and weld performance of candidate austenitic alloys for advanced ultrasupercritical fossil power plants', Sci Technol Weld Join 19 (2014) 271-294,. https://doi.org/10.1179/1362171814Y.0000000197.

[23] P.R. Vishnu, Solid-State Transformations in Weldments', in: Weld. Brazing Solder., United States of America: ASM International, 1993: pp. 162–356.
[24] P. Kah, M. Shrestha, J. Martikainen, Trends in Joining Dissimilar Metals by Welding', Appl Mech Mater 440 (2013) 269-276,. https://doi.org/10.4028/www.scientific.net/amm.440.269.
[25] R.E. Avery, Guidelines for Welding Dissimilar Metals', (1991). https://nickelinstitute.org/media/o3dnv2vx/14018_guidelinesforweldingdissimilarmetals.
[26] A. O'Brien, C. Guzman, Chapter 7—surfacing materials, in welding handbook - materials and applications, part 1, American Welding Society, 2011.
[27] K. Weman, 19 - The weldability of steel, in: K. Weman (Ed.), Weld. Process. Handb., Second, Woodhead Publishing, 2012: pp. 191–206.
[28] W.F. Gale, T.C. Totemeier, 33 - Welding, in: Smithells Met. Ref. Book, Eighth, Oxford, Butterworth-Heinemann, 2004: pp. 33-1-33–58.
[29] A. O'Brien, C. Guzman, Chapter 5 - Stainless and Heat-resistant Steels, in: Weld. Handb. - Mater. Appl. 1 Aw Soc. Ed. 2011 Chapter 5 - Stainl. Heat-Resist. Steels, n.d.: pp. 255–390.
[30] J. C.Lippold, Chapter 3 - Hot Cracking, in Welding Metallurgy and Weldability, John Wiley & Sons, 2015.
[31] Metalore Foundation for future, (2016). https://www.metalore.co.in/blog/common-applications-of-s355-structural-steel-plate/.
[32] I.P. Qualidade, Produtos laminados a quente de aços de construção Parte 2: Condições técnicas de fornecimento para aços de construção não ligados, (n.d.).
[33] M. Kubiak, W. Piekarska, T. Domański, Z. Saternus, Modelling of Phase Transformations in Solid State and Dilatometric Curves Using Interpolation Methods to Determine CCT Diagrams', Acta Phys Pol A 142 (2022) 184-187,. https://doi.org/10.12693/APhysPolA.142.184.
[34] I. Guru, Copper in Steels', Accessed Aug 13 (2014). https://www.ispatguru.com/copper-in-steels.
[35] J. Ihme, Supporting Structures and Superstructures of Railway Vehicles', in: Rail Veh. Technol., Springer, Wiesbaden, 2022: pp. 215–270.
[36] Produtos laminados a quente de aços de construção Parte 1 condições técnicas gerais de fornecimento NP EN 10025-1: 2014, (2014) 35–35.
[37] R. Chaudhari, P.K. Loharkar, A. Ingle, Applications and challenges of arc welding methods in dissimilar metal joining, IOP Conf. Ser. Mater. Sci. Eng. 810 (2020) 012006.
[38] N. Institute, Welding of Stainless Steels and other Joining Methods - A Designers, Nickel Institute, Toronto, Ontario, 2020.
[39] H. Cerjak, P. Mayr, Creep strength of welded joints of ferritic steels', in: Creep Resist. Steels Woodhead Publ. Ser. Met. Surf. Eng., Woodhead Publishing Limited, Cambridge England, 2008: pp. 472–503.
[40] W. Shao, X. An, L. Yang, G. Yang, T. Zhu, Z. Zhang, B. Zhang, Investigation of fatigue characteristics and damage behaviour in weathering steel plug-welded structures, Eng. Struct. 356 (2026) 122466.
[41] M. Vural, Welding Processes and Technologies: Comprehensive Materials Processing, Elsevier (2014) 3–48.
[42] ISO/TR 25901-1:2016, Welding and allied processes — Vocabulary — Part 1: General terms, (2016).
[43] M.P. Grover, Fundamentals of modern manufacturing: Materials, Process, and Systems, (2013) 776–779.
[44] K. Weman, Introduction to welding', in: Weld. Process. Handb. 2a Woodhead Publ. Ser. Weld. Join. Technol., Woodhead Publishing Limited, Cambridge UK, 2012: pp. 1–12.
[45] A. O'Brien, C. Guzman, Clad And Dissimilar Metals, in Welding Handbook - Materials and Applications, American Welding Society, 2011.
[46] K. Weman, MIG/MAG welding', in: Weld. Process. Handb. 2a Woodhead Publ. Ser. Weld. Join. Technol., Woodhead Publishing Limited, Cambridge UK, 2012: pp. 75–97.
[47] W. Europe, Comparison of welding processes: MIG and MAG welding', Accessed Aug 25

(2025). https://www.weldaseurope.com/knowledge.
[48] E.S.A.B. University, MIG Welding: Techniques, Advantages and Applications', Accessed Aug 25 (2022). https://esab.com/pt/eur_en/esab.
[49] U.T. Institute, What Is Metal Active Gas (MAG, Welding' Accessed Aug 25 (2025). https://www.uti.edu/blog/welding/gmaw.
[50] I. Davila-Rios, I. Lopez-Juarez, L. Martinez-Martinez, L.M. Torres-Treviño, Implementation of an Intelligent Robotized GMAW Welding Cell, Part 1: Design and Simulation', Robot Manip. Trends Dev. InTechOpen (2010) 543 562.
[51] M. Bäck, Welding of dissimilar metals in different welding positions', Master Thesis, KTH Royal Institute of Technology School of Engineering Sciences, 2015.
[52] D. Naidu, K. Moore, S. Ozcelik, Gas Metal Arc Welding: Modeling', in Modeling, Sensing and Control of Gas Metal Arc Welding, Elsevier, Oxford UK, 2003.
[53] D.H. Phillips, Arc Welding Processes', in Welding Engineering An Introduction, John Wiley & Sons, Chichester United Kingdom, 2016.
[54] K.A. Lyttle, Shielding Gases for Welding', in: Weld. Brazing Solder., United States of America: ASM International, 1993: pp. 148–306.
[55] A.W. Society, AWS D1.1/D1.1M:2020 Structural Welding Code Steel, American Welding Society, Miami, 2020.
[56] S.K. Shihab, R.H. Mohamed, E.M. Mubarek, Optimization of Process Parameters in Cladding of Stainless Steel over Mild Steel, Mater. Today Proc. 16 (2019) 816–823.
[57] A.S.M.I.H. Committee, 112.3 Weld Cladding, ASM Handb. 06 (n.d.) 815–829.
[58] Z. Śloderbach, J. Pająk, Determination of Ranges of Components of Heat Affected Zone Including Changes of Structure / Określenie Zakresów Składowych Strefy Wpływu Ciepła Uwzględniając Zmiany Struktury, Arch. Metall. Mater. (2015) 60.
[59] H. Bhadeshia, R. Honeycombe, 13.3.2 Microstructural Zones, in: Steels - Microstruct. Prop., 4th ed., Elsevier, n.d.
[60] J.R. Davis, 5.1.1 Single-Pass Weldments, in: ASM Spec. Handb. Carbon Alloy Steels, ASM International, 1996.
[61] C. Hui-Chi, B. Guijun, S. Chen-Nan, High Energy Beam Welding Processes in Manufacturing, in: Editor. (Ed.), Handb. Manuf. Eng. Technol. AC Nee, London, Springer London, 2015: pp. 617–639.
[62] H. Granjon, CHAPTER 3 - Introduction to the metallographical examination of welds, in: H. Granjon (Ed.), Fundam. Weld. Metall., Woodhead Publishing, 1991: pp. 57–67.
[63] A.S. Shahi, S. Pandey, Modelling of the effects of welding conditions on dilution of stainless steel claddings produced by gas metal arc welding procedures, J. Mater. Process. Technol. 196 (2008) 339–344.
[64] J.G. Feldstein, Dissimilar Welds With Stainless Steels', in: Weld. Brazing Solder., United States of America: ASM International, 1993: pp. 1264–1273.
[65] P.J. Haagensen, Fatigue strength improvement methods', in Fracture and Fatigue of Welded Joints and Structures, in: Woodhead Publ. Ser. Weld. Join. Technol., Woodhead Publishing Limited, Cambridge UK, 2011: pp. 297–329.
[66] R. Singh, Stresses, Shrinkage, and Distortion in Weldments', in: Appl. Weld. Eng. Process. Codes Stand. 2a, Elsevier, 2016: pp. 201–238.
[67] S.J. Maddox, Significant features of welds in relation to fatigue', in: Fatigue Strength Welded Struct. 2a Woodhead Publ. Ser. Weld. Join. Technol., Woodhead Publishing Limited, Cambridge England, 1991: pp. 19–29.
[68] J.C. Lippold, D.J. Kotecki, 3.1 Alloying Elements in Stainless Steels, in: Weld. Metall. Weldability Stainl. Steels, John Wiley & Sons, 2005.
[69] L. Nhung, P.M. Khanh, A.T. Hoang, D.N. Nguyen, Microstructure Change For Multi-Pass Welding Between Austenitic Stainless Steel And Carbon Steel', J Mech Eng Res Dev 41 (2018) 97-102,. https://doi.org/10.26480/jmerd.02.2018.97.102.
[70] C.C. C., P. Abe, Influence of Welding on Steel Weldment Properties', in: Weld. Brazing Solder., United States of America: ASM International, 1993: pp. 1068–1093.
[71] L. Jeffus, Welding: Principles and Applications, (2015).

[72] R. Singh, Weld Defects and Inspection', in Applied Welding Engineering, Process. Codes Stand. 2a (2016) 277–295.
[73] J. C.Lippold, Chapter 5 - Hydrogen-Induced Cracking, in Welding Metallurgy and Weldability, John Wiley & Sons, Canada, 2015.
[74] Sodel, Cold Cracking Of Welds', (2025). https://www.sodel.com/medias/iw/cold-cracking-of-welds-sodel.pdf.
[75] H. Granjon, Hardening and cold cracking in steel welding', in: Fundam. Weld. Metall. Woodhead Publ. Ser. Weld. Join. Technol., Woodhead Publishing Limited, Cambridge England, 1991: pp. 156–177.
[76] G. Mathers, Welding metallurgy', in The Welding of Aluminium and its Alloys, in: Woodhead Publ. Ser. Weld. Join. Technol., Woodhead Publishing Limited, Cambridge England, 2002: pp. 10–34.
[77] Y. Huang, J. Huang, J. Zhang, X. Yu, Q. Li, Z. Wang, D. Fan, Microstructure and corrosion characterization of weld metal in stainless steel and low carbon steel joint under different heat input, Mater. Today Commun. 29 (2021) 102948. https://doi.org/10.1016/j.mtcomm.2021.102948.
[78] A.K. Maurya, S.M. Pandey, R. Chhibber, D. Fydrych, C. Pandey, Corrosion performance of super duplex stainless steel and pipeline steel dissimilar welded joints: a comprehensive investigation for marine structures, Int. J. Adv. Manuf. Technol. 135 (2024) 1009–1033. https://doi.org/10.1007/s00170-024-14596-3.
[79] C. Wang, Y. Yu, J. Yu, Y. Zhang, Y. Zhao, Q. Yuan, Microstructure evolution and corrosion behavior of dissimilar 304/430 stainless steel welded joints, J. Manuf. Process. 50 (2020) 183–191. https://doi.org/10.1016/j.jmapro.2019.12.015.
[80] A.R. Beeravolu, N.K. Babu, M.K. Talari, A.U. Rehman, P. Srirangam, Influence of Microstructure and Mechanical Properties of Dissimilar Rotary Friction Welded Inconel to Stainless Steel Joints, Materials 16 (2023) 3049. https://doi.org/10.3390/ma16083049.
[81] J.J.J. Cisneros Fonfría, E. Olmeda, S. Sanz, M. Garrosa, V. Díaz, Failure analysis of a train coach underframe', Eng Fail Anal 156 (2024) 1-13,. https://doi.org/10.1016/j.engfailanal.2023.107756.
[82] M. Vogt, K. Dilger, M. Kassner, Investigations on different fatigue design concepts using the example of a welded crossbeam connection from the underframe of a steel railcar body', Int J Fatigue 34 (2012) 47-56,. https://doi.org/10.1016/j.ijfatigue.2011.01.017.
[83] Y. Suzuki, Railway industry', in: Handb. Adhes. Technol., Springer, Berlin, Heidelberg, 2011: pp. 1214–1215.
[84] Y.-L. Lee, Fatigue damage theories', in Fatigue Testing and Analysis, Elsevier (2005) 57–76.
[85] G. Kang, H. Luo, Review on fatigue life prediction models of welded joint', Acta Mech Sin 36 (2020) 701-726,. https://doi.org/10.1007/s10409-020-00957-0.
[86] Y.-L. Lee, D. Taylor, Stress-Based Fatigue Analysis And Design', in Fatigue Testing and Analysis, Elsevier (2005) 103–180.
[87] S. Suresh, Fatigue of materials, 2nd ed, Cambridge University Press, Cambridge ; New York, 1998.
[88] W. Fricke, Fatigue analysis of welded joints: state of development, Mar. Struct. 16 (2003) 185–200. https://doi.org/10.1016/S0951-8339(02)00075-8.
[89] G.A.M. Mendes, Fadiga de juntas soldadas em aços estruturais de alto limite elástico', Master Thesis, Faculty of Science and Technology of the University of Coimbra, 2009.
[90] M.A. Kumbhalkar, D.V. Bhope, A.V. Vanalkar, Finite Element Analysis of Rail Vehicle Suspension Spring for Its Fatigue Life Improvement', in: Adv. Manuf. Mater. Sci. Lect. Notes Multidiscip. Ind. Eng., Springer, Cham, 2018: pp. 39–53.
[91] S.E.R.M.E.C. Group, Unpublished certificate, 'Quality Certificate of S355J2,' Mar 20 (2024).
[92] S.E.R.M.E.C. Group, Unpublished certificate, 'Inspection certificate of 1.4318 Type 301LN 4.0 mm,' Mar 25 (2025).
[93] S.E.R.M.E.C. Group, Unpublished certificate, 'Inspection certificate of 1.4318 Type 301LN

1.5 mm,' Mar 13 (2025).
[94] S.E.R.M.E.C. Group, Unpublished certificate, 'Inspection certificate of 1.4318 Type 301LN 5,0 mm,' Feb 14 (2025).
[95] J.F. Unsworth, 2.3.4 Weldability, in: Des. Constr. Mod. Steel Railw. Bridg., 2nd ed., CRC Press, 2018.
[96] S.E.R.M.E.C. Group, Unpublished certificate, 'Inspection certificate of AWS A 5.22 E309LMoT0 1/4,' (2026).
[97] S.E.R.M.E.C. Group, Unpublished certificate, 'Inspection certificate of AWS A 5.9 ER308LSi,' Jan 1 (2026).
[98] International Organization for Standardization, Welding — Guidelines for a metallic materials grouping system, ISO/TR 15608 (2017).
[99] International Organization for Standardization, Welding consumables — Gases and gas mixtures for fusion welding and allied processes, ISO 14175 (2008).
[100] EN ISO 14273:2016, Resistance welding — Destructive testing of welds — Specimen dimensions and procedure for shear testing of resistance spot, seam and embossed projection welds, (2016).
[101] ISO 17639:2022, Destructive tests on welds in metallic materials — Macroscopic and microscopic examination of welds, (n.d.).
[102] G.F. Vander Voort, Metallography: principles and practice, 4. print, ASM International, Materials Park, Ohio, 2007.
[103] ISO 4136: Destructive tests on welds in metallic materials — Transverse tensile test, n.d.
[104] J.F. Lancaster, The physics of welding, Phys. Technol. 15 (1984) 73–79. https://doi.org/10.1088/0305-4624/15/2/I05.
[105] R.W. Messler, Principles of welding : processes, physics, chemistry, and metallurgy, 2004.
[106] H.B. Cary, Modern Welding Technology, 1979. http://ci.nii.ac.jp/ncid/BA12614717?l=en.
[107] S. Kou, Welding Metallurgy, 1st ed., Wiley, 2002. https://doi.org/10.1002/0471434027.
[108] Metal Fatigue Analysis Handbook, Elsevier, 2012. https://doi.org/10.1016/C2010-0-66376-0.
[109] Metal fatigue analysis handbook: practical problem-solving techniques for computer-aided engineering, n.d.
[110] Triyono, Jamasri, M.N. Ilman, R. Soekrisno, Static and fatigue behavior of plug-welded dissimilar metal welds between carbon steel and austenitic stainless steel with different thicknesses, Int. J. Mech. Mater. Eng. 9 (2014) 17. https://doi.org/10.1186/s40712-014-0017-4.

APPENDIX

A Tensile Shear Results of Preliminary Results

PEAK SHEAR FORCE (N)	SAMPLE 1	SAMPLE 2	SAMPLE 3	SAMPLE 4	SAMPLE 5	SAMPLE 6
SPECIMEN 1	9007	8938	50592	24207	95130	89658
SPECIMEN 2	6642	10323	66456	16977	94668	72624
SPECIMEN 3	5808	6332	52360	27126	92833	96113
SPECIMEN 4			58371	28977	89528	95361
SPECIMEN 5			66454		93564	88870
AVERAGE	7152	8531	58846	24322	93145	88525
MAXIMUM	9007	10323	66456	28977	95130	96113
MINIMUM	5808	6332	50592	16977	89528	72624
RELATIVE STANDARD OF DEVIATION	19%	19%	11%	19%	2%	10%